Numerical modelling of turbulent premixed jet flames in large eddy simulation framework

Perković, Luka

Doctoral thesis / Disertacija

2014

Degree Grantor / Ustanova koja je dodijelila akademski / stručni stupanj: **University of Zagreb, Faculty of Mechanical Engineering and Naval Architecture / Sveučilište u Zagrebu, Fakultet strojarstva i brodogradnje**

Permanent link / Trajna poveznica: https://urn.nsk.hr/urn:nbn:hr:235:777153

Rights / Prava: In copyright / Zaštićeno autorskim pravom.

Download date / Datum preuzimanja: **2025-03-11**

Repository / Repozitorij:

Repository of Faculty of Mechanical Engineering and Naval Architecture University of Zagreb

DIGITALNI AKADEMSKI ARHIVI I REPOZITORIJI

University of Zagreb

FACULTY OF MECHANICAL ENGINEERING AND NAVAL ARCHITECTURE

LUKA PERKOVIĆ

NUMERICAL MODELLING OF TURBULENT PREMIXED JET FLAMES IN LARGE EDDY SIMULATION FRAMEWORK

DOCTORAL THESIS

Supervisor:

Prof. Dr. Sc. Neven Duić

Zagreb, 2014.

Sveučilište u Zagrebu

FAKULTET STROJARSTVA I BRODOGRADNJE

LUKA PERKOVIĆ

NUMERIČKO MODELIRANJE TURBULENTNIH PREDMIJEŠANIH PLAMENOVA METODOM SIMULACIJE VELIKIH VRTLOGA

DOKTORSKI RAD

Mentor:

Prof. dr. sc. Neven Duić

Zagreb, 2014.

BIBLIOGRAPHY DATA

Keywords:

Scientific area:

Scientific field:

Institution:

Principal supervisor:

Number of pages:

Number of figures:

Number of tables:

Number of references:

Date of oral examination:

Jury members:

Acknowledgements

This work has taken place at the Department of Energy, Power Engineering and Environment of the Faculty of Mechanical Engineering and Naval Architecture, University of Zagreb.

First, I would like to thank my mentor and supervisor, Professor Neven Duić, for inviting me into his computational fluid dynamics team, showing trust in me, giving constructive comments during the intensive work periods and providing motivation during the hard times.

Next, I would like to thank to my colleagues and collaborators at the Department, especially to Powerlab crew for providing the constructive and beneficial discussions and a good atmosphere at the office. They are: senior research assistants Marko Ban and Milan Vujanović and young researchers Hrvoje Mikulčić and Zvonimir Petranović. I would also like to thank to other fellow researchers from the Department: Boris Ćosić, Tomislav Pukšec and senior researcher Goran Krajačić for being good friends and colleagues during this work.

The writing of this thesis would be impossible without the AVL AST people, who gave the guidelines for the work that has to be done, as well as providing the great help through discussion and technical support. They are: Dr. Peter Priesching, Dr. Reinhard Tatschl, Dr. Branislav Basara and others. AVL AST Zagreb is acknowledged for the financial support of this work. Special thanks in this respect go to AVL AST Zagreb director, Mr. Goran Mirković.

I am very thankful for the valuable suggestions on a draft of this thesis that I received from other jury members, Professors Zdravko Virag and Assistant Professors Željko Tuković and Franjo Juretić.

At the end, I am greatly thankful to my family, my wife Matea and my newborn son Filip Jan, for loving support during this work and for fulfilling my life outside the office. Also, I am very grateful to my Mom and Dad for giving me love and support during the years when was I depending on them.

Contents

Acknowledgements II

Abstract VI

Keywords VI

Sažetak VII

Ključne riječi VII

Proširenі Sažetak VIII

Motivacija i generalni pregled VIII

Pregled trenutnih istraživanja VIII

Doprinos rada X

Nomenclature XI

List of Figures XVII

List of Tables XXI

1 Introduction 1

1.1 Motivation, general overview and state-of-the-art in LES research 1

1.2 Work hypothesis and outline 4

1.3 Thesis contribution 4

2 Mathematical method in LES framework 5

2.1 Reynolds and Favre averaging 7

2.2 Implicit filtering in Large Eddy Simulation 8

2.3 Conservation equations in LES framework 9

2.3.1 Conservation of mass 9

2.3.2 Conservation of momentum 10

2.3.3 Conservation of energy 10

2.3.4 Scalar transport 11

2.4 Modelling of unresolved or Sub-Grid Scale (SGS) turbulent transport in conservation equations 12

2.4.1 Smagorinsky model 12
2.4.2 Coherent Structure Method (CSM) 13
2.5 Hybrid LES/RANS approach 14
2.6 Species transport 15
2.7 Turbulent premixed combustion modelling 17
2.7.1 Turbulent premixed combustion regime 17
2.7.2 Flame local quenching by flame stretch 19
2.7.3 Coherent flame model in LES framework (CFMLES) 20
2.8 Boundary conditions in LES framework 27
2.8.1 Vortex Method (VM) for turbulent inlet boundary conditions 28
2.8.2 Non-reflective outflow boundary conditions 29
2.9 Flame-wall interaction modelling 31
3 Error Assesment for LES framework 32
3.1 Modelling errors 33
3.2 Discretization errors 34
3.3 Numerical errors 35
4 Numerical procedure 36
4.1 Integral form of the transport equations 36
4.2 Discretization into finite number of control volumes 37
4.3 Requirements for the mesh quality 38
4.4 Domain decomposition in parallel computing 38
4.5 Numerical schemes 38
4.5.1 Upwind, central and blended schemes 38
4.5.2 High-order upwind schemes 39
4.6 Solution procedure 40
4.7 Implementation of LES boundary conditions 41
4.8 Implementation of numerical error assessment tools 41

5 Verification results: estimation of discretization errors 42
5.1 Simulation setup 42
5.2 Estimation of spatial discretization error (mesh sensitivity analysis) 43
5.3 Estimation of temporal discretization error (time step sensitivity analysis) 45
6 Simulations of laboratory-scale flames 46
6.1 Set of results 46
6.2 Highly stretched premixed methane-air jet flame (flame F2) 47
6.2.1 Experimental configuration 48
6.2.2 Simulation set-up 49
6.2.3 Isothermal flow - validation of boundary conditions 50
6.2.4 Reactive flow 52
6.3 Premixed methane-air swirl burner (flame PSF30) 64
6.3.1 Experimental configuration 65
6.3.2 Simulation set-up 66
6.3.3 Isothermal flow - validation of boundary conditions 68
6.3.4 Reactive flow 70
6.4 Discussion of results with comparative analysis between flames F2 and PSF30 83
7 Conclusions 86
Appendix A - Vortex method inflow boundary condition 87
Appendix B - 3D NSCBC boundary conditions 89
Appendix C - derivation of the flame controlling parameter F 91
Appendix D - source terms for residual error analysis 92
Bibliography 95
Curriculum vitae in English 104
Curriculum vitae in Croatian 105

Abstract

The main topic of this work's research is obtaining the methodological framework for large eddy simulation of turbulent premixed combustion. Obtaining this framework implies good knowledge of the state-of the-art in LES combustion, understanding the sub-grid scale (SGS) modelling of combustion and turbulent transport, proper definition of boundary conditions, quality mesh generation and proper numerical setup. In this work two different approaches have been used for SGS modelling of turbulent transport in Smagorinsky modelling framework. The first approach is the approach with constant value of Smagorinsky parameter. This approach is heavily relying on the chosen value of the parameter, which depends on flow configuration and simulation expertise and can introduce modelling errors if not chosen properly. Second approach is the Coherent Structure Method (CSM) approach, which is able to modify the Smagorinsky parameter according to the local coherence in the velocity field. Additionally, the CSM approach is in this work first-time used in the scope of the combustion modelling. The two approaches are mutually compared according to several criteria. The most significant comparison criteria is the comparison against available experimental data for two significantly different premixed combustion flames. The two approaches are also compared according to their level of numerical and discretization errors. Simulation results show that with the proposed methodological framework it is possible to get results which are comparable with experimental within approximately 20% of local discrepancy, with remark that CSM approach better reproduces fluctuations in the flow field. Furthermore, it is evaluated that probable cause of local discrepancy in validation comes from too excessive influence of combustion SGS modelling in regions of the flame front. This is directly related to insufficient resolution of the mesh resolution, even though the formal criteria of 80% of the resolved-to-total turbulent kinetic energy was satisfied. Conclusion is that the proposed methodological framework can be used for simulation of turbulent premixed combustion and that further improvement in result validation can be obtained by reducing the cell size in the flame region and further monitoring of numerical and discretization errors.

Keywords

Premixed combustion, turbulence modelling, large eddy simulation, turbulence inflow procedure, non-reflective boundary conditions, coherent structure method, highly stretched flames, swirl flames.

Sažetak

Tema ovog rada je dobivanje metodskog okvira za simulaciju turbulentnogpredmiješanog plamena u okviru simulacije velikih vrtloga (eng. *Large Eddy Simulation* - LES). To podrazumijeva dobro poznavanje područja istraživanja vezanih uz područje simulacije velikih vrtloga, poput istraživanja vezanih uz pod-mrežne modele izgaranja i turbulentnog transporta, utjecaja definicije rubnih uvjeta kao i numeričkih postavki simulacije te utjecaj kvalitete i rezolucije računalne mreže. U ovome radu je dana usporedba dva različita pristupa računanja pod-mrežnog turbulentnog transporta u Smagorinsky-evom modelskom okviru, od kojih se jedan po prvi puta koristi za potrebe simuliranja izgaranja te su njegove implikacije na model izgaranja u ovome radu po prvi puta istražene. Prvi pristup je uobičajeni pristup u kojemu je modelski parametar Smagorinsky-evog modela konstantan te ne ovisi o lokalnom toku već je uniforman u cijeloj domeni. Drugi pristup je metoda koherentnih struktura (eng. *Coherent Structure Method* - CSM), koji lokalno podešava parametar Smagorinsky-evog modela shodno lokalnoj koherentnosti u polju strujanja fluida. Dva pristupa su međusobno uspoređena prema nekoliko kriterija od kojih je najvažniji kriterij točnost rješenja usrednjenih i fluktuirajućih usporedbom s dostupnim eksperimentalnim podacima za dva značajno drugačija predmiješana plamena. Pristupi su također uspoređeni preko procjena grešaka diskretizacije te numeričkih grešaka. Rezultati pokazuju da je predloženim modelskim okvirima moguće dobiti zadovoljavajuća rješenja za značajno različite tipove plamena uz korištenje istih modelskih konstanti, uz napomenu da CSM pristup daje bolje rezultate fluktuirajućih veličina od pristupa sa uniformnim vrijednostima Smagorinsky-evog modelskog parametra. Nadalje, procjena je da najveći utjecaj na odstupanje od eksperimentalnih podataka uzrokuje preveliki utjecaj podmrežnog modela izgaranja, a koji je izravno vezan uz nedovoljnu rezoluciju mreže u području plamena iako je formalni kriterij od 80% izravnog riješenja u ukupnom zadovoljen za cijelu domenu. Zaključak je da predloženi modelski okvir može biti korišten u simulacijama predmiješanih turbulentnih plamenova te da se za daljnje povećanje razine točnosti rješenja predlaže korištenje finije mreže (u području plamena) od one koja je korištena u ovom radu.

Ključne riječi

Turbulentno predmiješano izgaranje, modeliranje turbulencije, metoda simulacije velikih vrtloga, turbulentni ulazni rubni uvjeti, ne-reflektivni rubni uvjeti, metoda koherentnih struktura, rastegnuti plamenovi, vrtložni plamenovi.

Prošireni Sažetak

Motivacija i generalni pregled

Turbulentno predmiješano izgaranje je vrlo učestali tip izgaranja u suvremenim komorama izgaranja, kako na laboratorijskim tako i na industrijskim razinama. Utjecaj turbulencije u polju strujanja svježe mješavine izravno utječe na turbulentnu brzinu izgaranja jer turbulencija uglavnom povećava površinu fronte plamena po jedinici volumena, čineći samu reakciju burnijom. Turbulencija u polju svježe mješavine može biti uzrokovana uzvodnim perturbacijama u polju brzina ili perturbacijama nastalim fizikalno-kemijskim promjenama u samoj fronti plamena. S obzirom na razinu detaljnosti u opisu turbulencije, u računalnoj dinamici fluida (eng. *Computational Fluid Dynamics* - CFD) razlikujemo tri glavna pristupa: pristup izravnog rješavanja turbulencije na računalnoj mreži (eng. *Direct Numerical Simulation* - DNS), pristup metodom simulacije velikih vrtloga (eng. *Large Eddy Simulation* - LES) i pristup modeliranjem u sklopu Reynoldsovih osrednjenih Navier-Stokesovih jednadžbi (eng. *Reynolds Averaged Navier-Stokes* - RANS). Trenutno je u industriji najčešće korišten RANS pristup zbog najmanjih računalnih zahtjeva ali i najvećim udjelom modeliranog u ukupnom rješenju što može rezultirati prevelikom ovisnošću rezultata o odabranim vrijednostima koeficijenata modela turbulencije. DNS pristup ne unosi u rješenje grešku modela turbulencije ali je zbog prevelikih računalnih zahtjeva trenutno ograničen samo na male domene i ne nalazi široku primjenu u industriji. LES pristup bi trebao dati točnija rješenja nego RANS pristup jer je kod njega ukupno rješenje dobiveno superpozicijom izravno rješenog i modeliranog djela, pri čemu modelirani dio ne bi smio biti dominatan. Sa pozicije računalnih resursa LES je zahtjevniji od RANS pristupa ali i dalje prihvatljiv za upotrebu u industriji. Upravo je LES u fokusu ovog rada, pri čemu će se pokušati prikazati njegova primjenjivost na primjeru simulacije jednog eksperimentalnog plamena, s obzirom na odabir tzv. pod-mrežnog modela.

Pregled trenutnih istraživanja

Svojstvo površinske gustoće plamena (eng. *Flame Surface Density* - FSD) u okviru metode simulacije velikih vrtloga (eng. *Large Eddy Simulation* - LES) je moguće izračunati pomoću algebarskih izraza ili transportne jednadžbe. Algebarski izrazi za računanje FSD su točni samo u slučaju kada su lokalna proizvodnja i disipacija FSD-a u ravnoteži. Za ostale slučajeve primjerenije je koristiti formu u kojoj se FSD računa pomoću transportne jednadžbe. Hawkes i Cant su prvi razvili transportnu jednadžbu za FSD pristup u LES okruzenju [1] na primjeru

slobodno-propagirajućeg trodimenzionalnog plamena. Od istih autora dolazi prva analiza FSD-LES pristupa pri kojoj su mijenjali ulaznu turbulenciju i veličinu LES-filtera [2]. Metoda koherentnih struktura (eng. Coherent Flame Model - CFM) bazira se na jednadžbi za FSD te postoje modeli za RANS i LES pristup. CFM pristup u LES okruženju je predstavljen u radu Richard i sur. [3] gdje se metoda naziva CFM-LES (naziv koji će se koristiti u ovom radu) te je korištena u simulaciji jednocilindričnog motora s unutašnjim izgaranjem. Slična analiza je provedena u radu Vermorel i sur. [4] gdje su autori CFM-LES metode proučavali varijabilnost u krivulji tlaka između deset uzastopnih ciklusa rada cilidra motora s unutrašnjim izgaranjem. Oba pristupa koriste rad Charlette i sur. [5] u kojem je predstavljen model za računanje pod-mrežne (eng. Sub-Grid Scale - SGS) turbulentne brzine koja doprinosi ukupnoj brzini reakcije kod predmiješanog izgaranja. Turbulentna brzina izgaranja je jedan od bitnijih parametara u analizi predmiješanih plamenova. Driscoll je istraživao strukturu predmiješanih plamenova te njihov utjecaj na turbulentnu brzinu izgaranja [6] te objavio opsežnu studiju o tome. Upravo je nakon implementacije CFM-LES modela u programski paket FIRE pokušana dobiti analiza turbulentne brzine izgaranja za slučaj siromašnih mješavina metana i zraka pri malim vrijednostima turbulencije. To je ujedno bio prvi pokušaj da se dobije analiza kvazi-stacionarnih plamenova CFM-LES metodom tijekom ovog istraživanja. Pokušalo se dobiti stabilnu kalkulaciju slučaja kojeg su eksperimentalno proučavali Savarianandam i Lawn [7] ali se plamen pokazao numerički vrlo nestabilan. Zbog toga je kao validacijski plamen u ovom radu izabran jako rastegnuti plamena [8] u kojem je prisutna jaka turbulencija. Isti plamen je već korišten za validaciju različitih modela izgaranja i tubulencije unutar RANS i LES metode [9] [10] i [11]. Izravnu usporedbu tri različita SGS modela izgaranja, za sličnu konfiguraciju plamena kao i [8], istražili su Hernandez-Perez i sur [12]..

Pored različitih pristupa za SGS izgaranje, treba razlikovati i različite model za SGS turbulentni transport koji također utječu na globalne karakteristike plamena. U ovome radu će se, između ostalog, nastojati prikazati kakav utjecaj donose različiti pristupi kod SGS transporta, a koji su uglavnom vezani na konstantu Smagorinsky-evog SGS modela. Nešto napredniji pristup kod modeliranja SGS turbulentnog transporta predstavlja model koherentnih struktura (eng. Coherent Structure Method - CSM), predstavljen u [13]. Ovaj pristup će također biti analiziran u ovom radu. Daljnja istraživanja CSM pristupa su pokazala da taj model daje gotovo jednako dobre rezultate kod LES simulacija strujanja u složenim geometrijama, kao i računalno znatno zahtjevniji dinamički model [14]. Također, CSM model je dokazan i u slučajevima

aerodinamičkih simulacija kod dobivanja koeficijenata otpora [15]. Dinamički model u ovoj disertaciji nije razmatran.

Vrlo važnu ulogu u LES simulacijama čine rubni uvjeti. U ovoj disertaciji od značenja su turbulentni rubni uvjeti na ulazu u domenu kao i prikladni ne-reflektivni rubni uvjeti na izlazu. Mathey i sur. su prikazali metodu izravnog zadavanja vrtloga na primjeru strujanja u cijevi i skokovite promjene u kanalu [16]. U ovome radu ova metoda je primjenjena na 2D simulacije u poglavljima koja se bave verifikacijskim testovima. Za realne laboratorijske plamenove, u ovoj disertaciji rubni uvjeti su dobiveni nekom od standardnih metoda kao što su mapiranje ili dovoljno uzvodno računanje strujanja. Dobar pregled ne-reflektivnih rubnih uvjeta za ulazne i izlazne rubne uvjete je dan u radu Lodato i sur. [17], čija je metoda korištena i u ovome radu implementacijom preko korisničkih funkcija.

Doprinos rada

Glavna namjera istraživanja ovog rada je dobivanje metode za simulaciju turbulentnog predmiješanog izgaranja u okviru simulacije velikih vrtloga. U okviru istraživanja prvi je puta primjenjena CSM metoda za modeliranje pod-mrežnog turbulentnog transporta za slučajeve simuliranja izgaranja turbulentnih predmiješanih plamenova. CSM metoda je pokazala značajnu prednost u odnosu na standarni Smagorinsky-ev pristup sa konstantnim modelskim parametrom, pogotovo pri validaciji fluktuirajućih veličina za dva različita turbulentna predmiješana plamena. Ovaj rad također donosi analizu grešaka koje svaka metoda računalne dinamike fluida intrinzično posjeduje. Greške se klasificiraju prema uzroku nastajanja a u ovom radu obavljena je procjena modelskih, numeričkih i diskretizacijskih grešaka metodama koje su već od ranije poznate i razvijene ali njima do sada nije analiziran utjecaj transportnih varijabli vezanih uz reaktivno strujanje, kao primjerice površinske gustoće plamena, varijable koja izravno ukazuje na položaj plamena u računalnoj domeni. Analiza grešaka, dobivena u ovome radu na laboratorijskim plamenovima, ukazuje na dominantne uzroke neslaganja rezultata simulacija sa eksperimentalnim podacima te daje vrijedne smjernice o kvalitenom postavljanju simulacija realnih industrijskih plamenova, čije komore izgaranja su nekoliko puta veće od plamenova prezentiranih u ovome radu.

Nomenclature

Roman	Description	Unit
a_T	Sub-grid scale straining of the flame	1/m
B	Channel height in swirl burner	m
Bl	Blint number	-
c	Reaction progress variable	-
c^*	Model parameter	-
C_2	CSM modelling parameter	
C_S	Smagorinsky model constant	-
C_{SGS}	General modelling parameter for SGS viscosity	
C_μ	Modelling parameter	-
D	Mass diffusivity	m^2/s
D_h	Hydraulic diameter	m
D_t	Turbulent scalar diffusivity	m^2/s
E	Velocity gradient tensor	1/s
E_M	Momentum error	m/s
f	Mixture fraction	-
F	Flame thickness correction	-
F_{CS}	Coherent structure function	
F_Ω	Energy decay suppression function	-
h	specific enthalpy	J/kg
H_L	Lower heating value of the fuel	J/kg
k	Turbulent kinetic energy	m^2/s^2
K_1	Modelling parameter in CFMLES	-
K_2	Modelling parameter in CFMLES	-
l_F	laminar flame thickness	m
l_{lon}	Longitudinal length scale	-
l_{lat}	Lateral length scale	-

l_q	local quench scale	m
Le	Lewis number	-
L_H	Enthalpy loss factor	-
m	Mass	kg
n	Number of channels in swirl burner	-
n_{res}	Modelling parameter in CFMLES	-
N	Number of turbulent structures (Vortex method)	-
N_i	Unit normal vector of the flame front	-
p	Static pressure	Pa
Pr	Prandtl number	-
P	Flame power	kW
r_0	Inner radius of swirl burner channel	m
R_0	Outer radius of swirl burner channel	m
$R_{ax,lon}$	Normalized longitudinal correlation of axial velocity	-
$R_{ax,lat}$	Normalized lateral correlation of axial velocity	-
$Q_{h,gas}^N$	Normal cubic meter of gas per one hour	m_N^3/h
$Q_{h,air}^N$	Normal cubic meter of air per one hour	m_N^3/h
Re	Reynolds number	-
Sc	Schmidt number	-
S	Stoichiometric fuel-to-air ratio	-
$S_{0,th}$	Theoretical swirl number	-
S_0	Actual (calculated) swirl number	-
S_{ij}	Velocity strain tensor	1/s
$S_{L,0}$	Laminar flame speed	m/s
$S_{L,m}$	Modified laminar flame speed	m/s
S_d	Displacement speed	m/s
Sc	Schmidt number	-
t	Time	s
u_i	Velocity vector	m/s

H	Total enthalpy	J
q	Enthalpy source	W
Q	Second invariant of the velocity flow field	
r	Radius (variable)	m
T	Temperature	K
T_{ad}	Adiabatic temperature	K
T^0	Fresh mixture temperature	K
u	Normal part of the velocity field	m/s
w	Tangential part of the velocity field	m/s
W_{ij}	Vorticity tensor	1/s
x_i	Position vector	m
y	Species mass fraction in SCRS model	-
Y	Species mass fraction	-
Y_F	Fuel mass fraction	-
Y_F^0	Initial fuel mass fraction	-
Y_r	Reduced fuel mass fraction	-

Greek	**Description**	**Unit**
α	Non-moveable block attack angle for swirl burner	rad
	Heat release factor	-
β	Reduced activation energy	-
β^*	model parameter	-
γ_q	Model parameter for enthalpy loss parameter	-
δ_{cn}	Natural flame brush thickness	m
δ_L	Laminar flame thickness	m
Δ_x	Spatial discretization (grid resolution)	m
$\hat{\Delta}$	Combustion filter size	m
ε	Turbulent dissipation rate	m^2/s^3
φ	Arbitrary scalar	-
ϕ	Equivalence ratio	-

Γ	Efficiency function	-
λ	Thermal conductivity	W/(mK)
μ	Dynamic molecular viscosity	Pas
μ_t	Turbulent viscosity	Pas
η	Kolmogorov length scale	m
ω	Chemical source term	kg/(m^{3}s)
ρ	Density	kg/m^3
σ	Turbulent structure length scale (Vortex method)	
Σ	Flame surface density	1/m
τ	Modelling parameter	-
τ_c	Chemical time scale	s
τ_e	Residence time	s
τ_t	Turbulent integral time	s
τ_v	Turbulent structure lifetime (Vortex method)	s
τ_{ij}	Tangential stress tensor	N/m^2
τ_η	Kolmogorov time	s
θ	Reduced temperature	-
υ	kinematic viscosity	m^2/s
ξ	Attack angle of swirl burner's moveable block	rad
ξ_m	Maximum attack angle of swirl burner's moveable block	rad
Ξ	Wrinkling factor	-

Subscripts	**Description**
res	Resolved
SGS	Sub-grid scale
fr	Fresh-side
fu	Fuel
u	Unburned
b	Burned, boundary
tot	Total
init	Initial

Superscripts	**Description**
lam	Laminar
'	Fluctuating

Math. symbols	**Description**
e=2.71828...	Euler's number
π=3.14159...	number pi

Overbars	**Description**
$\tilde{\phi}$	Favre averaged, directly resolved value
$\bar{\phi}$	Reynolds averaged, cell-averaged value
$\hat{\phi}$	second (test) filtered value

Abbreviations	**Description**
1D, 2D, 3D	One-, two-, three- dimensional
RANS	Reynolds averaged Navier-Stokes
LES	Large eddy simulation
LUDS	Linear Upwind Differencing Scheme
SGS	Sub-grid scale
RES	Resolved
CDF	Central differencing scheme
CFM	Coherent flame model
CSF	Coherent structure function
CV	Control volume
CSM	Coherent structure model
FSD	Flame surface density

CBC	Convection boundedness criteria
CURV	Flame curvature
PROP	Flame propagation
PSF	Premixed swirling flame
PSD	Power spectra density
ROHR	Rate of heat release
STR	Flame straining
SMART	Sharp and Monotonic Algorithm for Realistic Transport
SCRS	Simple chemically-reacting system
RMS	Root mean squared
RPV	Reaction progress variable
QUICK	Quadratic Upwind Interpolation for Convective Kinematics
TVD	Total variation diminishing concept
UDS	Upwind differencing scheme
FV	Finite volume
NSCBC	Navier-Stokes continuous boundary conditions

List of Figures

Figure 1 - Schematic representation of turbulence-flame interaction. 3
Figure 2 - Illustration of an overall model for unsteady simulations [20] 3
Figure 3 - Idealized spectrum of turbulent kinetic energy of isotropic turbulence with respect to the wavenumber (Fourier space) and the schematic of the extent of modelling employed by the DNS, LES and RANS [23] 5
Figure 4 - Implicit filtering and cut-off scales in physical space 6
Figure 5 - Instantaneous profile decomposed into mean and fluctuating part 7
Figure 6 - Regions of LES and RANS framework in hybrid approach 14
Figure 7 - Combustion regime diagram. (Source: Schneider, Dreizler and Janicka in 2005 [51]) 19
Figure 8 - Actual flame thickness over LES grid (left); artificial spreading of the flame over LES grid (middle); flame thickened over LES filter size – combustion filter (right) 21
Figure 9 - Graphical representation of flame controlling parameter F (the F-diagram) 22
Figure 10 - Displacement speed and normal to the flame front pointing towards fresh gases. 24
Figure 11 - Laminar flame speed obtained from GRI-MECH 3.0 mechanism [63] in PREMIX [59] solver 26
Figure 12 - Schematic representation of VM applied on inlet boundary condition. Streamwise flow is in the direction of orientation vector 28
Figure 13 - 3D visualization of velocity magnitude in a few typical cross sections and iso-surface of k=0.2 for two values of *k* applied on VM. Turbulent structure size is the same in both cases 29
Figure 14 - Qualitative representation of static pressure outflow: (a) reflective outflow; (b) - non-reflective outflow. 30
Figure 15 - Control volume (arbitrary polyhedron) 37
Figure 16 - Schematic view of boundary conditions used in verification tests 42
Figure 17 - Time-integrated deviation for the three mesh resolutions 43
Figure 18 - Instantaneous values of FSD for the three mesh sizes 44
Figure 19 - Instantaneous values of temperature for the three mesh sizes 44
Figure 20 - Instantaneous values of C_s for the three mesh sizes 45
Figure 21 - Time integrated deviation for the three different time-steps 45
Figure 22 - Combustion regime diagram for flame F2 with plotted lines separating the regimes 47

Figure 23 - Schematic view of the experimental configuration (left) and recorded average temperature field (right); (Source: Chen et al. [8]) 48
Figure 24 - Normalized mean and RMS velocity profiles at burner exit plane. (Source: Chen et al. [8]) 49
Figure 25 - Mesh and inlet configuration for Chen case. 50
Figure 26 - Computational domain representing channel attached to the burner. Channel is used to generate velocity and turbulence field for the burner zone. 51
Figure 27 - Flame F2: Mean and RMS values of axial (U) and tangential (W) velocity on three axial positions near the nozzle exit (1, 10 & 20 mm) for isothermal flow 51
Figure 28 - Flame F2: Axial distribution of axial velocity and turbulent kinetic energy, normalized by mean axial velocity for isothermal flow 52
Figure 29 - Flame F2: Comparison of instantaneous temperature field; C_s=f(CSM) (a); C_s=0.1 (b) and C_s=0.2 (c) 53
Figure 30 - Flame F2: Comparison of instantaneous reaction rate field; C_s=f(CSM) (a); C_s=0.1 (b) and C_s=0.2 (c). 53
Figure 31 - Flame F2: Iso-surface of instantaneous reaction rate (left) and streamlines at nozzle entrance to the combustion chamber (right) 54
Figure 32 - Flame F2: mean and RMS of reaction progress variable. 55
Figure 33 - Flame F2: mean CH4 and CO2 species. 56
Figure 34 - Flame F2: mean and RMS velocity field. RMS velocity field represents resolved turbulence. 57
Figure 35 - Flame F2: scatter plots of cell values for resolved vs. SGS FSD source terms, coloured by RR for $C_s=0.1$, $C_s=0.2$ & $C_s=f(CSM)$ 58
Figure 36 - Flame F2: scatter plots of cell values for RR vs. RPV, coloured by vorticity, for $C_s=0.1$, $C_s=0.2$ & $C_s=f(CSM)$ 59
Figure 37 - Flame F2: scatter plots of cell values for controlling factor F vs. RPV, coloured by RR for $C_s=0.1$, $C_s=0.2$ & $C_s=f(CSM)$ 59
Figure 38 - Flame F2: cell values of controlling factor F for $C_s=0.1$, $C_s=0.2$ & $C_s=f(CSM)$; lines are different parameters of $\hat{\Delta}/\Delta_x$ 60
Figure 39 - Flame F2: scatter plots of cell values for δ_q/δ_t ratio vs. RPV, coloured by RR; horizontal line represents limit where $\delta_q/\delta_t = 1$ (above that limit flame quenching can be expected) 60

Figure 40 - Flame F2: scatter plot of cell values for Smagorinsky parameter C_S vs. vorticity for $C_s=f(CSM)$, coloured by RPV 61
Figure 41 - Flame F2: scatter plots of cell values for resolved vs. SGS turbulent kinetic energy for $C_s=0.1$, $C_s=0.2$ & $C_s=f(CSM)$; line represents equality between resolved and SGS TKE 62
Figure 42 - Flame F2: scatter plots of cell values for FSD vs. momentum normalized residual errors, coloured by RPV, for $C_s=0.1$, $C_s=0.2$ & $C_s=f(CSM)$; lines in upper diagrams represents error of 1% (1% slope), while in lower diagrams line represents equality between cell values of relative errors (slope =1) 62
Figure 43 - Combustion regime diagram for flame PSF30 with plotted lines separating the regimes 64
Figure 44 - Schematic view of the experimental configuration. (Source: Schneider, Dreizler and Janicka in 2005 [51]) 65
Figure 45 - Computational mesh for TECFLAM laboratory flame; swirler is included in the domain 66
Figure 46 - Theoretical swirl number as a function of the angle of PSF' burner moveable block. 67
Figure 47 - 3D representation of the swirler with two inlets and axes of cylindrical coordinate system 68
Figure 48 - TECFLAM isothermal flow: Mean and RMS values of axial (U) and tangential (W) velocity on three axial positions near the nozzle exit. 69
Figure 49 - Flame PSF30: qualitative difference in fields of temperature between C_s=f (CSM) (a), C_s=0.1 (b) and C_s=0.2 (c) 70
Figure 50 - Flame PSF30: qualitative difference in fields of reaction rate between C_s=f (CSM) (a), C_s=0.1 (b) and C_s=0.2 (c) 70
Figure 51 - Flame PSF30: Iso-surface of instantaneous reaction rate (left) and streamlines at nozzle entrance to the combustion chamber (right) 71
Figure 52 - Colourless instantaneous isosurface of reaction rate at value of 0.1 J/s (left) and isosurface of same reaction rate coloured by axial velocity for the case of CSM turbulent transport for the flame PSF-30 (right). 71
Figure 53 - Instantaneous and mean CH4 mass fraction 72
Figure 54 - Instantaneous and mean CO2 mass fraction 72
Figure 55 - Flame PSF30: mean and RMS of temperature at different axial distances from the inlet to combustion chamber 73

Figure 56 - Flame PSF30: mean and RMS of CH4 and CO2 at different axial distances from the inlet to combustion chamber. 74
Figure 57 - Flame PSF 30: mean and RMS of axial and radial velocity at several axial positions 75
Figure 58 - Flame PSF 30: mean and RMS of tangential velocity at several axial positions. . 77
Figure 59 - Flame PSF30: scatter plots of cell values for resolved vs. SGS FSD source terms, coloured by RR for $C_s=0.1$, $C_s=0.2$ & $C_s=f(CSM)$ 78
Figure 60 - Flame PSF30: scatter plots of cell values for RR vs. RPV, coloured by vorticity, for $C_s=0.1$, $C_s=0.2$ & $C_s=f(CSM)$ 78
Figure 61 - Flame PSF30: scatter plots of cell values for controlling factor F vs. RPV, coloured by RR for $C_s=0.1$, $C_s=0.2$ & $C_s=f(CSM)$ 79
Figure 62 - Flame PSF30: cell values of controlling factor F for $C_s=0.1$, $C_s=0.2$ & $C_s=f(CSM)$; lines are different parameters of $\hat{\Delta}/\Delta_x$ 79
Figure 63 - Flame PSF30: scatter plots of cell values for δ_q/δ_t ratio vs. RPV, coloured by RR; horizontal line represents limit where $\delta_q/\delta_t = 1$ (above that limit flame quenching can be expected) 80
Figure 64 - Flame PSF30: scatter plot of cell values for Smagorinsky parameter C_S vs. vorticity for $C_s=f(CSM)$, coloured by RPV 80
Figure 65 - Flame PSF30: scatter plots of cell values for resolved vs. SGS turbulent kinetic energy for $C_s=0.1$, $C_s=0.2$ & $C_s=f(CSM)$; line represents equality between resolved and SGS TKE 81
Figure 66 - Flame PSF30: scatter plots of cell values for FSD vs. momentum normalized residual errors, coloured by RPV, for $C_s=0.1$, $C_s=0.2$ & $C_s=f(CSM)$; lines in upper diagrams represents error of 1% (1% slope), while in lower diagrams line represents equality between cell values of relative errors (slope =1) 82

List of Tables

Table 1 - SGS model parameters and corresponding values 25
Table 2 - Meshes used in estimation of discretization errors 42
Table 3 - Parameters for three different premixed highly stretched flames. 49
Table 4 - parameters for inlet boundary conditions for flame F2 50
Table 5 - Integral values of resolved-to-total ratio and cell residuals for turbulent kinetic energy and FSD (for cell residuals, only cells with RR>0 are taken into account) 63
Table 6 - Different premixed swirling flames (PSF) investigated on the unconfined swirl burner. 66
Table 7 - Integral values of resolved-to-total ratio and cell residuals for turbulent kinetic energy and FSD (for cell residuals, only cells with RR>0 were taken into account) 82
Table 8 - Comparison between flame F2 and PSF30 by validation against experimental data and error assessment 84

1 Introduction

1.1 Motivation, general overview and state-of-the-art in LES research

Turbulent premixed combustion is one of the main divisions in the field of combustion, both on the laboratory and the industrial scale. When considering the premixed flame, turbulence on the side of the fresh mixture influences the reaction rate by increasing the flame front per unit volume. Fresh mixture turbulence can be caused by upwind perturbations of velocity field, as well as perturbations as a consequence of the physical changes in the flame front itself. Considering the level of detail in description of turbulence in computational fluid dynamics (CFD), three main approaches can be distinguished: direct numerical simulation (DNS), large eddy simulation (LES) and Reynolds-averaged Navier-Stokes (RANS) approach. Currently, RANS is the preferable choice in industry due to the lowest computational resources when compared to other approaches, but has a drawback that all turbulent scales are by definition modelled and solution is very dependent to turbulence models' closure coefficients. DNS approach, on the other hand, does not introduce modelling uncertainties into the solution, but due to large demand for computational resources it still remains impractical choice for industry. LES provides results which are superimposed from both the modelled or sub-grid scale (SGS) and the resolved part, with resolved part dominant in most of the domain. From the computational resources' point of view, LES needs more resources than RANS, but less than DNS and this makes it feasible approach for industry. It is LES approach which is in the focus of this research. The aim of this research is to explore few different options in LES from SGS and resolution point of view, with an application to turbulent premixed combustion modelling.

Flame surface density (FSD) can be calculated in LES framework in two different ways: algebraically and from the transport equation. Algebraic expression can be used when local production and destruction of FSD are in balance. For strongly unbalanced cases, separate transport equation is necessary. Hawkes and Cant were the first to introduce transport equation for FSD in LES framework [1] and verified it on the example of freely-propagating three dimensional flame. Same authors have performed the first analysis of FSD LES approach with varying inflow turbulence intensity and SGS filter size [2]. Coherent flame model (CFM) is based on the equation for FSD and there are variants for both RANS and LES approach. CFM approach in LES framework is introduced in work of Richard et al. [3], representing the simulation of single-cylinder internal combustion engine, where this approach is abbreviated as CFMLES (abbreviation which will be used in this work). Similar analysis was performed by

Vermorel et al. [18], where authors have used CFMLES approach for simulation of cycle-to-cycle variability for the same case. Both approaches use SGS wrinkling model for turbulent premixed combustion introduced by Charlette et al. [5]. Turbulent flame speed is one of the criteria used in analysis of turbulent premixed flames. Driscoll published extensive analysis of flame structure and its influence on turbulent flame speed [6]. One of the first attempts of obtaining the proper turbulent flame speed in this research was the case of lean methane-air weakly wrinkled premixed combustion experimentally done by Savarianandam and Lawn [7]. Calculations were unsuccessful due to the frequent flame extinction. Du to that, as a validation flame in this work highly stretched flame of Chen et al. [8] is chosen. Same experiment has already been used for validation of several turbulent combustion models, both in RANS and LES framework [9] [10] [11]. Direct comparison for three different SGS combustion models was provided by Hernandez-Perez et al. [12] for the similar flame as the one in [8].

Apart from the different approaches for SGS combustion, one should distinguish between different approaches in SGS turbulent transport, which can also influence the global flame characteristics. In this work a standard Smagorinsky and more advanced SGS model for turbulent transport will be combined with CFMLES approach, in order to investigate possible benefits/drawbacks of specific configuration. Advanced SGS model is the one introduced by Kobayashi and is called coherent structure method (CSM) [13]. It recognizes coherent structures in the flow and modifies Smagorinsky coefficient according to the coherent structure function. Investigations of CSM SGS approach have shown that this model gives results which are comparable with more resource-demanding dynamic model [14]. Moreover, the use of CSM method has been successful in obtaining the sufficiently correct drag coefficient in cases of aerodynamic flow over the cylinder [15]. Dynamic model is not considered in this work.

Definitions of boundary conditions for LES framework are different than for the RANS. Since the nature of LES is different than the one in RANS simulations, this also reflects in definition of boundary conditions. This means that great portion of turbulence on the inlet should be directly defined and that pressure oscillations on the inlet and outlet should not be reflected back into the domain. In this work only the use of most physically defined inflow and outflow boundary conditions is an option, in order to reduce the influence of boundary conditions on the results. Mathey et al. [16] have introduced the Vortex method, which imposes the vortices directly at the inlet of domain and successfully validated this approach for turbulent channel flow and backward facing step. In this work this method will be modified and used as the

turbulent inflow generator for 2D verification simulations. Good overview of non-reflective boundary conditions for inlet/outlet is given by Lodato et al. in [17].

LES is by a factor of 10 to 100 more costly than RANS computations [19]. However, this is the trade-off which user has to make in return for higher accuracy. Turbulent premixed combustion is a very complex phenomena and turbulence-flame interaction can result in both increase in reaction rate or flame quenching due to excessive flame stretch. Locally, these phenomena can be captured with LES, as shown in this work. Interaction between combustion, continuum flux and turbulence is shown schematically in Figure 1.

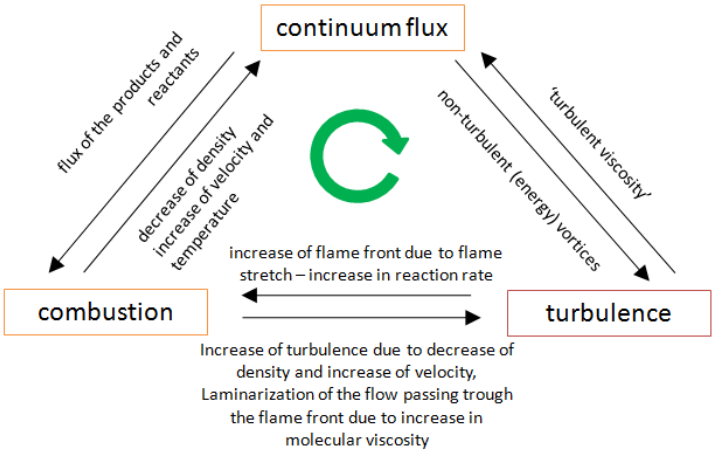

Figure 1 - Schematic representation of turbulence-flame interaction.

The most important role of the turbulence modelling is to provide turbulent viscosity to account mixing in scales smaller than grid resolution.

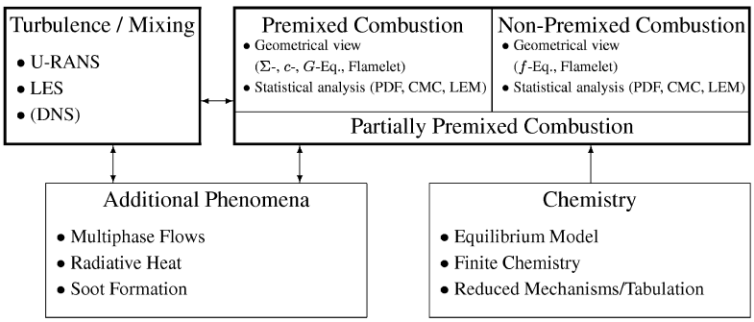

Figure 2 - Illustration of an overall model for unsteady simulations [20]

Combustion modelling frameworks can be divided into few groups, depending on the levels of resolved/modelled levels of turbulence, type of the flame (premixed, non-premixed or partially premixed) or tracking of the flame front (direct tracking of the flame geometry of statistical analysis). The complete division is given in Figure 2. In this work Coherent Flame Model is used.

1.2 Work hypothesis and outline

Knowledge of sub-grid scale turbulence models is one of the crucial steps in understanding the overall method of simulation of turbulent premixed flames within the framework of large eddy simulation. By introducing the more advanced SGS models with the ability of recognizing coherent structures in the flow, like coherent structure method (CSM), and by using the proper definition of boundary conditions, it is possible to get good validation of results for a wide span of laboratory flames with different levels of turbulence by using the same model setup. This makes the overall approach suitable for simulation of different levels of turbulence and transition periods in real combustion chambers.

1.3 Thesis contribution

It is expected that this research will result in better understanding of interaction between SGS turbulent transport model and flame behaviour within the framework of LES, especially for determining local flame phenomena, like flame quenching. This research uses, for the first time, CSM turbulent transport approach for simulation of turbulent premixed flames. The positive effect of using the CSM over standard Smagorinsky is especially seen in validation of turbulent fluctuation for two laboratory flames simulated in this work. This work can be seen as an attempt to find the method capable for capturing correctly a wide range of flames with the unique method framework. This work also presents error analysis. Errors were analysed by the known methods, but applied for the first time on transported values resulting from combustion modelling, like FSD. This analysis can be a valuable input in setting guidelines for proper LES setup for real-world industrial burners.

2 Mathematical method in LES framework

A mathematical model consists from conservation equations for mass, linear momentum, energy and scalars, as well as constitutional relations. A conservation equation for angular momentum is not solved since the modelling framework assumes that the stress tensor is symmetric [21]. Before going into detailed description of the model, general reasoning on the LES framework is given.

Qualitative features of turbulent flows possess spatial-temporal randomness, irregularity, strong interaction between different scales, dissipation and diffusion [22] In order to enable development of turbulence models, Richardson-Kolmogorov turbulent cascade is adopted. It says that turbulence can be presented by eddies of different sizes that may be broken into smaller eddies that retain kinetic energy of the broken larger eddies, i.e. smaller eddies inherit energy from larger eddies. In this way energy is passed down from large to small scales of motion. Kolmogorov (papers in Russian - Kolmogorov 1941 a, b) predicted a scale, called Kolmogorov scale, at which kinetic energy is dissipated due to viscosity. Between the large scales and the Kolmogorov scale, turbulent kinetic energy is transferred towards smaller eddies without dissipation. Energy is dissipated at smaller scales, close to Kolmogorov scale, where viscosity effects take place. Range with energy cascade without dissipation is called inertial subrange and generally can be few orders of magnitude for high Re number. Theoretical (idealized) energy decay in Fourier space is presented in Figure 3.

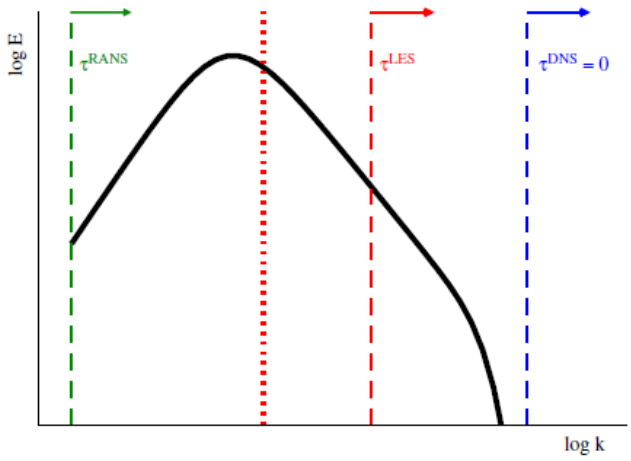

Figure 3 - Idealized spectrum of turbulent kinetic energy of isotropic turbulence with respect to the wavenumber (Fourier space) and the schematic of the extent of modelling employed by the DNS, LES and RANS [23]

LES framework based on filtering concept is introduced by Leonard in 1974 [24]. Filtering can be performed explicitly or implicitly. In implicit filtering ratio of filter width to step size of the grid is equal to one. This means that step size of the grid determines the filter cut-off scale. If the grid is refined, cut-off scale is shifted towards smaller eddies (higher wavenumbers). Theoretically, if $\Delta \to 0$, then SGS part of the solution vanishes and modelling framework switches to DNS. LES framework implies that the solution obtained from the simulation is partly directly resolved on the grid and partly obtained by the SGS model. By observing Figure 3, it means that all scales left from LES cut-off are solved directly on the grid (therefore grid has to have spatial resolution as cut-off scale), while all scales right from LES cut-off need modelling. Schematic view of the cut-off scales for three different frameworks (DNS, LES and RANS) in physical space is presented in Figure 4.

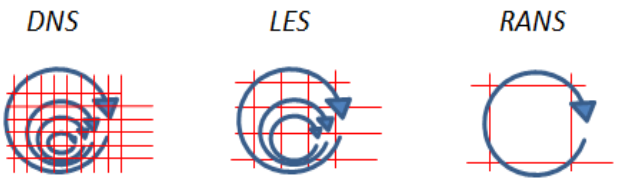

Figure 4 - Implicit filtering and cut-off scales in physical space

Cut-off length scale is called filter length scale and all solution corresponding to characteristic sizes below the filter is called Sub-filter scale (SFS). In this work, the computational grid itself is a filter so SFS values will be denoted as SGS values or SGS part of the solution, where grid is implicitly accounted as the filter (implicit filtering). This is why special attention has to be taken to the resolution of computational grid. Due to limitations from computational resources, high resolution might not be employed everywhere. However, it should be employed locally where specific phenomena of interest might occur, like area between nozzle and flame, flame front etc. In LES, SGS models should explicitly contain information about the local mesh size Δ_x [25].

2.1 Reynolds and Favre averaging

Calculating all turbulent scales directly on the computational grid, the DNS framework, requires very fine mesh resolution (on the order of Kolmogorov spatial scale) and consequently large amount of computational cells. This implies the need for very high computational resources which makes the DNS approach very expensive and limited to simple cases [26] [27] [28]. At present, the meshes describing the real industrial geometries have their spatial resolution much smaller than the Kolmogorov scale. The common approach is then to solve averaged instead of the exact equations [29], [30]. Each instantaneous quantity can be decomposed into its ensemble mean and fluctuating part (Eq. ((2-1)).

$$\varphi = \overline{\varphi} + \varphi' \tag{2-1}$$

Graphical representation of the above equation is presented in Figure 5. The average fluctuation is zero, i.e. $\overline{\varphi'} = 0$.

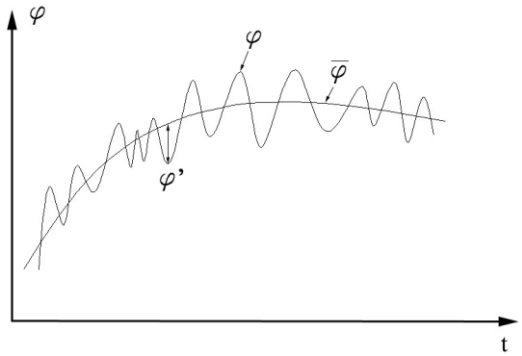

Figure 5 - Instantaneous profile decomposed into mean and fluctuating part

Averaged quantities are varying smoothly in time and they are much easier to solve (on larger mesh resolution and larger time step). In the classical RANS concept the averaged equations are obtained by inserting Eq. ((2-1) for dependent variables into the leading instantaneous equations, like Navier-Stokes or energy equation, and by closing the correlations that emerge because of averaging with some specific models. In configurations with strong density variations, on the other hand, the more appropriate averaging procedure is that based on the Favre averaging [31], [32]. Density fluctuations are observed in turbulent flames because of the thermal heat release. The Favre mean is defined as:

$$\tilde{\varphi} = \frac{\overline{\rho\varphi}}{\bar{\rho}} \tag{2-2}$$

The Favre fluctuation is defined as $\varphi'' = \varphi - \tilde{\varphi}$, where $\tilde{\varphi}'' = 0$. An advantage of the Favre averaging over the Reynolds averaging is in a lesser number of unclosed correlation terms that appear as a consequence of averaging procedure in the case with variable density [31]. Favre averaged equations are formally identical with Reynolds averaged equations and can be solved with the same solvers [31].

2.2 Implicit filtering in Large Eddy Simulation

In LES, the relevant instantaneous quantities φ are filtered either in spectral space or physical space. The Favre filtering operation can be defined as [31]:

$$\bar{\rho}\tilde{\varphi} = \int \rho\varphi(x^*)F(x - x^*)dx \tag{2-3}$$

In equation (2-3) F represents the LES filter. Tilde above the quantity symbol denotes Favre filtered part of the instantaneous quantity φ and its mathematical formalism is not the same as in the case of conventional Favre averaging in RANS. In physical space a box filter can be defined:

$$F(x) = \begin{cases} 1/\Delta^3 & if \quad |x_i| \le \Delta/2, i = 1,2,3 \\ 0 & otherwise \end{cases} \tag{2-4}$$

This filter corresponds to an averaging of the φ over a box of size Δ.

Each instantaneous quantity can be decomposed into a filtered component $\tilde{\varphi}$ and a fluctuating part φ'' similar according to Eq. (2-1). The difference between filtering and Favre (Reynolds) averaging is that $\tilde{\varphi}'' \neq 0$ and $\tilde{\tilde{\varphi}} \neq \tilde{\varphi}$ [31]. Derivations are given below. Favre-filtered fluctuation can be expressed as:

$$\begin{aligned} \tilde{\varphi}''(x) &= \int \left[\varphi(x^*) - \tilde{\varphi}(x^*)\right]F(x - x^*)dx^* \\ &= \int \varphi(x^*)F(x - x^*)dx^* - \int \tilde{\varphi}(x^*)F(x - x^*)dx^* \\ &= \tilde{\varphi}(x) - \tilde{\tilde{\varphi}}(x) \end{aligned} \tag{2-5}$$

Filtering of the Favre filtered quantity will not result in original Favre-filtered value:

$$\begin{aligned}\tilde{\tilde{\varphi}}(x) &= \int \underbrace{\left[\int \varphi(x^+) F(x^+ - x^*) dx^+\right]}_{\tilde{\varphi}(x)} F(x - x^*) dx^* \\ &= \underbrace{\int\int \varphi(x^+) F(x^+ - x^*) F(x - x^*) dx^+ dx^*}_{\neq \tilde{\tilde{\varphi}}(x)}\end{aligned} \tag{2-6}$$

Furthermore, the derivation of balance equations for the Favre (or Reynolds) filtered quantities requires the exchange of filtering and derivation operators. In most simulations, the uncertainties due to this exchange are neglected and assumed to be built in SGS modelling [31], [33].

As an example of filtering procedure, filtering of the convective term of instantaneous scalar equation is given:

$$\frac{\partial(\bar{\rho}\widetilde{u_j\varphi})}{\partial x_j} \xrightarrow{filtering} \frac{\partial(\bar{\rho}\tilde{u}_j\tilde{\varphi})}{\partial x_j} - \frac{\partial}{\partial x_j}\left(\bar{\rho}\left(\tilde{u}_j\tilde{\varphi} - \widetilde{u_j\varphi}\right)\right) \tag{2-7}$$

Set of instantaneous balance equations is filtered by the instantaneous quantity and appropriate model closures have to be introduced.

2.3 Conservation equations in LES framework

Basic set of equations governing the fluid flow are given by applying the conservation laws to the fluid passing infinitesimally small control volume. For deeper insight and derivation one is referred to standard literature on this topic [34], [30], [35], [36] and [37]. Eulerian frame of reference is applied and Einstein's summation convention is applied over the repeated indices of the Cartesian components [35]. Here, only the differential equations in the final pre-implementing form are given.

2.3.1 Conservation of mass

Conservation of mass states that any net flux on the CV through its boundaries is followed by the changes in density. Favre filtered form of continuity equation is:

$$\frac{\partial(\bar{\rho})}{\partial t} + \frac{\partial}{\partial x_i}(\bar{\rho}\tilde{u}_i) = 0 \tag{2-8}$$

The equation of continuity, as given in Eq. (2-8), is valid for both single- and multi-component systems [37].

2.3.2 Conservation of momentum

Conservation of momentum for isotropic Newtonian fluid is represented by the Favre-filtered Navier-Stokes vector equation:

$$\frac{\partial(\bar{\rho}\tilde{u}_j)}{\partial t}+\frac{\partial(\bar{\rho}\tilde{u}_j\tilde{u}_i)}{\partial x_j}=\frac{\partial}{\partial x_j}\left(\bar{\rho}\left(\widetilde{u_j u_i}-\tilde{u}_j\tilde{u}_i\right)\right)-\frac{\partial p}{\partial x_j}+\frac{\partial}{\partial x_j}\left(\mu\frac{\partial(\bar{\rho}\tilde{u}_i)}{\partial x_j}\right) \tag{2-9}$$

Equation (2-9) basically means that the local change of momentum is balanced with fluid's local flux (the convection and diffusion) and external surface forces acting on the fluid. Mass forces are neglected from the consideration, since only gaseous phases are going to be considered. Buoyancy forces are also neglected, since flame behaviour is explored in the proximity of the burner nozzle, where pressure forces and convective flux are dominant.

The first term on the right hand side $\left(\widetilde{u_j u_i}-\tilde{u}_j\tilde{u}_i\right)$ is modelled by a SGS turbulence model. The detailed description on modelling the SGS terms is in given in Chapter 2.4. Here only the final equation is presented:

$$\frac{\partial(\bar{\rho}\tilde{u}_j)}{\partial t}+\frac{\partial}{\partial x_j}\left(\bar{\rho}\tilde{u}_i\tilde{u}_j\right)=-\frac{\partial\bar{p}}{\partial x_j}+\frac{\partial}{\partial x_j}\left((\mu+\tilde{\mu}_t)\frac{\partial(\bar{\rho}\tilde{u}_i)}{\partial x_j}\right) \tag{2-10}$$

Viscosity, representing the diffusion coefficient, is consisting of molecular viscosity μ (property of the fluid) and turbulent viscosity $\tilde{\mu}_t$ (property of the flow). Turbulent viscosity is an artificial viscosity, representing equivalent dissipation of unresolved (SGS) scales of motion. Modelling of turbulent viscosity is given in Chapter 2.4. In equation for conservation of momentum, written in the form as in Eq. (2-10), fluid's bulk viscosity is neglected.

2.3.3 Conservation of energy

Conservation of energy in Favre filtered framework is represented by the following transport equation for the specific enthalpy [34]:

$$\frac{\partial(\bar{\rho}\tilde{h})}{\partial t}+\frac{\partial(\bar{\rho}\tilde{u}_j\tilde{h})}{\partial x_j}=\frac{\partial}{\partial x_j}\left(\bar{\rho}\left(\widetilde{u_j h}-\tilde{u}_j\tilde{h}\right)\right)+\frac{\partial p}{\partial t}+\frac{\partial}{\partial x_j}\tilde{u}_i\tau_{ij}+\frac{\partial}{\partial x_j}\left(\lambda\frac{\partial\tilde{h}}{\partial x_j}\right)+\bar{\rho}\dot{q} \tag{2-11}$$

Local change of the specific enthalpy is equal to the specific enthalpy flux (convection and diffusion) balanced by temporal pressure gradients (first term on r.h.s.), viscous heating (second term on r.h.s.) and specific enthalpy contribution due to external sources $\dot{q}$. In our case, external sources will be releasing of the heat contained in fresh mixture due to combustion. The

unclosed term on the right hand side $\left(\widetilde{u_j h} - \tilde{u}_j \tilde{h}\right)$ has to be closed. Usually it is closed by using gradient assumption:

$$\widetilde{u_j h} - \tilde{u}_j \tilde{h} = \frac{\tilde{\mu}_t}{\bar{\rho} Pr} \frac{\partial \tilde{h}}{\partial x_j} \tag{2-12}$$

where Pr is the Prandtl number. By using gradient assumption, problems arising from cross-diffusion are eliminated by the expense of the accuracy and the physical representation. The SGS viscosity is estimated from the unresolved turbulent transport, see Chapter 2.4. Final form of Favre filtered energy equation is given:

$$\frac{\partial\left(\bar{\rho}\tilde{h}\right)}{\partial t} + \frac{\partial}{\partial x_j}\left(\bar{\rho}\tilde{u}_j \tilde{h}\right) = +\frac{\partial \bar{p}}{\partial t} + \frac{\partial}{\partial x_j}\tilde{u}_i \tau_{ji} + \frac{\partial}{\partial x_j}\left(\left(\lambda + \tilde{\lambda}_t\right)\frac{\partial \tilde{h}}{\partial x_j}\right) + \bar{\rho}\dot{q} \tag{2-13}$$

Thermal diffusion is consisting from molecular thermal diffusion λ and turbulent thermal diffusion $\tilde{\lambda}_t = \tilde{\mu}_t / \left(\bar{\rho}\,\mathrm{Pr}\right)$.

2.3.4 Scalar transport

Scalar property φ can be species mass fraction, mixture fraction or flame surface density. A generic transport equation in Favre-filtered form for any arbitrary scalar φ is given by the following equation [34]:

$$\frac{\partial(\bar{\rho}\tilde{\varphi})}{\partial t} + \frac{\partial\left(\bar{\rho}\tilde{u}_j\tilde{\varphi}\right)}{\partial x_j} = \frac{\partial}{\partial x_j}\left(\bar{\rho}\left(\widetilde{u_j\varphi} - \tilde{u}_j\tilde{\varphi}\right)\right) + \bar{\rho}\dot{\tilde{\varphi}} \tag{2-14}$$

In the former equation the unresolved scalar transport $\left(\widetilde{u_j\varphi} - \tilde{u}_j\tilde{\varphi}\right)$ is also modelled by gradient assumption.

$$\widetilde{u_j\varphi} - \tilde{u}_j\tilde{\varphi} = \frac{\tilde{\mu}_t}{\bar{\rho}\mathrm{Sc}} \frac{\partial \tilde{\varphi}}{\partial x_j} \tag{2-15}$$

Finally, the scalar equation in Favre-filtered framework can be written in the following form:

$$\frac{\partial\left(\bar{\rho}\tilde{\varphi}\right)}{\partial t} + \frac{\partial}{\partial x_j}\left(\bar{\rho}\tilde{u}_j\tilde{\varphi}\right) = \frac{\partial}{\partial x_j}\left(\bar{\rho}\left(D + \tilde{D}_t\right)\frac{\partial \tilde{\varphi}}{\partial x_j}\right) + \bar{\rho}\,\dot{\tilde{\varphi}} \tag{2-16}$$

Diffusion coefficient consists from mass diffusion D (scalar diffusing with mass) and turbulent diffusion $\tilde{D}_t = \tilde{\mu}_t / \left(\bar{\rho} Sc\right)$.

In this work the use of equality between Pr and Sc number was used $Sc = \Pr = 0.7$. This assumption has been already used in jet flows [38] and gas turbine combustors [39]. This assumption also implied the unity of Lewis number. By definition, Lewis number represents the ratio of thermal diffusivity to mass diffusivity. It is defined as:

$$Le = \frac{\alpha}{D} \tag{2-17}$$

This assumption is justified in turbulent flows because turbulent diffusion exceeds molecular diffusion by order of magnitude making differential diffusion negligible. Differential diffusion becomes more pronounced when flow is laminar or has laminar regions within the turbulent flow field, and therefore has to be modelled [40].

2.4 Modelling of unresolved or Sub-Grid Scale (SGS) turbulent transport in conservation equations

The unresolved momentum fluxes can be expressed as $\left(\widetilde{u_j u_i} - \tilde{u}_j \tilde{u}_i\right)$. They can be estimated according to the Boussinesq assumption [29]:

$$\widetilde{u_j u_i} - \tilde{u}_j \tilde{u}_i = -2\nu_t \tilde{S}_{ij} \tag{2-18}$$

SGS turbulent viscosity, ν_t, has to be modelled. Most common approaches are Smagorinsky model, scale similarity, Germano dynamic model, structure function approach etc.

2.4.1 Smagorinsky model

Smagorinsky model is derived from dimensional analysis by taking cell size instead of length scale:

$$\tilde{\mu}_t = \mu_{SGS} = \bar{\rho}(C_S \Delta_x)^2 \left|\tilde{S}\right| \tag{2-19}$$

it assumes that C_S is a constant throughout the domain. For a homogeneous and isotropic turbulence it is estimated to be 0.2, while for a pipe flow it should be around 0.1 [14].

$$C_S = C_S = 0.1 \div 0.2 \tag{2-20}$$

Drawbacks of Smagorinsky approach is it's dependency on a flow configuration and value of C_S is not universal. Therefore, it can be too dissipative [41].

2.4.2 Coherent Structure Method (CSM)

In 2005, Kobayashi presented model based on coherent structure function (CSF) with a fixed model parameter [13]. The proposed approach was successfully applied to non-reactive (cold) flow cases of homogeneous turbulence and channel flows [13], turbulent channel flows with a uniform magnetic field perpendicular to insulated walls [42], magneto hydrodynamic turbulent duct flows [43], backward facing step and asymmetric plane diffuser [41] as well as supercritical flow over the cylinder [15]. SGS model based on CSF is called Coherent Structure Model (CSM). CSM model is implemented in such way that Smagorinsky closure parameter is adapted locally, according to the local coherence in the velocity field, instead of having constant value. It formulation is given in Eq. (2-21).

$$C_S \Rightarrow C_{CSM} = C_2 \left| F_{CS} \right|^{3/2} F_\Omega \tag{2-21}$$

F_Ω is the energy decay suppression function, Eq. (2-22).

$$F_\Omega = \left(1 - F_{CS}\right) \tag{2-22}$$

Coherent structure function is defined as a second invariant Q normalized by the magnitude of the velocity gradient tensor E.

$$F_{CS} = \frac{Q}{E} \tag{2-23}$$

Moreover, F_{CS} and F_Ω have definite upper and lower limits:

$$\begin{aligned} -1 \le F_{CS} \le 1 \\ 0 \le F_\Omega \le 2 \end{aligned} \tag{2-24}$$

The second invariant and magnitude of the velocity gradient tensor are given in Eq. (2-25) and (2-26)

$$Q = \frac{1}{2}\left(\tilde{W}_{ij}\tilde{W}_{ij} - \tilde{S}_{ij}\tilde{S}_{ij}\right) \tag{2-25}$$

$$E = \frac{1}{2}\left(\tilde{W}_{ij}\tilde{W}_{ij} + \tilde{S}_{ij}\tilde{S}_{ij}\right) \tag{2-26}$$

Resolved velocity strain tensor and resolved vorticity tensor are calculated according to Eq. (2-27) and (2-28).

$$\tilde{S}_{ij} = \frac{1}{2}\left(\frac{\partial \tilde{u}_j}{\partial x_i} + \frac{\partial \tilde{u}_i}{\partial x_j}\right) \tag{2-27}$$

$$W_{ij} = \frac{1}{2}\left(\frac{\partial u_j}{\partial x_i} - \frac{\partial u_i}{\partial x_j}\right) \tag{2-28}$$

Fixed model constant $C_2 = 1/22$ is derived from DNS results of homogeneous isotropic turbulence.

2.5 Hybrid LES/RANS approach

Hybrid approach assumes that turbulence framework is partly LES and partly RANS [23]. The idea behind hybrid approach is that less expensive RANS method is used in regions where LES level of detail is not required. This is, for instance, flue gas transport towards the outlet away from the combustion zone, see Figure 6.

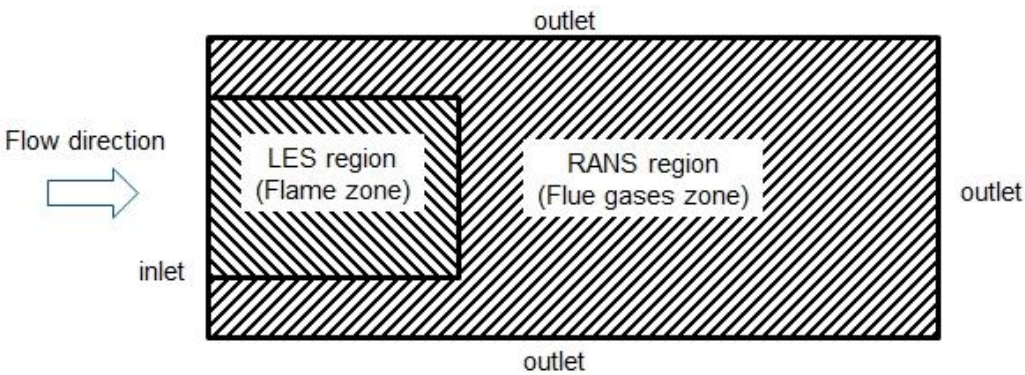

Figure 6 - Regions of LES and RANS framework in hybrid approach

RANS approach is by nature more dissipative and exhibits larger values of turbulent viscosity on the larger cells, which is desirable near outlets since reflection of pressure waves or backflow from vortices is supressed. The boundary between RANS and LES approach can be hard or soft. Soft boundaries are determined by the selected model parameter (like turbulent viscosity). Hard boundaries are determined by some 'environment parameter', like local cell size [23].

An example of soft connection between RANS and LES can be blending:

$$\mu_t^{hybrid} = f^{LES}\,\tilde{\mu}_t^{LES} + f^{RANS}\,\bar{\mu}_t^{RANS} \tag{2-29}$$

Local blending parameters f^{LES} and f^{RANS} can be determined from resolution-dependent damping of a RANS model (Flow Simulation Methodology - FSM) [44] [45], weighted sum of LES and

RANS [23], etc. On the other hand, hard connection between two frameworks has a strict boundary between the two zones and this formulation is straightforward:

$$\mu_t^{hybrid} = \begin{cases} \tilde{\mu}_t^{LES} & if \quad \Delta \le \Delta^{tresh} \\ \overline{\mu}_t^{RANS} & if \quad \Delta \ge \Delta^{tresh} \end{cases} \tag{2-30}$$

For the purpose of this work, it is important that the flame zone is entirely inside the LES region, in order to keep all combustion within the LES framework. On the other hand, it was not feasible to keep LES resolution through the whole domain. RANS region is responsible for solving transport of flue gases outside the domain, where it would be too expensive to have LES resolution of the computational grid. Boundary between the LES and RANS region is the cell size (hard boundary).

Turbulent viscosity in RANS framework can be calculated from one of the many commercially available models. In this work, *k*-*ζ*-*f* model, introduced by [46], is used. Without going into detail of the model, only the final expression for turbulent viscosity is given:

$$\overline{\mu}_t^{RANS(k-\zeta-f)} = \overline{\rho} C_\mu \zeta \frac{k^2}{\varepsilon} \tag{2-31}$$

Turbulent kinetic energy *k*, turbulent dissipation rate *ε* and velocity scale ratio *ζ* are obtained by appropriate transport equations, see [46]. This model is studied in modelling of flow and heat transfer of a wall-bounded pin matrix, where it was successfully coupled with LES [47], [48].

2.6 Species transport

Species transport is strongly coupled to the combustion modelling. In ideal case, each species would have its own transport equation, with corresponding individual reaction rate, but this approach is expensive since it needs large amount of computational resources. Due to that, in this work the simpler modelling framework is used. According to [49], species transport can be modelled if certain assumptions are taken into the account. First assumption is that unburned gas phase consists from five main species: fuel, molecular oxygen, molecular nitrogen, carbon dioxide and water (Fu, O_2, N_2, CO_2 and H_2O). The second assumption is that the fuel is fully burnt during the combustion and no fuel exist on the burned side. It should be noted that these assumptions can cause discrepancy between the simulation results and experimental data, but this is not investigated in this work.

Transport equation for each species can be written as:

$$\frac{\partial\left(\bar{\rho}\tilde{Y}_i\right)}{\partial t}+\frac{\partial}{\partial x_j}\left(\bar{\rho}\tilde{u}_j\tilde{Y}_i\right)=\frac{\partial}{\partial x_j}\left(\left(D+D_t\right)\frac{\partial\tilde{Y}_i}{\partial x_j}\right)+\omega_i \tag{2-32}$$

The burnt gas is composed of 11 species: O, O_2, N, N_2, H, H_2, CO, CO_2, H_2O, OH and NO. By taking the assumption that no fuel exists in burnt gases, the five main species (excluding fuel) of the burnt gas composition (O_2, N_2, CO_2, H_2O) are calculated according to:

$$Y_{i,b}=\frac{Y_i-\left(1-c\right)Y_{i,fr}}{c} \tag{2-33}$$

where $Y_{i,fr}$ is a fresh counterpart of the five main species (excluding fuel), calculated from the assumption of local homogeneity and isotropy, and concentrations of fresh fuel and oxygen mass fractions $Y_{i,fr}$ and $Y_{O_2,fr}$, calculated by their own separate conserved scalar equations:

Other species from the burned side have to be calculated according to some emission model. Employing emission model can alter concentrations furthermore but this is not explained here since it exceeds the scope of this work.

Combustion modelling in this work is assumed to be 2-step irreversible following chemical kinetic scheme:

$$C_nH_mO_k+\left(n+\frac{m}{4}-\frac{k}{2}\right)O_2\rightarrow nCO_2+\frac{m}{2}H_2O \tag{2-34}$$

$$C_nH_mO_k+\left(\frac{n}{2}-\frac{k}{2}\right)O_2\rightarrow nCO+\frac{m}{2}H_2 \tag{2-35}$$

Fuel reaction rates are calculated as multiplication of laminar flame speed, unburned gas density and function depending on which reaction in 2-step chemistry is active.

$$\omega_{fu,i}=\rho_{fu,fr}S_{L,0}\begin{Bmatrix}\gamma\\1-\gamma\end{Bmatrix} \tag{2-36}$$

where γ is a function depending on local equivalence ratio ϕ. Laminar flame speed S_L can be calculated either from empirical relations or can be tabulated in the form $S_{L,0}=f(\phi_{fr},p,T_u,Y_{EGR})$, see Chapter 2.7.3.3. Unburnt temperature T_u is calculated from the fresh gas composition on the unburnt side and additional conserved scalar, and the unburnt enthalpy h_{fr}.

The reaction rates for each of the main species, needed to close the equation (2-32), is calculated based on the fuel reaction rate and corresponding stoichiometric coefficients:

$$\omega_i = \upsilon_{i,1}\omega_{fu,1} + \upsilon_{i,2}\omega_{fu,2} \tag{2-37}$$

Stoichiometric coefficients are calculated from the corresponding system of equations.

2.7 Turbulent premixed combustion modelling

In turbulent premixed combustion fuel and oxidizer are mixed on molecular level and the main task of the combustion model is capturing the flame front (i.e. turbulent flame speed) which is dividing the burnt from the unburnt side. Generally, LES approach in CFD assumes that one can obtain greater level of details in results when compared with RANS approach. In this work Coherent Flame Model (CFM) is used.

The assumption in derivation of combustion models based on flamelet assumption is that the thin reaction zone is not influenced by turbulent vortices. Therefore it is important to estimate if flamelet assumption holds for specific cases presented in this work, and if not, how far combustion regime is from the flamelet region.

2.7.1 Turbulent premixed combustion regime

As the mean burning rate ω_{fu} cannot be found by simply averaging the Arrhenius law, models for turbulent combustion have to be derived [31]. Turbulent premixed combustion is characterized by interaction between various lengths, velocity and time scales describing turbulent flow field and chemical reactions. The Damkoehler number compares the turbulent and chemical time scales:

$$Da = \tau_t / \tau_c \tag{2-38}$$

In regimes with high Da number fast chemical reactions and heat release are occurring within a thin flame zone, called flamelet. Flamelet occurs when $\tau_t / \tau_c > 1$ and $\tau_\eta / \tau_c > 1$ which implies that all turbulence time scales are larger than the chemical time scale. In the flamelet regime decoupling between turbulence transport and chemistry is possible. If $\tau_t / \tau_c > 1$ and $\tau_\eta / \tau_c < 1$ the flame structure is thickened and can be quenched. This is called distributed-reaction-zone-regime [50]. In distributed-reaction-zone regime flame stretch by turbulence becomes important and local quenching of the can occur [8], [50]. Example of distributed reaction zone regime is gas turbines operating at lean mixture fraction [8]. According to [31],

chemical time scale τ_c may be estimated as the ratio of the flame thickness δ_L and the propagation speed of the laminar flame $S_{L,0}$ (time required for the flame to propagate over a distance equal to its own thickness). Turbulent time can be estimated from turbulent integral length scale characteristics, the integral length scale (l_t) and fluctuating velocity (u'). Equation (2-38) can be rewritten into:

$$Da = \frac{\tau_t}{\tau_c} = \frac{l_t}{\delta_L}\frac{S_{L,0}}{u'} \tag{2-39}$$

Turbulent integral length can be obtained from the turbulence spectra [8] from spatial or temporal longitudinal/transversal correlation, or expression $l_t = u'^3/\varepsilon$ [31]. In turbulent premixed combustion most practical situations correspond to high or medium values of *Da* number making flamelet assumption valid. Ratio between chemical and smallest turbulence (Kolmogorov) time scales is determined by Karlowitz number:

$$Ka = \frac{\tau_c}{\tau_k} = \frac{\delta_L}{l_k}\frac{u_k}{S_{L,0}} \tag{2-40}$$

Kolmogorov values can be estimated from the values of kinematic viscosity υ and local dissipation rate ε. Kolmogorov time scale is:

$$\tau_\eta = \sqrt{\frac{\upsilon}{\varepsilon}} \tag{2-41}$$

and Kolmogorov length scale is:

$$\eta = \left(\frac{\upsilon^3}{\varepsilon}\right)^{\frac{1}{4}} \tag{2-42}$$

Reynolds (*Re*), Damkoehler (*Da*) and Karlowitz (*Ka*) numbers are related as:

$$\mathrm{Re} = Da^2 Ka^2 \tag{2-43}$$

Set of only two parameters (*Re, Da*), (*Re, Ka*), (*Ka, Da*) is enough to estimate the regime for the case of premixed flame.

For easier classification of turbulent premixed flames, combustion regime diagram can be derived, Figure 7 [51]. This diagram should be used only for orientation [31].

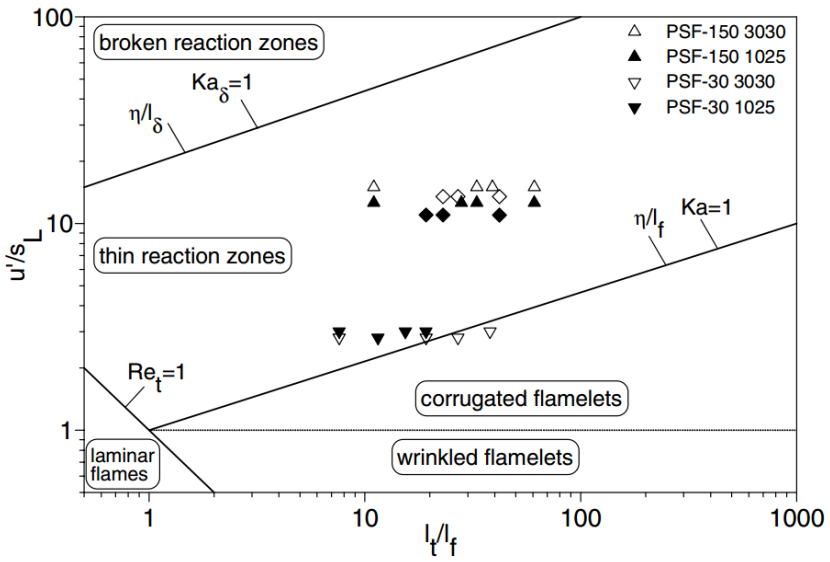

Figure 7 - Combustion regime diagram. (Source: Schneider, Dreizler and Janicka in 2005 [51])

Selecting the location for combustion diagram inputs is also relevant, since equations (2-38)-(2-43) can be defined locally everywhere inside the combustion chamber/computational domain. This means that it is not irrelevant on which locations are l_t or u' measured (experiment) or extracted (simulation). For the cases of turbulent premixed jets locations can be, for example, on the nozzle center or some other predefined position in the region of fresh mixture.

2.7.2 Flame local quenching by flame stretch

Flames can be quenched when interacting with the wall (flame-wall interaction is explained in Chapter 2.9) or due to its excessive stretch. Quench scale can be defined by setting the turnover time of a turbulent eddy equal to the flame time [52]:

$$l_q = \left(\varepsilon \tau_c^3\right)^{\frac{1}{2}} \tag{2-44}$$

When chemical time τ_c is equal to the turnover time of an eddy of the size of l_q, no complete burnout is possible during the lifetime of an eddy of size l_q [8]. This may lead to the broadening between the high and low temperature regions inside the flame front and can also lead to the pockets of unburnt mixture. Examining of the quenching is important in cases with high stretch of the flame front, since flame surface production is balanced between flame stretching and flame quenching. Small and moderate flame stretch lead to active and controllable flame while high stretch may lead to unstable flame due to quenching [53]. Flame quench scale can be

recorded locally throughout the domain and compared to local integral length scale to give a qualitative pointer towards regions where flame quenching occurs.

2.7.3 Coherent flame model in LES framework (CFMLES)

Source term for fuel mass fraction is determined from the input of the combustion model. In coherent flame model, introduced by Hawkes and Cant [1], it is assumed that turbulent reaction rate is computed as the product of the flame surface density Σ and laminar burning velocity $S_{L,0}$.

$$\omega_{fu} = \rho_u Y_{fu,fr} (S_{L,0} \tilde{\Sigma}) \tag{2-45}$$

Form of balance equation for Σ is different for RANS and LES framework. CFM in LES framework is commonly abbreviated CFMLES model [3] [18] and its detailed description is given in this work.

2.7.3.1 The concept of artificial thickening of the flame

Even though typical cell size used in LES is considerably smaller than the one used in RANS, flame front still cannot be captured accurately since the typical flame thickness is still smaller than the typical cell size in LES framework. Typical flame thickness reported in literature is around 0.1 mm, and typical CFMLES mesh resolution is around 0.5 mm. This problem is often called flame brush thickness control problem.

In order to overcome this issue, concept of artificial modification of FSD diffusion (and all other scalars) can be employed. The main principle is that diffusion coefficient in FSD transport equation is increased in order to diffuse FSD property over the few mesh cells, thus enabling that resolved structures can alter the geometry of the flame front. This means that solution of FSD field, which represents the flame geometry, depends on larger number of mesh nodes and therefore can obtain better control of the flame brush. (i.e. wrinkling from the velocity field). This diffusion has to be compensated with decrease of the FSD source terms. Generic transport equation of such approach can be written as [54]:

$$\frac{\partial(\bar{\rho}\tilde{\phi})}{\partial t} + \frac{\partial}{\partial x_j}(\bar{\rho}\tilde{u}_j\tilde{\phi}) = \frac{\partial}{\partial x_j}\left(Z\tilde{D}\frac{\partial\tilde{\phi}}{\partial x_j}\right) - \frac{\tilde{\phi}_{source}}{Z} \tag{2-46}$$

Z represents some modification factor for diffusion and source term(s).

From the premixed combustion modelling point of view, absolute criteria for correctness of such approach is that aggregate (turbulent) combustion speed is not violated. In other words,

rate at which fresh mixture is consumed should not be violated, only better tracking of the flame front fluctuating harmonics between fresh mixture and burned gases should be achieved.

CFMLES method, in the form used in this work, was first introduced by Richard et al. in 2007 [3] for investigating applicability of CFMLES in spark-ignition engine. They introduced modification of the diffusion and source terms in such a way that flame brush thickness is kept equal to $\hat{\Delta} = \Delta_x n_{filt}$, where n_{filt} is one of the model parameters with values around 5-10. Scale $\hat{\Delta}$ represents combustion filter size, which is n_{filt} times larger than the LES grid scale Δ_x. In this analysis it should be noted that combustion filter size should not be misunderstood with second-level dynamic filtering procedure, which is not used here. Figure 8 demonstrates the principle of combustion filter size.

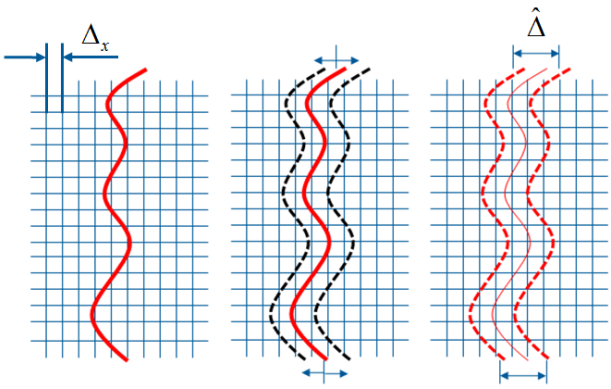

Figure 8 - Actual flame thickness over LES grid (left); artificial spreading of the flame over LES grid (middle); flame thickened over LES filter size – combustion filter (right)

Therefore, instantaneous quantities can now have three different mathematical formalisms, presented in following relations:

$\bar{\phi}$ … cell average value
$\tilde{\phi}$ … Favre filtered value
$\hat{\phi}$ … thickened filtered length scale

Introduction of combustion filter size is done since eddies smaller than the flame thickness are not able to wrinkle the flame front [54]. Flame brush thickness should be equal to combustion filter size $\hat{\Delta}$ and this is controlled by a controlling factor *F*. Controlling factor should ensure the equality [3]:

$$F\delta_{cn} = n_{res}\Delta_x = \hat{\Delta} \tag{2-47}$$

Its mathematical description is given in Appendix B. It is based on the natural flame brush thickness, grid spatial resolution and corresponding equilibrium wrinkling factor used as an estimator for SGS turbulence level inside the cell. Correction factor is plotted in Figure 9.

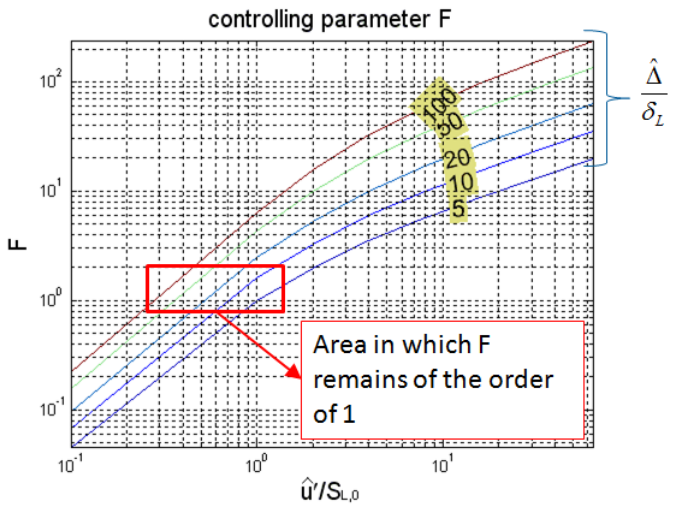

Figure 9 - Graphical representation of flame controlling parameter F (the F-diagram)

In CFMLES framework, correction factor is introduced in expression for diffusivity ($D_t \rightarrow D_t F$) and SGS strain ($str_{SGS} \rightarrow str_{SGS}/F$).

Diffusion term of all scalar equations should be filtered to combustion level only in the region of the flame. Flame region is defined as area where reaction progress variable (RPV) is between 0.001 (unburned) and 0.999 (burned). Following that reasoning, the diffusion term is is modified in the following way:

$$\tilde{D}_t(c) = \begin{Bmatrix} F(D + \hat{D}_t) & \text{for } 0.999 > c > 0.001 \text{ (flame region)} \\ D + \tilde{D}_t & \text{elsewhere} \end{Bmatrix} \tag{2-48}$$

Diffusion at combustion filter level is calculated similar as in Eq. (2-48), with exception that turbulent viscosity is filtered at combustion filter as well. It can be derived from dimensional analysis:

$$\hat{\mu}_T = \tilde{\mu}_T \left(n_{filt} \right)^{\frac{4}{3}} \tag{2-49}$$

Reaction progress variable can be obtained algebraically from the ratio between Favre filtered and initial fuel mass fraction:

$$\tilde{c} = 1 - \frac{\tilde{Y}_{fu}}{Y_{fu,initial}} \tag{2-50}$$

Initial fuel mass fraction $Y_{fu,initial}$ is tracked by the conserved scalar equation.

2.7.3.2 Balance equation for CFM in LES framework

Equation for FSD as a part of the CFMLES approach, filtered to combustion filter is derived according to [3]:

$$\begin{aligned}\frac{\partial\left(\tilde{\Sigma}\right)}{\partial t} + \frac{\partial}{\partial x_j}\left(\tilde{u}_j \tilde{\Sigma}\right) = & \underbrace{\frac{\partial}{\partial x_j}\left(\tilde{D}_\Sigma(\tilde{c})\frac{\partial \tilde{\Sigma}}{\partial x_j}\right)}_{\text{Resolved transport}} + \\ & + \underbrace{\left(\frac{\partial \tilde{u}_j}{\partial x_j} - N_i N_j : \frac{\partial \tilde{u}_i}{\partial x_j}\right)\tilde{\Sigma}}_{\text{Resolved propagation}} + \underbrace{S_d \nabla \cdot \left(N_i\right)\tilde{\Sigma}}_{\text{Resolved straining}} - \underbrace{\nabla \cdot \left(S_d N_i \tilde{\Sigma}\right)}_{\text{Resolved curvature}} + \\ & + \underbrace{a_T(\tilde{c})}_{\text{SGS straining}} + \underbrace{\beta^* S_{L,0} \frac{c^* - \bar{c}}{\bar{c}(1-\bar{c})}\left(\tilde{\Sigma} - \tilde{\Sigma}^{lam}\right)\tilde{\Sigma}}_{\text{SGS curvature}}\end{aligned} \tag{2-51}$$

Source terms appearing on the right side in FSD equation are (ordered from first to last): diffusion transport, resolved terms representing propagation, curvature and straining and sub-grid scale straining and curvature.

Displacement speed and normal to the flame front (towards fresh gases) appearing in resolved terms in FSD equation can calculated according to equations (2-52) and (2-53). Displacement speed is calculated from the conservation of mass trough the flame front:

$$S_d \bar{\rho} = S_{L,0} \rho_u \rightarrow S_d = \frac{S_{L,0}\rho_u}{\bar{\rho}} \tag{2-52}$$

Normal to the flame front is calculated as normalized gradient of RPV field:

$$N_i = -\frac{\nabla_i \tilde{c}}{\left|\nabla \tilde{c}\right|} \tag{2-53}$$

Graphical description of the flame front is given in Figure 10.

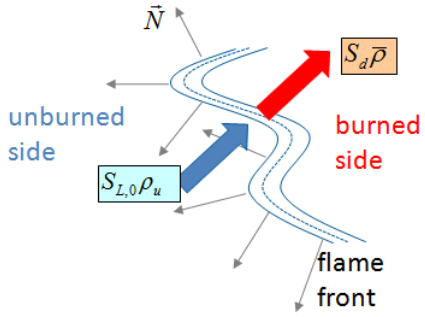

Figure 10 - Displacement speed and normal to the flame front pointing towards fresh gases.

Displacement speed is calculated from the conservation of mass passing through the unit surface of the flame and is always greater than corresponding laminar flame speed due to decrease in density behind the flame front. Vector representing normal to the plane (and pointing towards the fresh gases) can be calculated from the RPV field. The choice of laminar flame speed $S_{L,0}$ is explained in Chapter 0.

SGS straining is presented in following equation:

$$a_T = \Gamma\left(\frac{\hat{u}'_{SGS}}{S_{L,0}}, \frac{\hat{\Delta}}{\delta_L}\right)\frac{\hat{u}'_{SGS}}{\hat{\Delta}}\tilde{\Sigma} \tag{2-54}$$

Gamma function appearing in the above expression is derived in [5] and adopted for CFMLES in [3]. It represents the effective straining of the flame by turbulence at all relevant scales smaller than $\hat{\Delta}$.

Fluctuation velocity can be obtained from dimensional relations and simple Smagorinsky-like model:

$$u' = \frac{\tilde{\mu}_t}{\bar{\rho} C_s \Delta_X} = \left|\tilde{S}\right| C_s \Delta_X \tag{2-55}$$

Flame thickness is obtained from the Blint's correlation:

$$\delta_L = Bl\frac{\mu_b / \mathrm{Pr}}{\rho_{fr} S_{L,0}} \tag{2-56}$$

Blint's parameter has a value Bl=2.

Inputs for SGS curvature are laminar FSD and Bray-Moss-Libby expression [3] (Eq. (2-58))

$$\tilde{\Sigma}^{lam} = \left|\nabla\tilde{c}\right| + \left(\bar{c} - \tilde{c}\right)\nabla \cdot N_i \tag{2-57}$$

$$\bar{c} = \frac{\tilde{c}\bar{\rho}}{\left(\frac{\rho_u}{\tau+1}\right)} \tag{2-58}$$

Now, controlling parameter F can be defined. Its derivation is given in Appendix B. Here, only final equations and graphical description (Figure 9) are provided:

$$F = \frac{n_{res}\Delta_x a_T}{8K_1\sqrt{\frac{\left(D+\hat{D}_t\right)a_T}{\bar{\rho}(1-K_2)}}} \tag{2-59}$$

Model parameters K_1 and K_2 are obtained from the flow field thermal expansion rate $\tau = \rho_u / \rho_b - 1$ and model constants listed in Table 1. Their derivation is given in Appendix C and only the final relations are given here:

$$K_1 = \frac{\beta^*}{1+\tau}\left[(1+\tau)\left(\frac{1}{2}+\frac{\tau}{3}\right) - c^*\left(1+\tau+\frac{\tau^2}{2}\right)\right] \tag{2-60}$$

$$K_2 = 1 - \frac{\beta^* c^*}{1+\tau} \tag{2-61}$$

Values of all model parameters (closure coefficients) of CFMLES framework are listed in Table 1.

Table 1 - SGS model parameters and corresponding values

Variable	n_{res}	β^*	c^*
Value	5	4/3	0.5

Scalar equations for mixture fraction and unburned fuel also have to be filtered at combustion filter size [3]. This basically means that their diffusivities have to be modified according to Eq. (2-48). Final form of these scalar equations is presented:

$$\frac{\partial(\bar{\rho}f)}{\partial t}+\frac{\partial}{\partial x_j}\left(\bar{\rho}\tilde{u}_j f\right)=\frac{\partial}{\partial x_j}\left(\tilde{D}_\Sigma(\tilde{c})\frac{\partial f}{\partial x_j}\right) \tag{2-62}$$

$$\frac{\partial\left(\bar{\rho}\tilde{Y}_{fu}\right)}{\partial t}+\frac{\partial}{\partial x_j}\left(\bar{\rho}\tilde{u}_j\tilde{Y}_{fu}\right)=\frac{\partial}{\partial x_j}\left(\tilde{D}_\Sigma(\tilde{c})\frac{\partial\tilde{Y}_{fu}}{\partial x_j}\right)-\omega_{fu} \tag{2-63}$$

Rate of heat release (ROHR) is a source for energy equation and can be calculated as multiplication of fuel mass drain and its heat value:

$$\bar{\rho}\dot{q}=\underbrace{\left(\rho_{fr}Y_{fu,fr}S_{L,0}\tilde{\Sigma}\right)}_{\omega_{fu}}H_L \tag{2-64}$$

In above equation ROHR will be higher with higher value of FSD.

2.7.3.3 Laminar flame speed

Laminar flame speed $S_{L,0}$ is a model input. It can be obtained from experimental investigations [55] [56], correlation functions [57] [58] or numerical calculations performed in specific software's [59] [60] [61] [62]. Resulting values are usually tabulated in the following form:

$$S_{L,0}=f(\phi,p,T,EGR) \tag{2-65}$$

An example for methane is given in Figure 11. It can be seen that highest values of laminar flame speed is around stoichiometric equivalence ratio. Increase in pressure reduces and increase in temperature increases values of $S_{L,0}$.

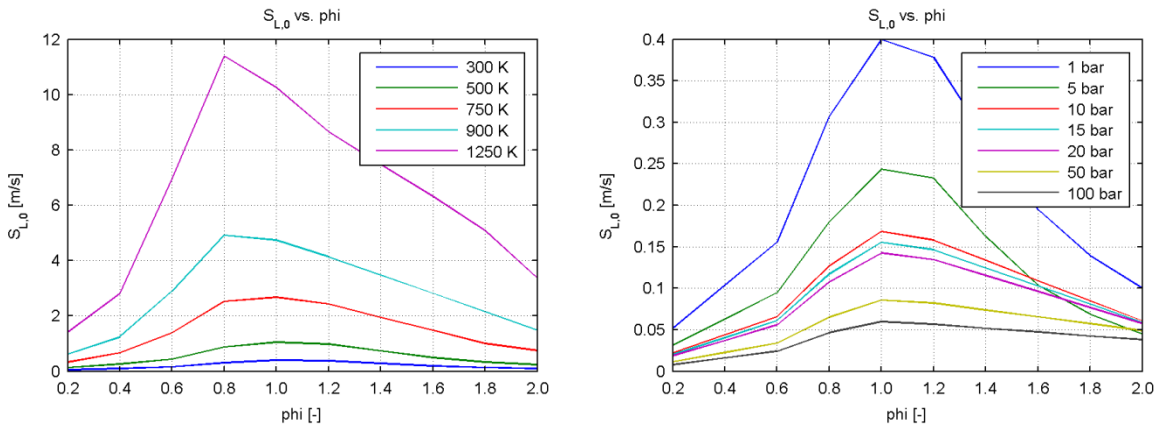

Figure 11 - Laminar flame speed obtained from GRI-MECH 3.0 mechanism [63] in PREMIX [59] solver

2.7.3.4 Ignition

Ignition procedure should basically provide the initial flame kernel. There are many ignition models, like AKTIM [3] or ISSIM [64] but in this work spherical ignition is used. Spherical ignition is simply insertion of initial FSD inside domain bounded with a sphere that represents flame kernel.

The goal of ignition in CFMLES is to provide sufficiently high values of initial FSD in order to achieve value of RPV above approximately 0.9 in at least one cell in the ignition area in a reasonable ignition time. This can lead to a very high values of initial FSD, which can retain in the domain even after the ignition has ended. Excess values of FSD are removed in first time step after the ignition by simply rearranging the FSD field in accordance with:

$$\tilde{\Sigma} = \Xi_{SGS} \left| \nabla \tilde{c} \right| \tag{2-66}$$

Sub-grid scale wrinkling factor is defined as [5]:

$$\Xi_{SGS} = \left(1 + \min\left(\frac{\Delta_x}{\delta_{L,0}}, \Gamma \frac{u'_{SGS}}{S_{L,0}} \right) \right)^{0.5} \tag{2-67}$$

Validation flames in this work are quasi-stationary and they should evolve to quasi-stationary state regardless on their ignition so no special analysis is given for ignition procedure.

2.8 Boundary conditions in LES framework

Definition of boundary conditions in DNS and LES frameworks should provide resolved turbulence at the inlets into the computational domain and prevent reflection of pressure waves on inlet/outlet boundaries.

This means that turbulent vortices should be reconstructed at the inlets, leading to correct levels of resolved turbulent vortices in front of the flame front. An alternative to the *a priori* modelling of turbulence on boundaries is to increase the computational domain further upstream so that the turbulence field can develop on its own inside the computational domain, which results in increased accuracy but larger number of computational cells and consequently longer simulation time. However, this second approach is chosen in this work, since VM requires additional its own model inputs, which might be difficult to find, especially in the case of swirling flame. Even though VM was not used in validation, it was used, in a modified form,

for definition of boundary conditions in recreating 2D vortex field for verification tests (Chapter 5).

All flow disturbances within the domain can lead to disturbances in the pressure field. This can happen during the strong sudden changes in velocity field, ignition of fresh mixture, etc. This will lead to creation of acoustic pressure waves which can have amplitudes of a few hundreds of Pascal. If these waves hit the outlet on which reflective boundaries are defined (prescribed total or static pressure or zero-gradient), they will be reflected back into the domain, like presented in Figure 14 (a). The only way they will disappear is by dissipation due to viscosity. Acoustic waves are seen in LES framework since mesh resolution is significantly smaller than wave period and time step is sufficiently small not to smooth-out acoustic waves travelling at speed of sound.

2.8.1 Vortex Method (VM) for turbulent inlet boundary conditions

In this method, turbulent structures are reconstructed from the given values of turbulent kinetic energy k and dissipation rate ε, see Figure 12.

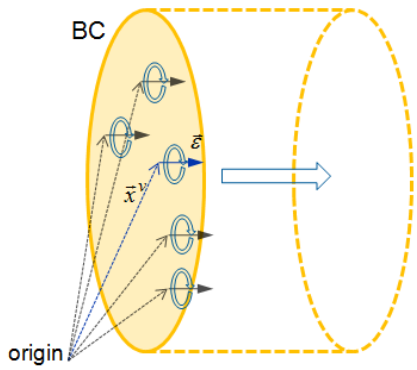

Figure 12 - Schematic representation of VM applied on inlet boundary condition. Streamwise flow is in the direction of orientation vector

The resulting turbulence, prescribed at the boundary, should retain these integral turbulent values inside the domain near the boundary. However, this artificial turbulence needs additional model input and performs worse than other alternative methods, like mapping velocity mapping for a channel flow. It was also observed that turbulence obtained form VM is decaying faster than the experimental observations, which is generally the problem with introduction of artificial turbulence. Description of the VM and its validation for a fully developed channel flow, pipe flow and separated hill flow is given in [16].

Figure 13 is showing 3D visualization of turbulence when VM is applied on a flow inside the tube.

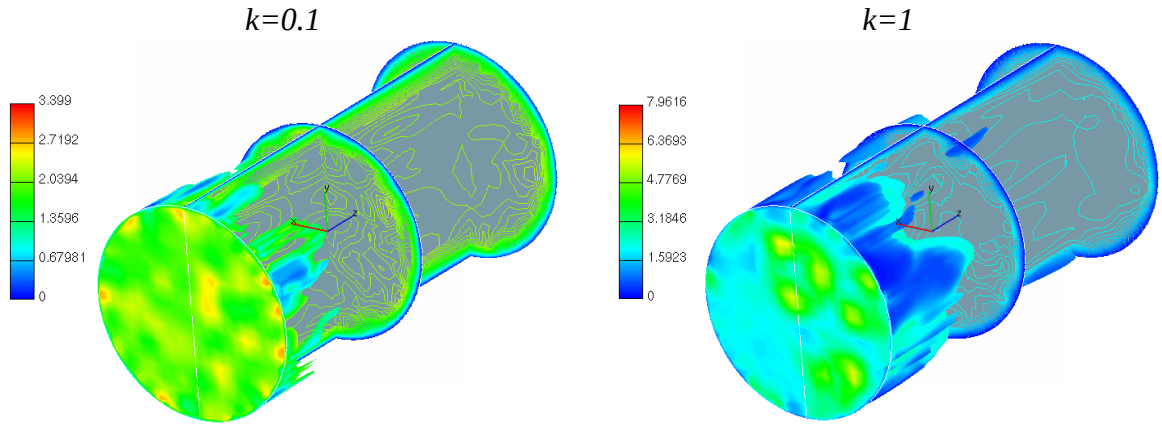

Figure 13 - 3D visualization of velocity magnitude in a few typical cross sections and iso-surface of k=0.2 for two values of *k* applied on VM. Turbulent structure size is the same in both cases

The significance of VM in this work is its application for two-dimensional cases used for estimation of discretization errors in Chapter 5. Description of a VM mathematical model, as well as its modification for two-dimensional flows is given in Appendix A.

2.8.2 Non-reflective outflow boundary conditions

In this work a full three-dimensional approach for Navier-Stokes continuous boundary conditions (3D NSCBC) approach, presented by Lodato et al. [17], is adopted. NSCBC should account for normal and transverse convection and pressure gradients on the outflow and inflow boundaries. Complete derivation of the method is explained in reference literature [17] and its implementation into CFD code is given in Appendix B. The main goal of the method is to define normal u_{1b} and transverse u_{2b} velocities, density ρ_b, pressure p_b and temperature T_b on the boundaries by using flow-field values of all variables that affect them from the inside of the domain. Formal representation of this equation set is given below:

$$
\begin{aligned}
\frac{\partial u_{1b}}{\partial t} &= f(u_{1b}, u_{2b}, \rho_b, p_b, T_b, u_1, u_2, u_{1b}^-, u_{1b}^+, u_{2b}^-, u_{2b}^+); \\
\frac{\partial u_{2b}}{\partial t} &= f(u_{1b}, u_{2b}, \rho_b, p_b, T_b, u_1, u_2, u_{1b}^-, u_{1b}^+, u_{2b}^-, u_{2b}^+); \\
\frac{\partial \rho_b}{\partial t} &= f(u_{1b}, u_{2b}, \rho_b, p_b, T_b, u_1, u_2, u_{1b}^-, u_{1b}^+, u_{2b}^-, u_{2b}^+); \\
\frac{\partial p_b}{\partial t} &= f(u_{1b}, u_{2b}, \rho_b, p_b, T_b, u_1, u_2, u_{1b}^-, u_{1b}^+, u_{2b}^-, u_{2b}^+); \\
\frac{\partial T_b}{\partial t} &= f(u_{1b}, u_{2b}, \rho_b, p_b, T_b, \underbrace{u_1, u_2, u_{1b}^-, u_{1b}^+, u_{2b}^-, u_{2b}^+}_{\text{implicitly from current time step}});
\end{aligned}
\tag{2-68}
$$

System of equations (2-68) should be solved for each time step of the calculation. It is basically set of ODE's so it can be solved with separately employed ODE solver, like DASSL [65] or DVODE [66]. Figure 14 shows the difference between the two outflow boundary conditions: the first one with prescribed static pressure and second one with 3D NSCBC employed. It can be seen that in first case there is a reflection of the pressure wave that does not appear in the second case. Reflection of the pressure wave can distort flow field inside the domain.

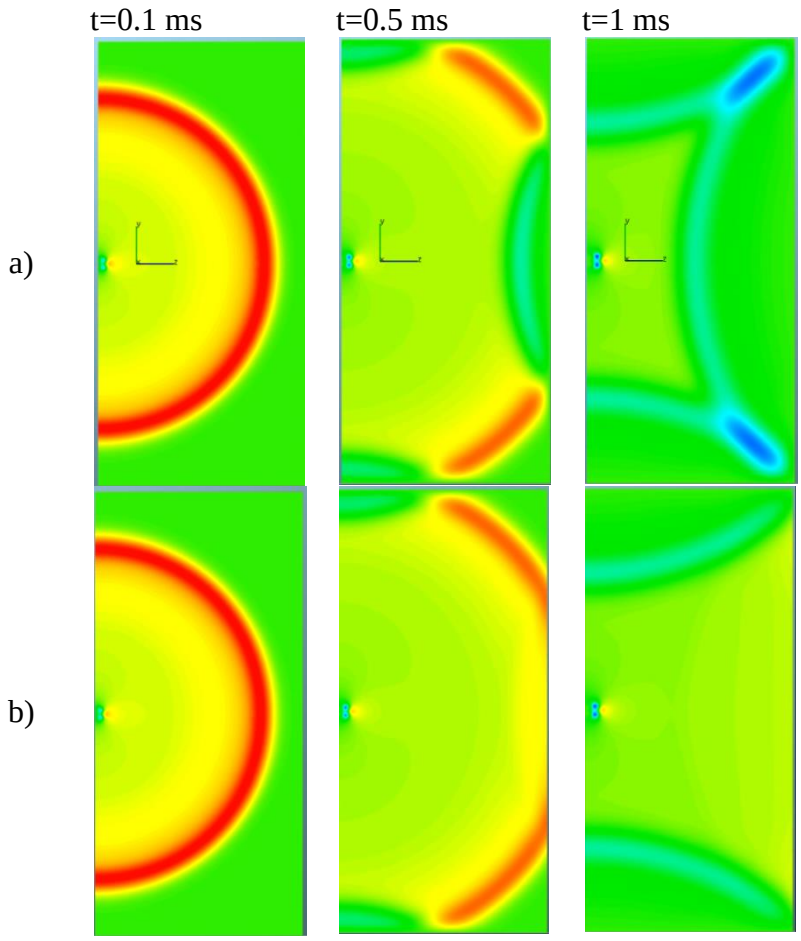

Figure 14 - Qualitative representation of static pressure outflow: (a) reflective outflow; (b) - non-reflective outflow.

2.9 Flame-wall interaction modelling

Flame-wall interaction modelling is important due to the various phenomena that have to be captured during the simulation. The most important phenomenon is the flame quenching. Flame quenches at wall due to the coupled thermo-physical processes like heat transfer, flame stretch, radical absorption and preferential diffusion [67]. During turbulent flame quenching, the combustion process stops and the reactants diffuse into the products without burning. Since there is no longer any interface separating reactants and products, any standard flamelet approach becomes invalid for capturing the flame correctly [68]. Turbulent length scales decrease near the wall and can become smaller than the flame thickness so flamelet models should not be used anymore. During the combustion burnt gases can reach temperatures between 1500 and 2500 K, while wall temperatures remain between 400 and 600 K, due to heat loss towards colder walls. Temperature decreases in a near-wall layer which is less than 1 mm thick, leading to very large temperature gradients. Quenching is directly associated to enthalpy loss from the fluid inside the domain towards the cooled wall. Another issue is the formation of unburnt hydrocarbons as a direct consequence of quenching leading to bad performance and pollution. The wall also limits flame wrinkling and acts as a sink term for the FSD [68], so the reaction rate should be lowered by modifying the original FSD through modification of laminar flame speed by enthalpy loss factor:

$$L_H = 1 - \left(Y_r + \theta\right) \tag{2-69}$$

In former expression θ is the reduced temperature (Eq. (2-70)) and Y is a reduced fuel mass fraction (Eq. (2-71)).

$$\theta = \frac{T - T^0}{T_{ad} - T^0} \tag{2-70}$$

$$Y_r = \frac{Y_F}{Y_F^0} \tag{2-71}$$

For non-isobaric combustion, enthalpy loss factor is defined as:

$$L_H = \frac{H_u^{t_0} + \int_{t_0}^{t} \left(\frac{dp}{\rho}\right) - H^t}{\Delta H} \tag{2-72}$$

Unburned reactant enthalpy is determined from the corresponding transport equation.

In an adiabatic premixed flame with unity Lewis number $L_H = 0$ everywhere and when the flame is non-adiabatic, like in near wall regions, the L_H lies between zero and one, $0 < L_H < 1$ [67]. Enthalpy loss through the wall affects the flamelet speed, flamelet annihilation and flame propagation. Reduction of laminar flamelet speed is modelled as:

$$S_{L,m} = S_L Q_m = S_L e^{-\gamma_q \beta L_H} \tag{2-73}$$

Parameter Q_m represents quenching factor, α is heat release factor, β is reduced activation energy and $\gamma_q = 25$ is a model constant. Definitions for are given in equations (2-74) and (2-75).

$$\alpha = \frac{T_{ad} - T^0}{T_{ad}} \tag{2-74}$$

$$\beta = \alpha \frac{T_{av}}{T_{ad}} \tag{2-75}$$

Adiabatic temperature T_{ad} can be estimated from the assumption of fully burnt state without heat loss from the cell, initial temperature T^0 can be obtained from conserved form of enthalpy equation and and average temperature T_{av} is provided by enthalpy equation (Eq. (2-11)).

3 Error Assesment for LES framework

In order to get objective impression on the accuracy of the simulation procedure, one has to be aware of the complete set of errors appearing and evolving during the simulation.

Accuracy can be improved by increasing the number of computational points or increasing the order of interpolation [69]. In this work both ways were limited. Increasing the number of computational points was limited due to the consequent need for higher CPU power. On the other hand, interpolation practices are as-they-are and their order of accuracy could not be modified. Therefore, this work proposes the strategy for performing LES simulations of turbulent premixed combustion under feasible possibilities at the same time keeping awareness on accuracy of the solution. In addition to commonly defined error types, like modelling, numerical and round-off errors, filtering error has to be defined as well. Additionally, since in this work implicit filtering is applied, filtering procedure is not separated from the grid and discretization errors. Based on the reasoning by Sagaut in [25], discretization error accounts for the fact that partial derivatives, which appear in mathematical model, are approximated on the

computational grid by Finite Volume (FV) scheme and resolution error accounts for the fact that some scales of the exact resolved solution are missing.

In general, it is assumed that LES simulations have small modelling errors. According to [20] conclusion about the model performance should not be drawn if calculations contain large or non-estimated errors. Modelling errors can be predicted and their estimation can be done prior to simulation. Resolution errors (both temporal and spatial) can be estimated from sensitivity analysis. Numerical errors can be traced directly during the simulation via implemented tools and tracking of residuals.

3.1 Modelling errors

Modelling errors are a consequence of various simplifications under which models were derived. Most notable model simplifications are recognized as:

- Constant value of Smagorinsky closure coefficient C_s (this is not the case for LES-CSM approach)
- Model closure coefficients for SGS FSD transport
- Unity of Lewis number
- Flame-wall interaction modelling
- Choice of Schmidt number

Smagorinsky closure coefficient should be adjusted according to the case under investigation. Since SGS dissipation is directly linked to the value of closing parameter C_s, too large value of C_s can lead to over-dissipation of the flow-field and destruction of coherent structures. Additional complexity is the implicit SGS filtering (i.e. filtering performed by the mesh), where values of C_s should be adjusted according to the local mesh refinement. Kobayashi et al. introduced local determination of C_s [14] according to the local level of coherence in the flow. The coherent structure model is inexpensive and efficient in comparison with the dynamic model, and is numerically stable without averaging.

In common types of flames, different species have different Le numbers and so a global Le number is difficult to assign [70]. Le number is associated to thermo-diffusive stability and it affects both temperature and species concentrations [71]. The flame temperature depends on the relative rate of heat and mass diffusion. If the diffusivities are equal ($Le = 1$) the total energy is conserved and the flame temperature equals to the adiabatic temperature. If $Le > 1$ the heat

loss exceeds the gain and the flame temperature is less than adiabatic. For $Le < 1$ heat loss is less than the gain in the mass and the the flame temperature is higher than the adiabatic flame [67]. Bell et al. [72] investigated Lewis number effect on lean premixed turbulent flames by performing two-dimensional calculations for hydrogen, methane and propane flame, having Le numbers 0.36, 0.96 and 1.85. They found that propane is thermo-diffusively stable since it has higher burning rates in regions with negative curvature, while unstable hydrogen flame burning is enhanced in regions with positive curvature and shows pockets of local extinction where curvature is negative. Chakraborty et al. [73] performed DNS calculations of freely propagating flame with Le number ranging from 0.34 to 1.2 and have showed Le number affects on dilatation rate. The same DNS configuration has been used by Chakraborty and Cant [70], who performed analysis on the effect of Lewis number on turbulent scalar transport. Same authors performed analysis on the effect of Le number on FSD transport [74]. The effect of non-unity and unequal Le numbers on flame dynamics was performed in [75].

Research performed in [76] showed that the choice of Prandtl/Schmidt number has significant effect on the predicted temperature field in the combustion chamber for the case of non-premixed combustion.

3.2 Discretization errors

Insufficiently fine mesh or too big time step can reduce the quality of the results. If simulation mesh is too coarse, cut-off scale is increased and less turbulence can be solved directly on the grid. This can lead to smoothening of the velocity flow field or deviation in reaction rates. Deviation of the reaction rate due to mesh resolution has to be controlled by the correction factor F, introduced in Chapter 2.7.1. According to Jasak [69], discretization errors describe the difference between the exact solution of the system of algebraic equations obtained by discretizing the governing equations on a given grid and the usually unknown exact solution of the mathematical model.

According to Meyers et al. [77] two discretization error sources are errors due to finite difference/finite volume approximation of derivatives and aliasing errors

Aliasing errors arise when non-linear terms in Navier-Stokes equations are projected on the solution space and are only relevant for high-order discretization methods. Estimation of discretization errors can be done by mesh sensitivity analysis, which is basically comparison of the simulation results between two meshes of different resolution. In this work a simple two-

dimensional test case is used for the estimation of discretization errors. As a basic error measure is the time-integrated relative deviation between LES and DNS predictions [78] [77]:

$$\delta_E(N,X)=\left[\frac{\int_0^T\left(E_{LES}(t)-E_{DNS}(t)\right)^2dt}{\int_0^T E_{DNS}^2(t)dt}\right]^{\frac{1}{2}} \tag{3-1}$$

Where N represents a measure of spatial resolution and X can represent some other comparison criteria resulting from the mathematical model (definition of Smagorinsky constant C_s) or simulation setup (e.g. time step Δt).

On the other hand, if the simulation time step is too big w.r.t. the given mesh resolution the effect can be the same as having too coarse mesh resolution. Necessary time step is estimated from the Courant number criteria.

$$C_\Delta=\Delta_x/\left(|u_i|\Delta t\right) \tag{3-2}$$

For explicit time integration courant number should be less or equal to one ($C_\Delta \leq 1$). This is also valid for implicit time stepping in order to prevent smoothing of the flow field solution evolving in time.

3.3 Numerical errors

Jasak [69] presented simple and cheap error estimation for transient calculations. Estimation can be performed with error indicators that can be defined based on the calculated resolved scalar field and geometrical properties of the mesh. For some instantaneous scalar, cell residual for a steady-state can be calculated [69]:

$$R_P(\varphi)=\sum_{f=1}^{N_f}S_f\cdot\left[\left(\rho u_i\right)_f\varphi_f-\left(\rho D_\varphi\right)_f\left(\nabla\varphi\right)_f\right]-S_uV_P-S_P\varphi_PV_P \tag{3-3}$$

The face values of φ on face and $\nabla\varphi$ can be obtained from cell-centered values φ_P [69]:

$$\varphi_f=\varphi_P+\left(\vec{x}_f-\vec{x}_P\right)\cdot\nabla\varphi_P \tag{3-4}$$

$$\left(\nabla\varphi\right)_f=\nabla\varphi_P \tag{3-5}$$

For transient cases total cell residual for some instantaneous scalar can be calculated as [69]:

$$R_F(\varphi) = \frac{\left(\rho_P^n \varphi_P^n\right) - \left(\rho_P^o \varphi_P^o\right)}{\Delta t} V_P + \frac{1}{2} R_P\left(\varphi^n\right) + \frac{1}{2} R_P\left(\varphi^o\right) \tag{3-6}$$

Error formulated in this way measures inconsistency between the prescribed variation of the function over the CV and the face interpolation practice. Set of equations (3-3)-(3-6) is calculated for each time step. It results in algebraic equation in the form:

$$R(\varphi) = a_P \varphi_P - \sum_{j=1}^{n_f} a_j \varphi_{P_j} - S_\varphi \tag{3-7}$$

Exact derivation of residual error presented in Eq. (3-7) is given in Appendix D. The numerical solution procedure of system of algebraic equations can be stopped and transferred to the next time step if certain level of accuracy is reached. This level of accuracy is usually determined a-priori for each scalar φ as the normalized sum of absolute residuals calculated by Eq. (3-7). The normalized sum of absolute residual values is defined as:

$$\frac{\sum_{i=1}^{M} \left| a_P^* \phi_P - \sum_{j=1}^{n_f} a_j \phi_{P_j} - S_\phi^* \right|}{\sum_{i=1}^{M} \left| a_P^* \phi_P \right|} \tag{3-8}$$

4 Numerical procedure

Set of equations presented in Chapter 2 are partial differential equations and their analytical solutions, in general, are not possible [62]. Therefore, they are discretized and combined into a discretized algebaric set of equations that can be solved [34].

In this work the CFD software FIRE [49] was used for the fluid flow computations. The transport equations relevant to combustion and turbulence modelling in this work were additionally implemented into the FIRE code via user-defined functions.

4.1 Integral form of the transport equations

Transport equations given in differential form in Chapter 2 have to be converted into integral form in order to be applicable to control volume (CV) method. Integration of some instantaneous quantity over the control volume V_{CV} surrounded by a surface S_{CV}, with a use of Gauss' divergence theorem [35], yields:

$$\frac{\partial}{\partial t}\int_{V_{CV}} \rho\varphi dV + \int_{S_{CV}} \rho\varphi u_j n_j dS = \int_{S_{CV}} \Gamma_\varphi \frac{d\varphi}{dx_j} n_j dS + \int_{V_{CV}} q_\varphi dV \tag{4-1}$$

The first term on l.h.s. is rate of change of the property φ in the CV. Second term is is net flux of property φ trough the CV boundaries due to the relative fluid motion to the control boundaries. The first term on the r.h.s. is due to the net diffusive flux through the CV boundaries. Last term represents the volumetric source/sink of the property φ.

4.2 Discretization into finite number of control volumes

The spatial domain is discretized into a finite number of CV's, see Figure 15. The computational nodes are located in the centres of these control volumes. In general, CV's can be polyhedrons of any type and they must not overlap. A complete set of CV's that covers a spatial domain constitutes numerical mesh.

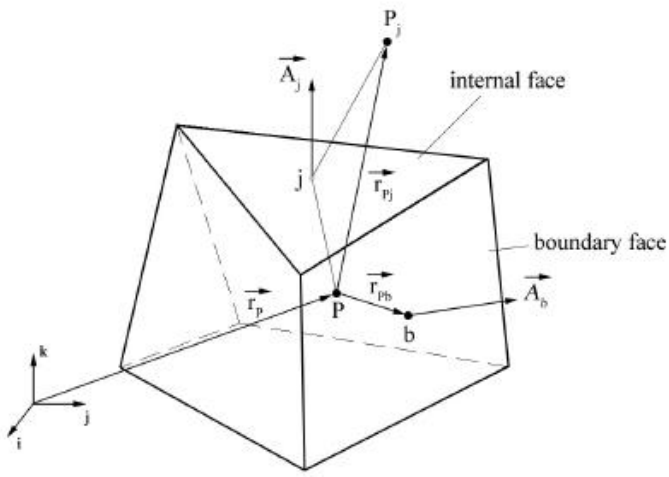

Figure 15 - Control volume (arbitrary polyhedron)

Any dependent variable is presumed to be homogeneous within the control volume and to have a value as obtained in the computational node, like collocated variable arrangement [34]. Values of dependent variables (or their gradients) on the faces are obtained by interpolation from the neighbouring computational nodes. For the approximation of the surface integrals midpoint rule is adopted [34]. Integral form of transport equation (Eq. (4-1)) can be written in algebraic form:

$$\frac{\partial}{\partial t}\left[(\rho\varphi)_c V_{CV}\right]+\sum_{k=1}^{N_f}\left(\rho\varphi u_j n_j\right)_c S_k=\sum_{k=1}^{N_f}\left(\Gamma_\varphi \frac{d\varphi}{dx_j} n_j\right)_c S_k+\left(q_\varphi\right)_c V_{CV} \tag{4-2}$$

In order to ensure the conservation of the surface fluxes it is important that the surface integrals over the common faces between the neighbouring CV's are calculated in the same way [79].

4.3 Requirements for the mesh quality

In addition to request for sufficiently high resolution, computational meshes should be structured, where possible, and without bad cells in regions where structured mesh cannot be achieved. Bad cells include negative volumes, negative normals, skewness, twisted faces etc. Detailed explanation on this matter can be found in appropriate literature [49] [80]. When simulating jet flames, the mesh structureness can usually be obtained in the region of the flame and irregular cells can occur on the joint between the fresh mixture inlet and combustion chamber, as well as regions of transition between small and large cells, near curved edges etc. This usually means that mesh should be hexahedron-dominated and mesh quality check should be performed prior to simulation setup and run.

4.4 Domain decomposition in parallel computing

Parallelization in numerical procedure consists from the decomposition of the domain into a smaller number of sub-domains and solving them separately on different CPU's. The goal of the parallelization is to reduce the computational time for the cases that have large number of mesh cells (very fine meshes or very large computational domains). The basic requirement of the domain decomposition is to get the subdomains with equal number of cells and minimum need for communication between them [49]. Both requirements reduce CPU time overhead and increases time performance of the simulation.

4.5 Numerical schemes

Calculation of the cell face values of the dependent variables includes interpolation from the values in cell centres along the direction $\vec{d}_j=\vec{r}_{P,j}-\vec{r}_P$ (Figure 15). This is called the differencing scheme. The choice of differencing scheme has high impact on results accuracy and numerical stability [34].

4.5.1 Upwind, central and blended schemes

Two academic schemes are upwind differencing scheme (UDS) and central differencing scheme (CDS).

$$\phi_j^{UDS} = \begin{cases} \phi_P \ , m_j > 0 \\ \phi_{P_j} \ , m_j < 0 \end{cases} \tag{4-3}$$

UDS is unconditionally bounded but produces excessive numerical diffusion. It is a first-order accurate in space.

$$\phi_j^{CDS} = f_j \phi_P + (1 - f_j)\phi_{P_j} \tag{4-4}$$

CDS generates numerical oscillations yielding unbounded and non-monotonic solutions. It is second-order accurate in space.

From these two we can derive blended CDS scheme with some contributions from the UDS scheme:

$$\phi_j = \phi_j^{UDS} + \gamma_\phi f_j^* \frac{m_j}{|m_j|}(\phi_{P_j} - \phi_P) \tag{4-5}$$

Second part of the above equation is the difference between the CDS and UDS, multiplied by blending factor γ_ϕ and the flow-orientated interpolation factor f_j^*.

$$f_j^* = \begin{cases} (1 - f_j), m_j > 0 \\ f_j \ , m_j < 0 \end{cases} \tag{4-6}$$

Blending factor γ_ϕ is a bounded variable between zero and one ($0 < \gamma_\phi < 1$). Blending factor is usually prescribed and user should choose it depending on the grid resolution. Generally, it is better to keep blending factor as high as possible in order to damp numerical diffusion from CDS but to still have numerical stability. Higher blending factor is usually associated to finer grids. Numerical diffusion can be controlled by setting different criteria for the computed boundedness of the numerical criteria. Two approaches, the TVD and CBC, are presented below.

4.5.2 High-order upwind schemes

High order upwind schemes have been investigated by various researchers [81] [82]. Total Variation Diminishing concept (TVD) and Convection Boundedness Criteria (CBC) can be used as boundedness criteria for construction of high order upwind bounded scheme. General upstream-weighted approximation of high-order upwind scheme:

$$\phi_j = \phi_C + \left[\frac{1}{2} f_j^*\left(1+f_j^*\right) - \alpha_j\right]\left(\phi_D - \phi_C\right) + \left[\frac{1}{2} f_j^*\left(1+f_j^*\right) + \alpha_j\right]\left(\phi_C - \phi_U\right) \tag{4-7}$$

Parameter α_j defines a family of schemes:

$$\alpha_j = \begin{cases} 0\,, \text{QUICK} \\ 0.5 f_j^*\left(1+f_j^*\right), \text{LUDS} \end{cases} \tag{4-8}$$

QUICK is third-order accurate and LUDS is second-order accurate.

Instead of using the dimensional variable ϕ it is more convenient to use normalized variable $\tilde{\phi}$, as proposed by Leonard [83]:

$$\tilde{\phi} = \frac{\phi - \phi_U}{\phi_D - \phi_U} \tag{4-9}$$

So that $\tilde{\phi}_U = 0$ and $\tilde{\phi}_D = 1$. If a limiter argument is introduced:

$$\varphi_j^* = \frac{\tilde{\phi}_C}{\left(1-\tilde{\phi}_C\right)} = \frac{\phi_C - \phi_U}{\phi_D - \phi_C} \tag{4-10}$$

Equation (4-7) can be written in a simplified form:

$$\tilde{\phi}_j = \tilde{\phi}_C + \varphi_j\left(1-\tilde{\phi}_C\right) \tag{4-11}$$

Where $\varphi_j = f\left(\varphi_j^*\right)$ and can be interpreted as a flux limiter:

$$\varphi_j = \left[\frac{1}{2} f_j^*\left(1+f_j^*\right) - \alpha_j\right]\left(\phi_D - \phi_C\right) + \left[\frac{1}{2} f_j^*\left(1+f_j^*\right) + \alpha_j\right]\varphi_j^* \tag{4-12}$$

The corresponding limiters for two bounded schemes, the MINMOD and SMART are presented below:

$$\varphi_j = \begin{cases} f_j^* \max\left\{0, \min\left(\varphi_j^*, 1\right)\right\} & \textit{MINMOD} \\ \max\left\{0, \min\left[\beta_1 \varphi_j^*, 0.5 f_j^*\left(1+f_j^*\right) + 0.5 f_j^*\left(1-f_j^*\right)\varphi_j^*, \beta_2\right]\right\} & \textit{SMART} \end{cases} \tag{4-13}$$

In this work MINMOD scheme is chosen due to good convergence properties and second-order accuracy on refined grids [49].

4.6 Solution procedure

The outcome of the discretization procedure is a set of algebraic equations in the following form:

$$a_P \varphi_P = \sum_{j=1}^{N_f} a_j \varphi_j + S_\varphi \tag{4-14}$$

For a computational domain of M control volumes a system of $M \times N$ algebraic equations need to be solved for N dependent variables φ. Equations are non-linear so iterative solution techniques are used. The segregated approach is used, which means that each equation for a specific variable φ is decoupled from the solution of other variables that are taken as known.

Throughout this work, implicit time stepping is used.

4.7 Implementation of LES boundary conditions

Boundary conditions were implemented via used-defined functions. They are called before each time step in order to set velocity and pressure field throughout the boundary. Both VM and NSCBC are calculated directly on a boundary faces by a face-loop.

4.8 Implementation of numerical error assessment tools

Implementation of numerical error assessment tools is done by calculating the error within the cells in a cell-loop manner. The residual (Eq. (3-7)) is calculated for each cell. The result is spatial distribution of residual errors. As a simulation convergence criteria the normalized sum of residuals is used (Eq. (3-8)). Normalized sum of residual can be defined and tracked for each scalar and is implemented in all CFD codes where it is used as criteria for a converged solution if it falls below prescribed value, usually few orders of magnitude below one.

5 Verification results: estimation of discretization errors

Sensitivity analysis is performed on a two-dimensional cases with fully structured rectangular grid. Although LES framework is not generally suitable for 2D simulations (except in situations with strong spanwise correlation), the choice for eliminating the third dimension was due to the need to reduce the spatial discretization step as much as possible. This greatly reduces computational time but still gives good framework for estimation of discretization errors. Sensitivity analysis is performed separately for spatial and temporal resolution.

5.1 Simulation setup

Verification simulations are performed on a two-dimensional turbulent premixed methane-air combustion cases. Fresh mixture with equivalence ratio equal to one is prescribed at the inlet. Three different meshes were used, each having different spatial resolution, see Table 2. Sensitivity of the time step is also examined, since finer mesh requires finer time step in order to preserve similar a Courant number.

Table 2 - Meshes used in estimation of discretization errors

Mesh	Number of cells (-)	Resolution (mm)	Time step (μs)
MESH100	100x100	1	20
MESH200	200x200	0.5	10
MESH400	400x400	0.25	5

Schematic representation of boundary conditions is given in Figure 16.

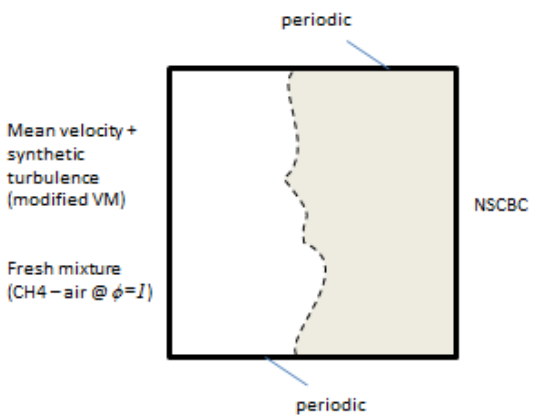

Figure 16 - Schematic view of boundary conditions used in verification tests

Inlet turbulence is synthesized by the modified Vortex Method (presented in Chapter 2.8.1). NSCBC are prescribed at the outlet and periodic boundary conditions are prescribed on top and bottom of the domain.

Relative error is calculated as integrated relative deviation between LES and very fine LES (*MESH400*), rather than DNS as presented in Eq. (3-1).

$$\delta_E(N,X)=\left[\frac{\int_0^T\left(E_{LES}(t)-E_{LES,MESH\,400}(t)\right)^2 dt}{\int_0^T E^2_{LES,MESH\,400}(t)dt}\right]^{\frac{1}{2}} \tag{5-1}$$

Integration time was $T=12\ ms$ for all cases. As second independent parameter the value of C_s is chosen. Three constant values (0.22, 0.11 and 0.55) as well as CSM approach were compared.

5.2 Estimation of spatial discretization error (mesh sensitivity analysis)

Three different mesh resolutions (MESH100, MESH200 and MESH400) were used for estimation of the influence of the spatial resolution on time-integrated deviations of ROHR and RPV. In addition, the analysis of Smagorinsky parameter ($C_s=0.22$, $C_s=0.11$, $C_s=0.055$ and $C_s=f(CSM)$) is also done. Results are presented in Figure 17.

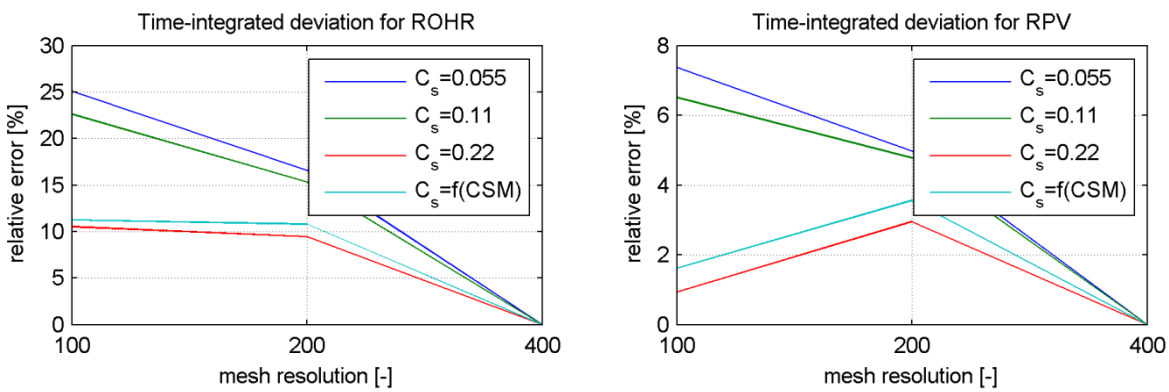

Figure 17 - Time-integrated deviation for the three mesh resolutions

Results for ROHR show that relative error between *MESH100* and *MESH400* is approximately 10% for higher values of C_s and $C_s=f(CSM)$ and 25% for lower values of C_s. Results for RPV are showing lower deviations, ranging between 6-8% for lower values of C_s and 1-2% for higher values of C_s and CSM.

Qualitative analysis of influence of the spatial resolution is depicted in Figures 18-20. Analysis of FSD field in Figure 18 and temperature field in Figure 19 shows that the flame front is

narrower as mesh resolution in increased. At the same time, it has higher peak in FSD value (1450 *1/m* for the *MESH400* and 450 *1/m* for the *MESH100*). Level of wrinkling is also higher in the *MESH400* case, since resolved eddies are appearing on a smaller cut-off scale and SGS diffusivity (according to Eq. (2-19)) is reduced, shifting the simulation framework closer to DNS.

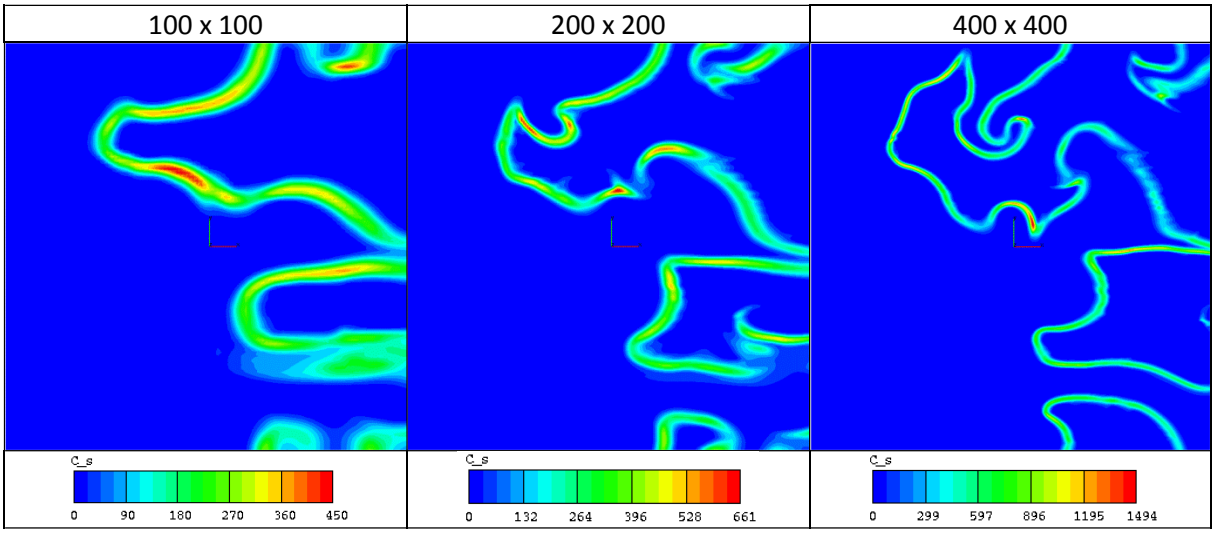

Figure 18 - Instantaneous values of FSD for the three mesh sizes

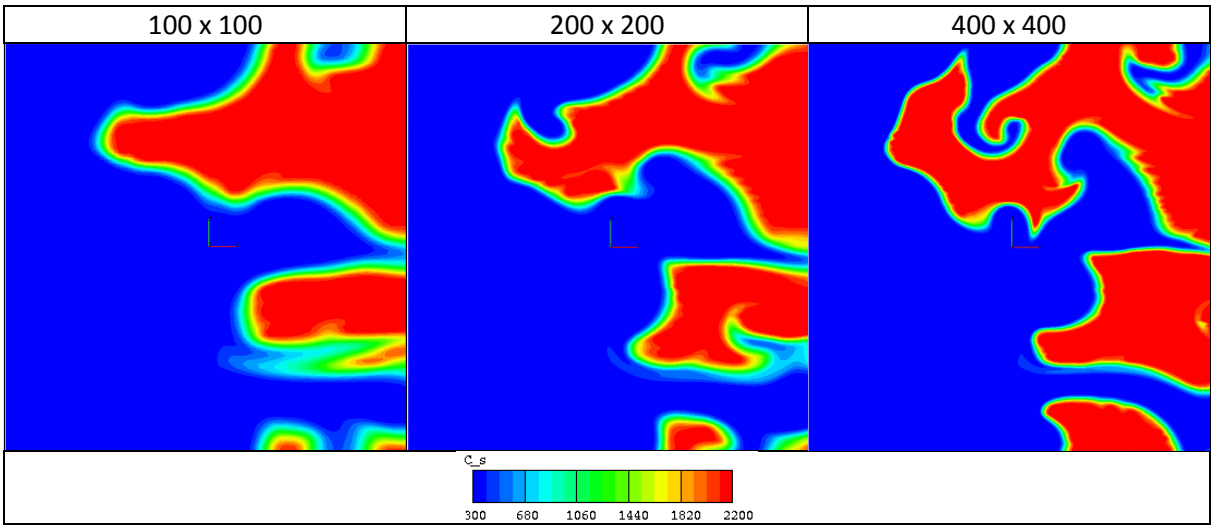

Figure 19 - Instantaneous values of temperature for the three mesh sizes

Instantaneous values of parameter C_s in the CSM SGS approach is presented in Figure 20.

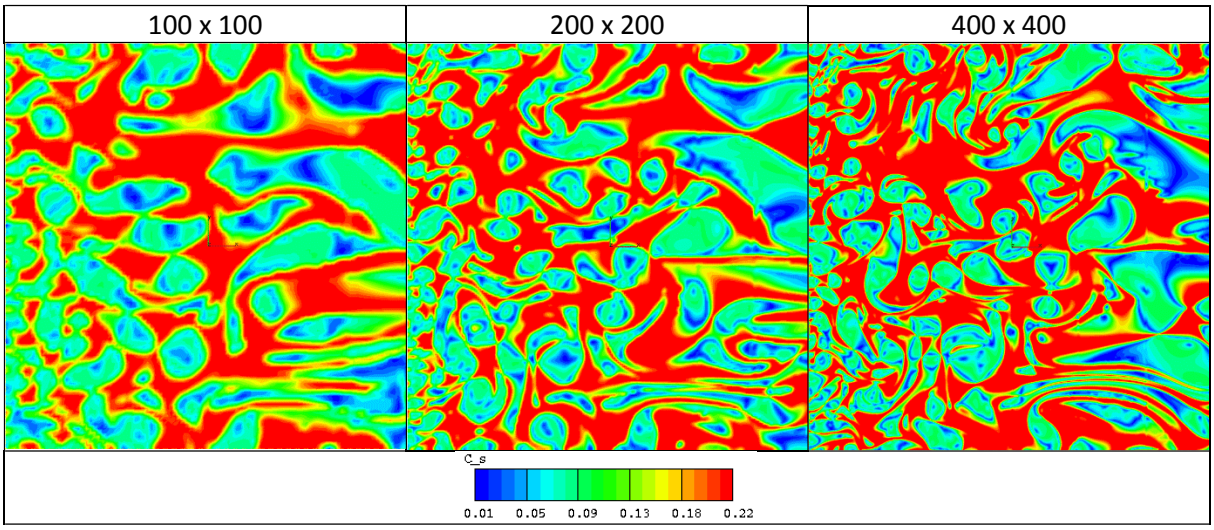

Figure 20 - Instantaneous values of C_s for the three mesh sizes

Results show that Smagorinsky parameter C_s is reduced in vortex centres and vortices are appearing further downstream in the case of more refined meshes.

5.3 Estimation of temporal discretization error (time step sensitivity analysis)

Three different time steps (200, 20 and 2 μs) were used for estimation of the influence of the temporal resolution on time-integrated deviations of ROHR and RPV. Calculations were done on *MESH100*. Results are presented in Figure 21. In addition, the analysis of Smagorinsky parameter ($C_s=0.22$, $C_s=0.11$, $C_s=0.055$ and $C_s=f(CSM)$) is also taken into account.

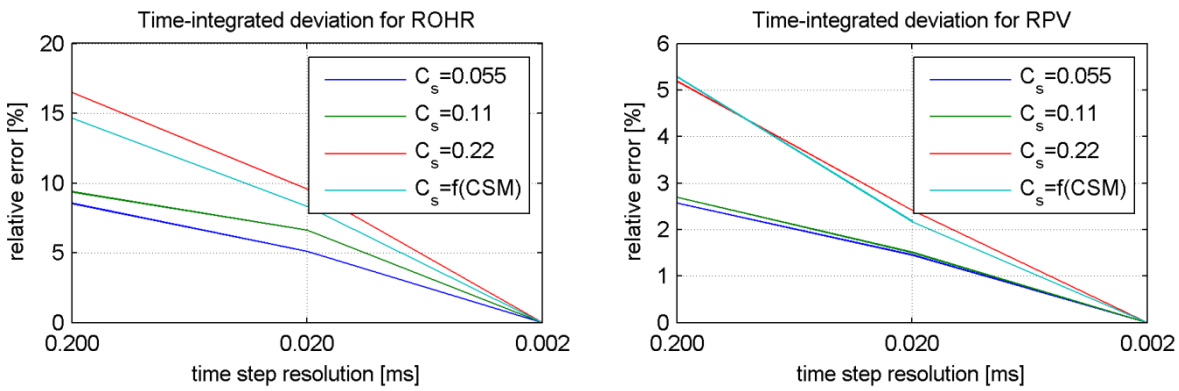

Figure 21 - Time integrated deviation for the three different time-steps

Results for ROHR show that increase in time step from 2 μs to 20 μs results in approximately 15-17% relative error for higher values of C_s and $C_s=f(CSM)$ and only 8-10% relative error for

lower values of C_s. Results for RPV are showing lower deviations from the reference case, ranging between 2-3% for lower values of C_s and 5% for higher values of C_s and $C_s=f(CSM)$.

6 Simulations of laboratory-scale flames

In this work two turbulent premixed flames were simulated and detailed analysis of simulation results is performed. These two flames are both located in the turbulent premixed regime diagram between the corrugated flamelets and the thin reaction zone regime, but have a major difference in the values of their stretch rates. Both spatial and temporal discretization of the domain was limited with the available CPU resources and the available time frame for performing the simulations of this work.

6.1 Set of results

Analysis of the results is performed by comparison of the mean and RMS quantities between simulation and experiment for three different SGS approaches, the $C_s=0.1$, $C_s=0.1$ and $C_s=f(CSM)$. After validation, qualitative analysis of local (cell-valued) flame properties is provided. Comparison between resolved and SGS source terms for FSD, influence of local vorticity and RPV on reaction rate, as well as distribution of controlling parameter F throughout the domain, is analysed. Additionally, qualitative analysis of C_s parameter is given for the case where C_s is obtained by CSM.

Flame quenching analysis is also performed by qualitative analysis of cell values of quench-to-turbulence scale ratio (δ_q/δ_t) within the flame. Ratio δ_q/δ_t is a parameter independent from two inputs for flame classification in premixed regime diagram (the δ_t/δ_F and $u'/S_{L,0}$) and it's values should be higher in highly stretched flames (quench due to flame stretch).

Error analysis is finally performed by qualitative plots of cell values of SGS vs. resolved turbulent kinetic energy with special emphasis on different SGS approaches. Plots of cell residuals are also provided and domain-integrated values of before mentioned values are listed in tables to give an estimation of numerical error and modelled (SGS) part on overall solution. Domain integrated values of SGS influence on overall solution for a scalar φ is calculated by following formula:

$$R_{\varphi}^{\%,res} = \frac{1}{V}\int_V \left[\frac{\varphi_{SGS}}{(\varphi_{res} + \varphi_{SGS})}\right] dV \tag{6-1}$$

Influence of numerical error can also be derived for any scalar φ. It is a domain-integrated average of cell residuals normalized by solution.

$$R_{\varphi} = \frac{1}{V}\int_V \left(\frac{R_{\varphi}}{\varphi}\right) dV \tag{6-2}$$

Scalars, which were tracked for error analysis, are velocity vector magnitude u and flame surface density Σ, representing scalars responsible for momentum transport and tracking of the flame.

6.2 Highly stretched premixed methane-air jet flame (flame F2)

This case represents a piloted Bunsen burner with high axial velocities of fresh mixture at the nozzle exit, described in detail in work by Chen et al. [8]. The main objective of this flame is to analyse the consequences of local quenching of reaction zones due to effect of flame stretch. From the reference literature this flame should be above the *Da=1* line in premixed combustion regime diagram. As seen in Figure 22, simulation results fall above that line. Location from which input value is extracted is at the centre of the nozzle in pure air inlet and isothermal conditions.

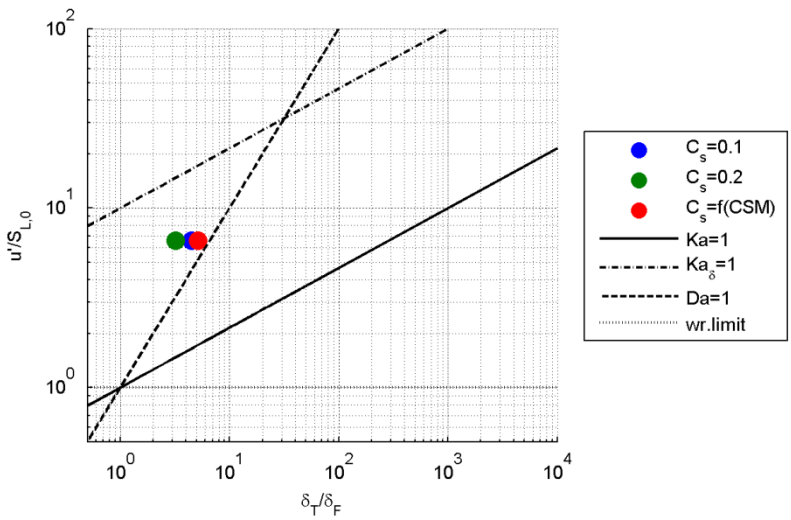

Figure 22 - Combustion regime diagram for flame F2 with plotted lines separating the regimes

In theory, these flames should cover the entire range of distributed-reaction-zones regime. The main feature of these flames is significantly lower instantaneous temperature of the flame than the adiabatic temperature within the mixing layer and fresh mixture, due to the short residence time, local flame stretch and consequent heat loss. Furthermore, partially mixing between the burned and unburnt gas (local quenching of the flame), due to high stretch rates, were observed [8].

Results of the simulation will be validated against the experimental data by radial profiles of mean velocity, RPV (defined via temperature) and main species (CH4 and CO2), as well as RMS profiles of velocity and RPV fluctuation, for five axial locations (*X/D* = 2.5, 4.5, 6.5, 8.5 and 10.5).

6.2.1 Experimental configuration

Experimental configuration is provided in Figure 23. I can be seen that the pilot surrounds the inlet of fresh mixture, which stabilizes the flame. At some downstream axial distance, the surrounding air is entrained into the flame. Fresh mixture is composed from methane and air at stoichiometric ratio ($\phi = 1$).

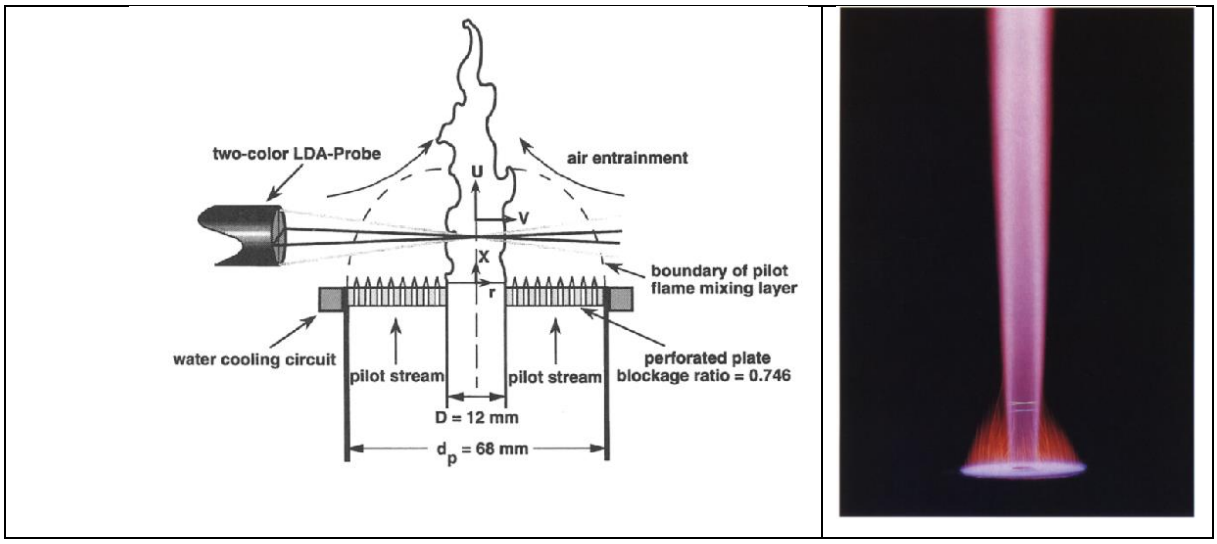

Figure 23 - Schematic view of the experimental configuration (left) and recorded average temperature field (right); (Source: Chen et al. [8])

Figure 24 presents distribution of axial components of velocity, normalized by mean velocity U_0 at the nozzle exit (x=0.5mm). Root-mean-squared streamwise/spanwise RMS fluctuations are also provided. This figure is used to validate quality of the turbulent inlet conditions for the simulation.

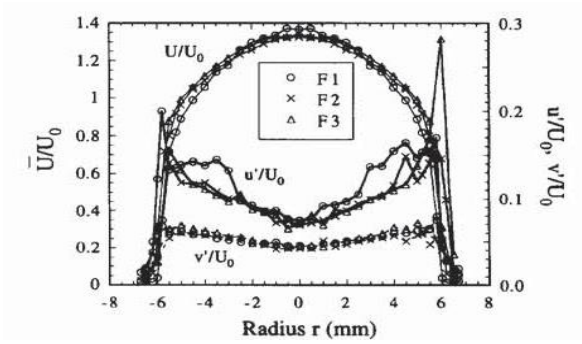

Figure 24 - Normalized mean and RMS velocity profiles at burner exit plane. (Source: Chen et al. [8])

Values presented in the former figure were recorded at isothermal conditions, so validation of the boundary conditions was performed first by simulating the isothermal flow.

Experimental analysis was performed for three different axial velocities at the nozzle exit which defines three flames: F1 with 65 m/s, F2 with 50 m/s and F3 with 30 m/s. Flame inlet parameters are presented in Table 3.

Table 3 - Parameters for three different premixed highly stretched flames.

Variable	Flame configuration		
name	F1	F2	F3
U_0	65	50	30
ϕ	1.0	1.0	1.0

In this work simulation of flame F2 is done. Time step was *5μs* and convergence criteria was *1e-4* for momentum, energy and all scalars.

6.2.2 Simulation set-up

Computational domain following geometry from schematic view in Figure 23 is discretized into the computational mesh consisting from hexahedron cells, especially in the combustion region. Computational mesh has approx. 1.2 million cells and typical cell size is between 1-1.5 mm inside the flame region.

Cross-view of the mesh	Schematic view of the inlet BC's
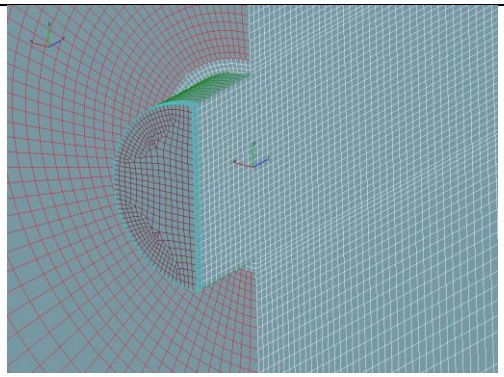	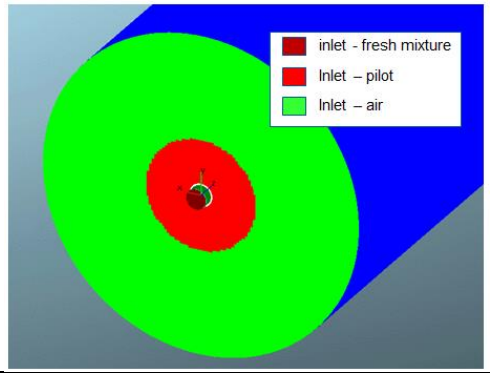

Figure 25 - Mesh and inlet configuration for Chen case.

Boundary conditions and mesh are presented in Figure 25. Three inlet boundary conditions were employed: fresh mixture, pilot and air. Inlet parameters are presented in Table 4.

Table 4 - parameters for inlet boundary conditions for flame F2

Selection	T [K]	U [m/s]	ϕ
fresh mixture	273	from mapping	1.0
pilot	1660	1.5	1.0 (egr[1] 1.0)
air	300	1.5	0.0

Outlet conditions were slipwall in lateral direction and NSCBC in axial direction.

6.2.3 Isothermal flow - validation of boundary conditions

Simulations of isothermal flow were used for validation of mean and RMS values of streamwise and spanwise components of velocity w.r.t. the values measured in the experiment under isothermal conditions. The importance of this simulation test is to see if velocity and turbulence taken from the channel can serve as boundary condition for the burner. According to the reference literature, the inlet into the combustion chamber should represent fully developed turbulent flow inside the round pipe. Fully turbulent conditions inside the tube can be obtained by the mapping procedure. The configuration of mapping procedure is presented in Figure 26.

[1] egr - exhaust gas recirculation

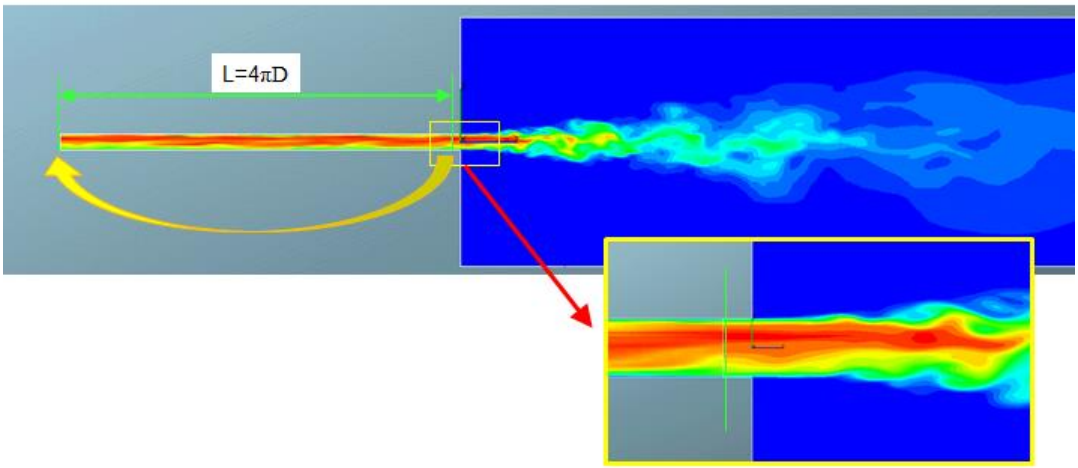

Figure 26 - Computational domain representing channel attached to the burner. Channel is used to generate velocity and turbulence field for the burner zone.

Length of the channel prior to combustion chamber should be sufficiently long not to distort evolution of turbulence but not too long since it increases computational time. Length $L = 4\pi D$ is chosen as most appropriate.

Results of the isothermal flow for are presented in Figure 27 and Figure 28. Results in Figure 27 indicate that mean values of axial velocity were well reproduced, while RMS values of radial velocity were not matched. Also, axial RMS fluctuations of axial velocity were well matched as seen on Figure 28.

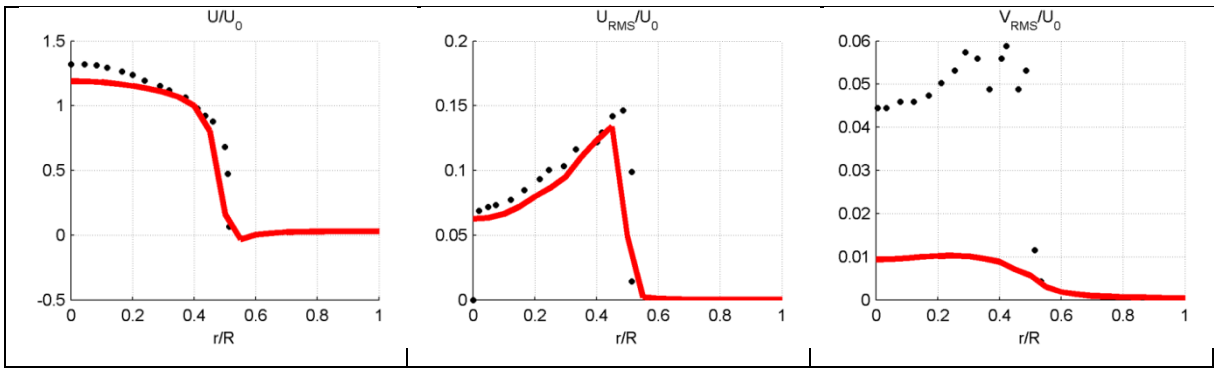

Figure 27 - Flame F2: Mean and RMS values of axial (U) and tangential (W) velocity on three axial positions near the nozzle exit (1, 10 & 20 mm) for isothermal flow

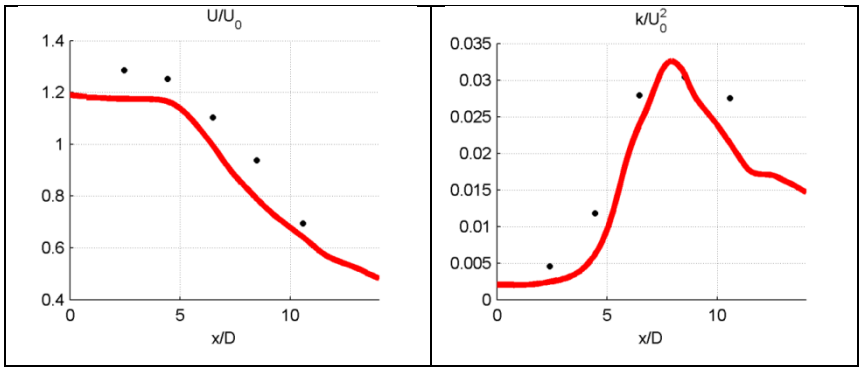

Figure 28 - Flame F2: Axial distribution of axial velocity and turbulent kinetic energy, normalized by mean axial velocity for isothermal flow

Cold flow validation shows that discrepancy of the simulation results from the measured data were less than 10%.

6.2.4 Reactive flow

Mean and RMS temperature and velocity radial profiles are presented in the same way as they were presented in reference literature. Temperature profile is presented trough temperature-based RPV:

$$C = \frac{T - T_u}{T_b - T_u} \tag{6-3}$$

It's mean and RMS formulations are defined in the following way:

$$\overline{C} = \frac{\overline{T} - T_u}{T_b - T_u} \tag{6-4}$$

$$\overline{C'} = \frac{\sqrt{\overline{T'^2}}}{T_b - T_u} \tag{6-5}$$

Velocity profile is also normalized with value $U_0 = 50\,\mathrm{m/s}$, while RMS values were normalized with $k_0 = 3.75\,\mathrm{m^2/s^2}$.

Results were averaged over the time period of 60 ms.

Qualitative difference between three approaches for flame F2 is depicted in Figure 29. Figure 29 shows similar wrinkling levels for the cases C_s = 0.1 and C_s= 0.2, while for the case C_s=f (CSM) more wrinkling inside the flame zone can be seen. The differences between three approaches can be explained by the fact that CSM approach allows the C_s to locally go towards

very low values, thus eliminating excessive SGS viscosity which might dissipate the flow field vorticity.

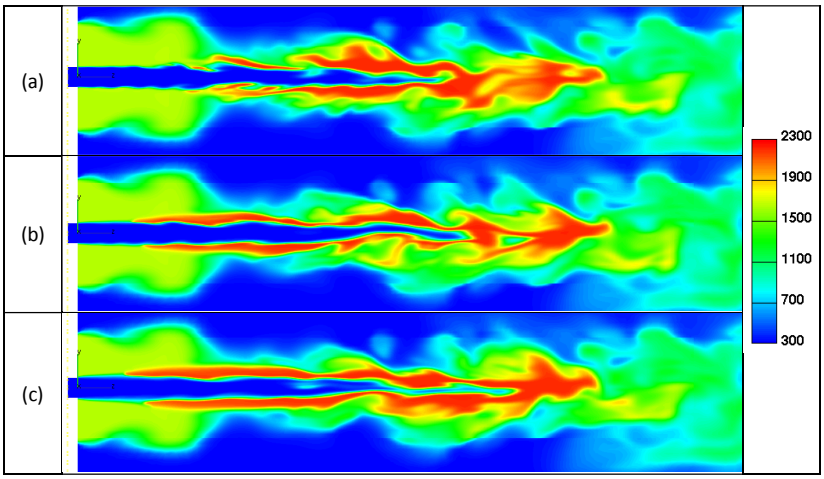

Figure 29 - Flame F2: Comparison of instantaneous temperature field; C_s=f(CSM) (a); C_s=0.1 (b) and C_s=0.2 (c)

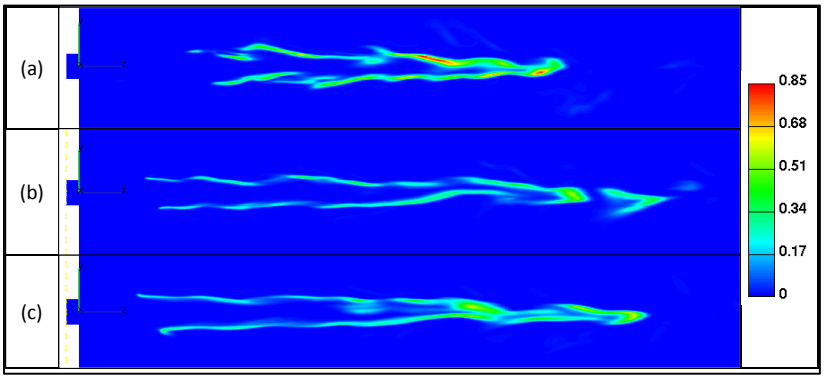

Figure 30 - Flame F2: Comparison of instantaneous reaction rate field; C_s=f(CSM) (a); C_s=0.1 (b) and C_s=0.2 (c).

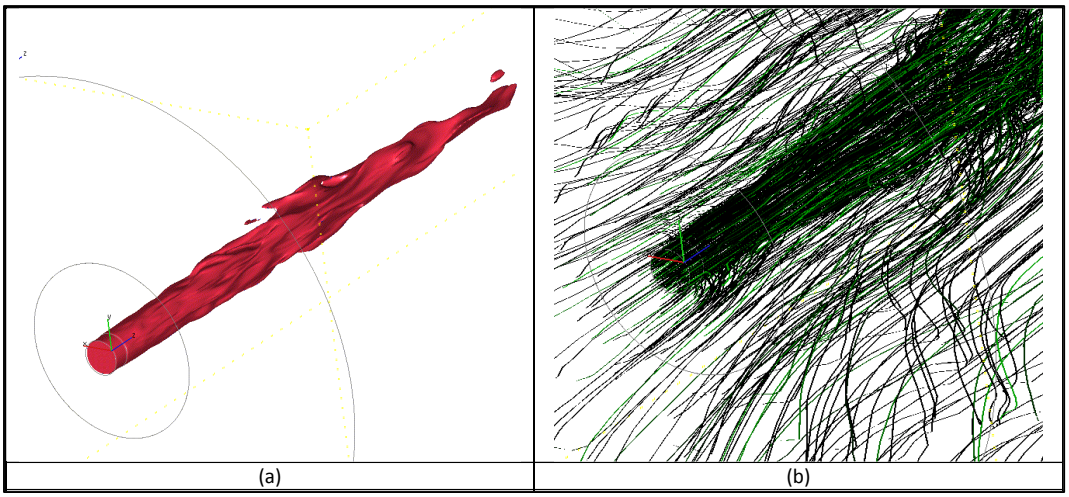

Figure 31 - Flame F2: Iso-surface of instantaneous reaction rate (left) and streamlines at nozzle entrance to the combustion chamber (right)

Results presented in following figures indicates that the choice of Smagorinsky constant C_s has high influence on flow field, temperature profiles and mean species.

6.2.4.1 Validation of mean and RMS quantities vs. experimental data

Radial profiles of the reaction progress variable from Figure 32 indicate that reaction rate is too excessive in the area closer to the center. This is especially seen at lower axial positions, near the nozzle. As already mentioned, this might be the reason for mismatch between experimental and simulated profiles of axial velocity and RPV. Radial profiles of RPV fluctuations (C_p) are also inclined towards the center which is probably also a consequence of higher reaction rate towards the central zones. However, magnitudes of the fluctuations were matched well, with observation that CSM approach reproduces more fluctuations than other two approaches.

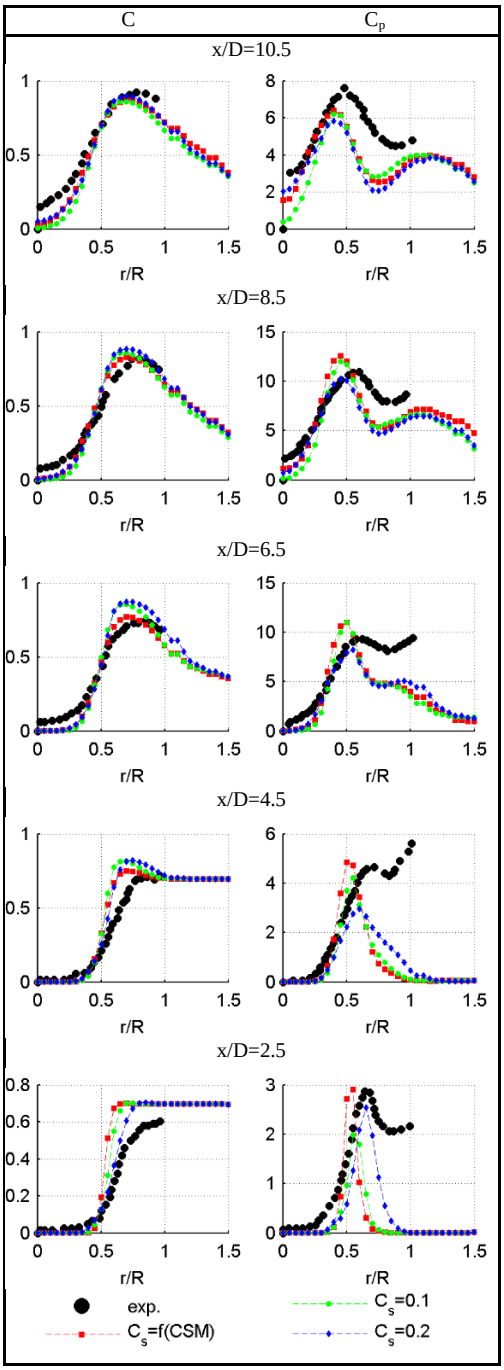

Figure 32 - Flame F2: mean and RMS of reaction progress variable.

Radial profiles of mean values of main species, the CH4 and CO2, are presented in Figure 33 It can be seen that CH4 values are over predicted in all axial positions, while CO2 is under predicted, except in axial position close to the nozzle. Difference between three approaches is not visible from radial profiles of main species. This means that the combustion is delayed in all approaches, despite the fact that RPV calculated from the temperature field is over predicted. The reason for such behaviour may be the use of very simple chemistry model or incorrect

definition of boundary conditions. Since objective of this work is to investigate difference between three approaches for C_s and possible benefits from using CSM approach, this will not be further analysed.

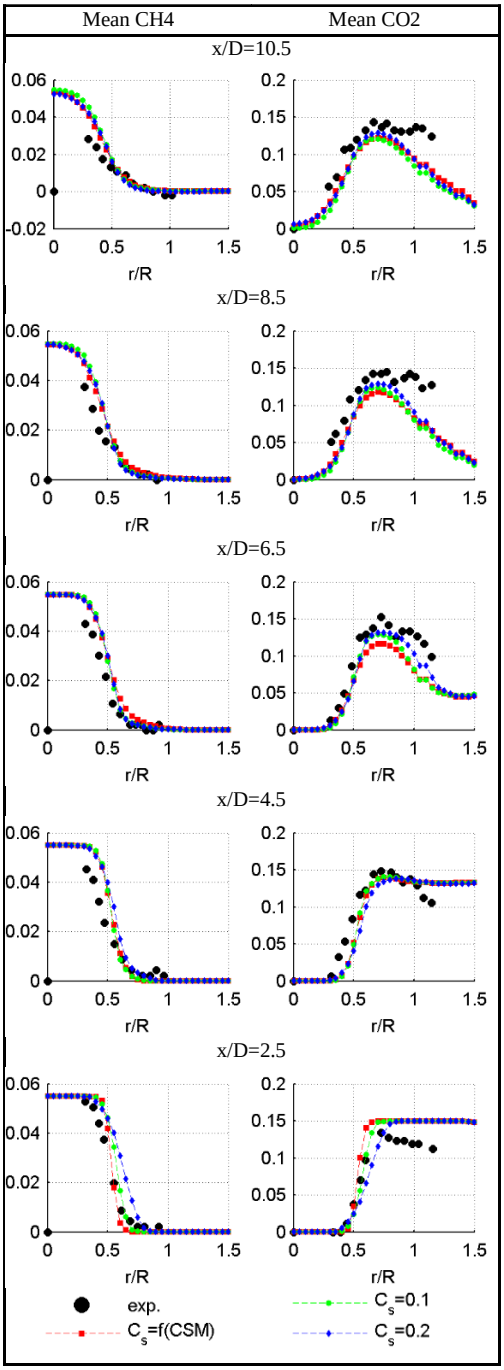

Figure 33 - Flame F2: mean CH4 and CO2 species.

The mean axial velocity from Figure 34 indicates that the mean axial velocity is lower than the experimental values on the outer radius of the flame. This might be a consequence of too

excessive reaction rate resulting in over prediction of the temperature field, as seen in Figure 32, or incorrectly resolved boundary conditions. All three approaches for C_s are showing this trend. Radial profiles of turbulent kinetic energy indicates that the best approach for solving fluctuations is CSM approach, probably due to the fact that locally reduced values of C_s enables lower dissipation of the vorticity field.

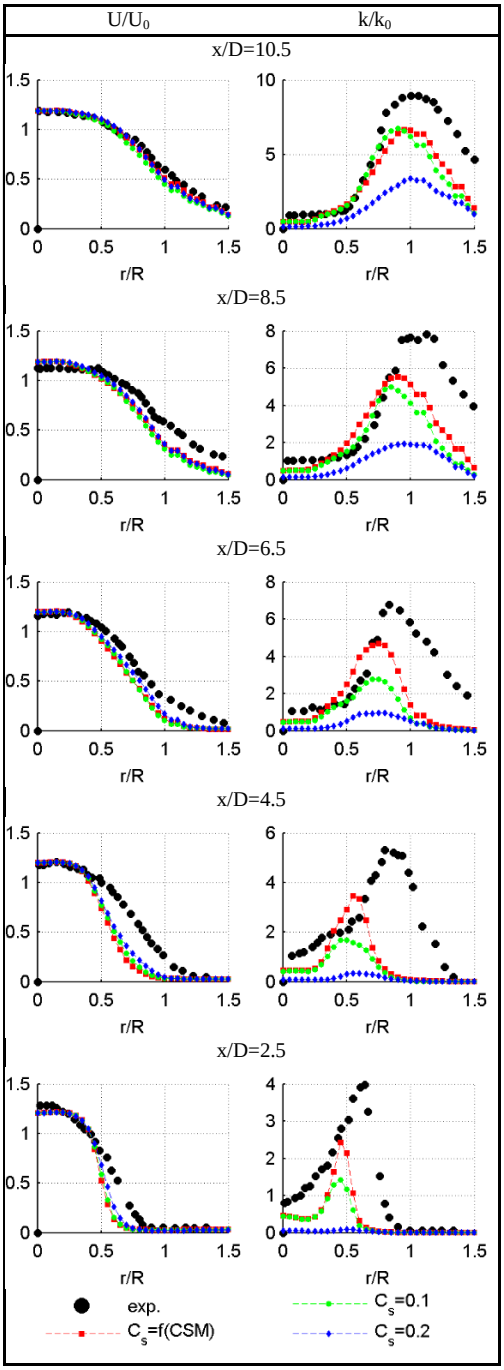

Figure 34 - Flame F2: mean and RMS velocity field. RMS velocity field represents resolved turbulence.

6.2.4.2 Influence of different SGS models on flame properties

Influence of different SGS models is clearly visible in different distribution of model quantities. These are the ratio between SGS and resolved FSD source terms, the distribution of RR and controlling parameter F across the flame front or the local levels of vorticity.

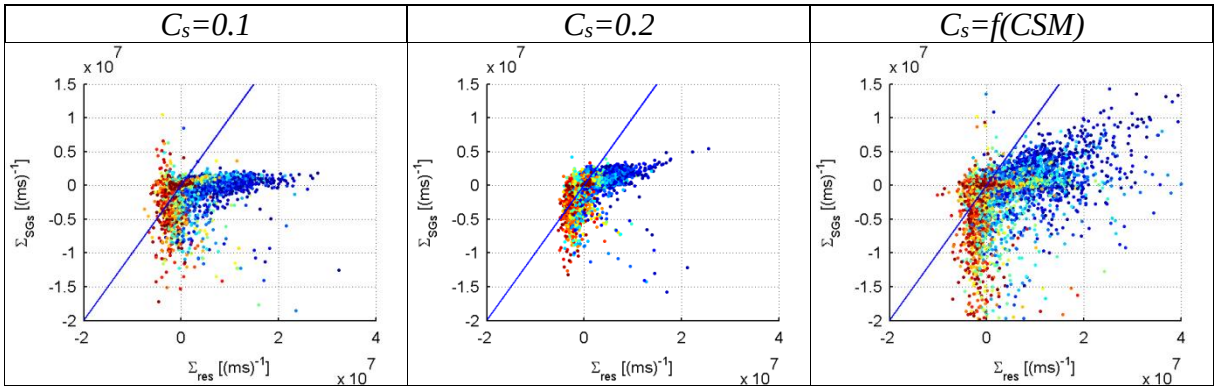

Figure 35 - Flame F2: scatter plots of cell values for resolved vs. SGS FSD source terms, coloured by RR for C_s=0.1, C_s=0.2 & C_s=f(CSM)

Ratio between SGS and resolved FSD source terms (Figure 35) shows that distribution is more compact in the case with higher C_s. It is also noticeable that CSM approach has largest scattering from the center point (0,0). This might be explained by the fact that local values of C_s fall close to zero in regions with high vorticity (Figure 40) thus eliminating turbulent SGS viscosity which leads to less compact distribution of SGS-to-resolved ratio around the center point.

Distribution of reaction rate across the flame, presented in Figure 36, is showing that for all three approaches largest reaction rate is at the middle of the flame, and this is less pronounced in the CSM approach. Furthermore, significant amount of vorticity is present throughout the flame, indicating that the laminarization did not occur after heat release indicating the wrinkling of the partially burned fuel and flame quenching. Distribution is more scattered in the case where C_s=f(CSM) than in the case with constant values of C_s.

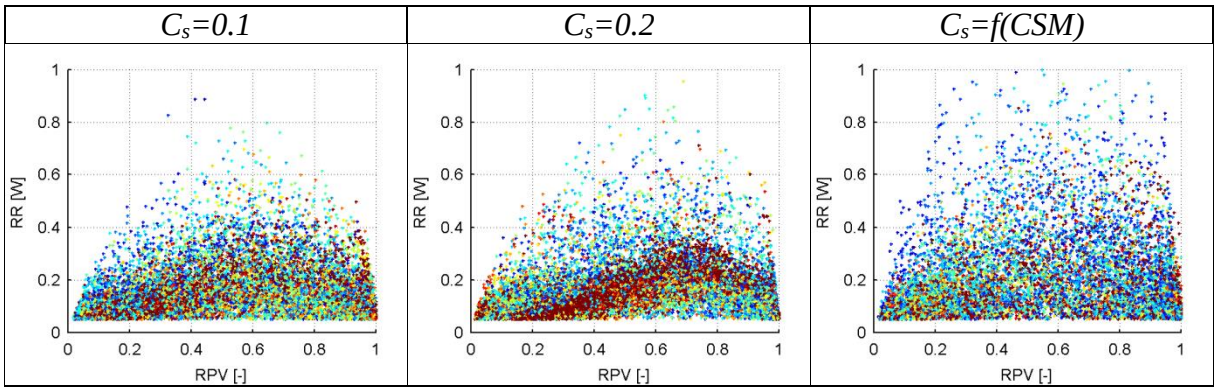

Figure 36 - Flame F2: scatter plots of cell values for RR vs. RPV, coloured by vorticity, for $C_s=0.1$, $C_s=0.2$ & $C_s=f(CSM)$

Values of controlling parameter F are dropping throughout the flame (Figure 37). Distribution is more scattered in the case where $C_s=f(CSM)$ than in the case with constant values of C_s. Highest levels of reaction rate occurs at the controlling parameter values between 0.2 and 0.4.

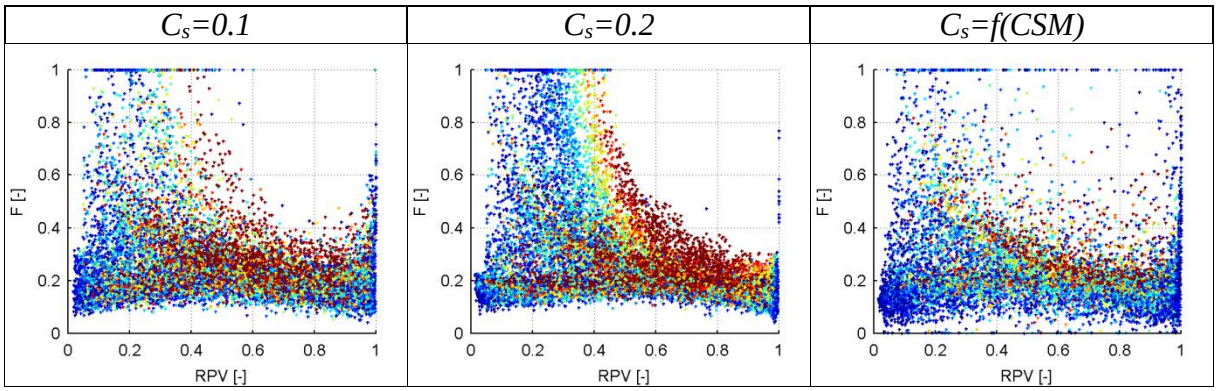

Figure 37 - Flame F2: scatter plots of cell values for controlling factor F vs. RPV, coloured by RR for $C_s=0.1$, $C_s=0.2$ & $C_s=f(CSM)$

Values of controlling parameter are plotted directly in the F-diagram (F-diagram is presented in Chapter 2.7.3.2) in Figure 38. Difference between the three SGS approaches is clearly seen. For the same level of turbulence inside the cell the $C_s=0.1$ approach gives values of F closer to one, leading to the conclusion that the flame is less controlled if the local values of C_s are lower. This conclusion is in accordance with Eq. (2-59) for F, where SGS diffusion (which is directly proportional to C_s) appears in the denominator.

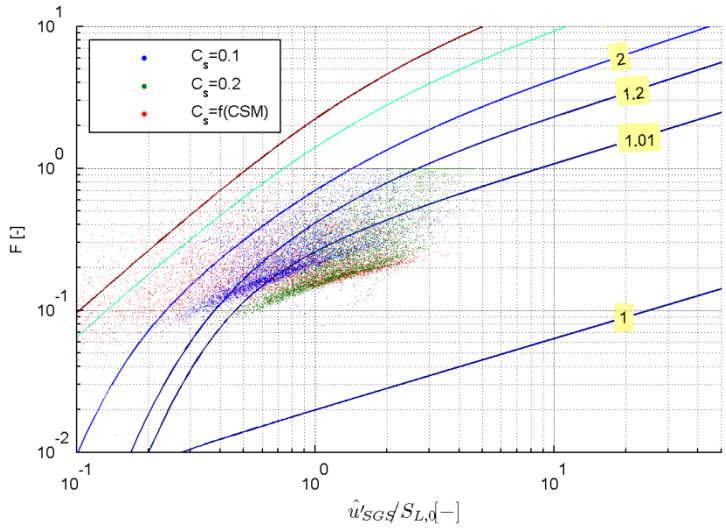

Figure 38 - Flame F2: cell values of controlling factor F for $C_s=0.1$, $C_s=0.2$ & $C_s=f(CSM)$; lines are different parameters of $\hat{\Delta}/\Delta_x$

6.2.4.3 Flame quenching

This flame is characterized by high stretch rate, so ratio between quench and turbulent scale is locally close to or larger than unity. Cell values of δ_q/δ_t are plotted against RPV for three different SGS approaches are plotted in Figure 39.

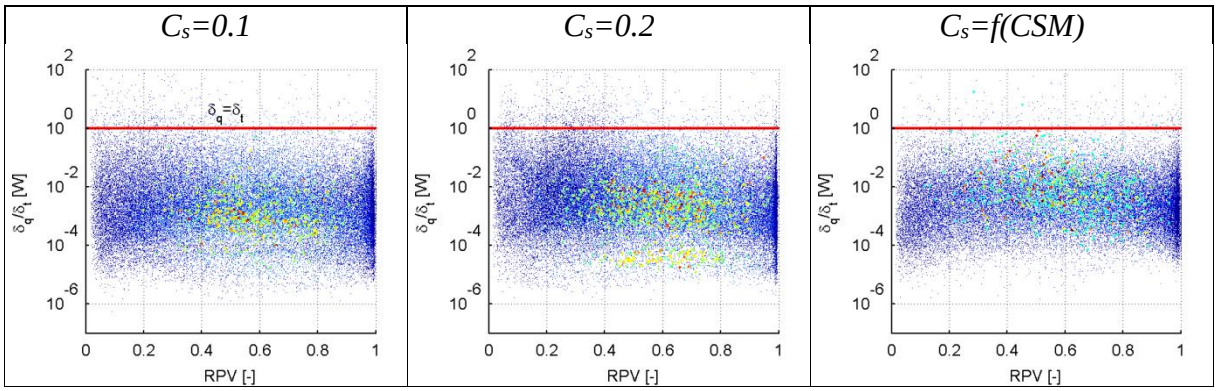

Figure 39 - Flame F2: scatter plots of cell values for δ_q/δ_t ratio vs. RPV, coloured by RR; horizontal line represents limit where $\delta_q/\delta_t = 1$ (above that limit flame quenching can be expected)

It is clearly visible that flame quenching may occur locally inside the flame, especially on the first half of the flame (first half of RPV range). This is best seen in case $C_s=0.2$. Majority of the RR occurs in regions where δ_q/δ_t ratio is below 1%.

6.2.4.4 Parameter C_s

Decreasing of C_s with increasing vorticity is clearly seen in Figure 40. This was expected since vorticity is actually coherence in velocity field, which acts as sink in energy decay suppression function (Eq. (2-22)).

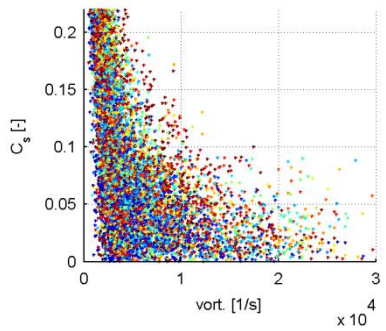

Figure 40 - Flame F2: scatter plot of cell values for Smagorinsky parameter C_S vs. vorticity for $C_s=f(CSM)$, coloured by RPV

Cell values of significant reaction rate are distributed across the whole values of vorticity and corresponding C_s, which was also observed in previous analysis.

6.2.4.5 Error analysis

One of the most widely used indicators if LES conditions were achieved in is the ratio between the resolved and SGS turbulent kinetic energy. The rule of thumb for cold-flow simulations is that the overall LES solution should be approximately 80% directly resolved on the mesh [29]. Scatter plots for three SGS approaches are presented in Figure 41. Plots basically confirm that using higher values of C_s leads to more pronounced values of SGS kinetic energy, since these variables are mutually proportional. CSM approach results in very scattered ratio, which is a trend already seen in previous flame analysis.

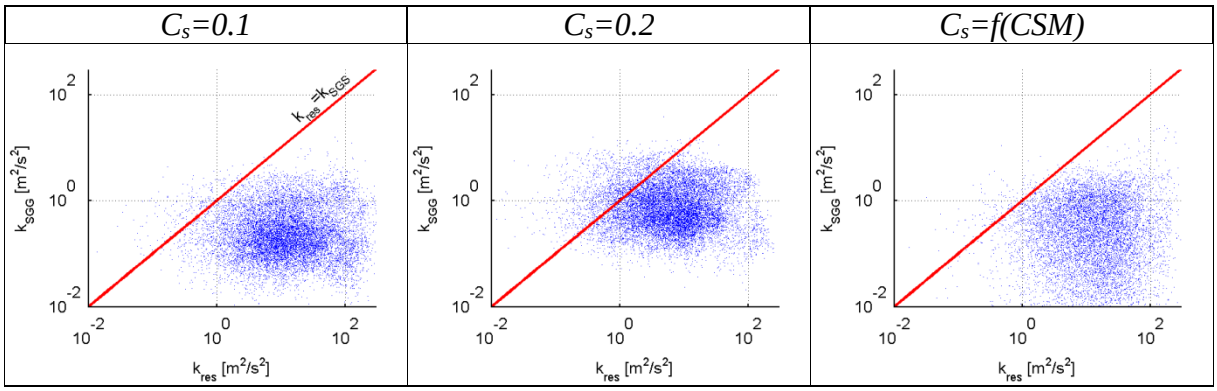

Figure 41 - Flame F2: scatter plots of cell values for resolved vs. SGS turbulent kinetic energy for $C_s=0.1$, $C_s=0.2$ & $C_s=f(CSM)$; line represents equality between resolved and SGS TKE

Further analysis looks at the ratio between cell values of residuals vs. nominal solution, as well as normalized cell residuals of the FSD vs. normalized residuals of the momentum, both presented in Figure 42. First set of plots provide information on residual evolvement throughout the flame (flame position is identified by level of RPV). Residuals are gradually increasing with the increasing RPV. Nevertheless, residuals generally stay less or around the value of 1%.

Analysis of normalized residuals indicates that normalized residuals for FSD are 10 times higher than residuals for momentum. Following the logic from the analysis of the FSD residual, this difference is more pronounced towards the higher values or RPV.

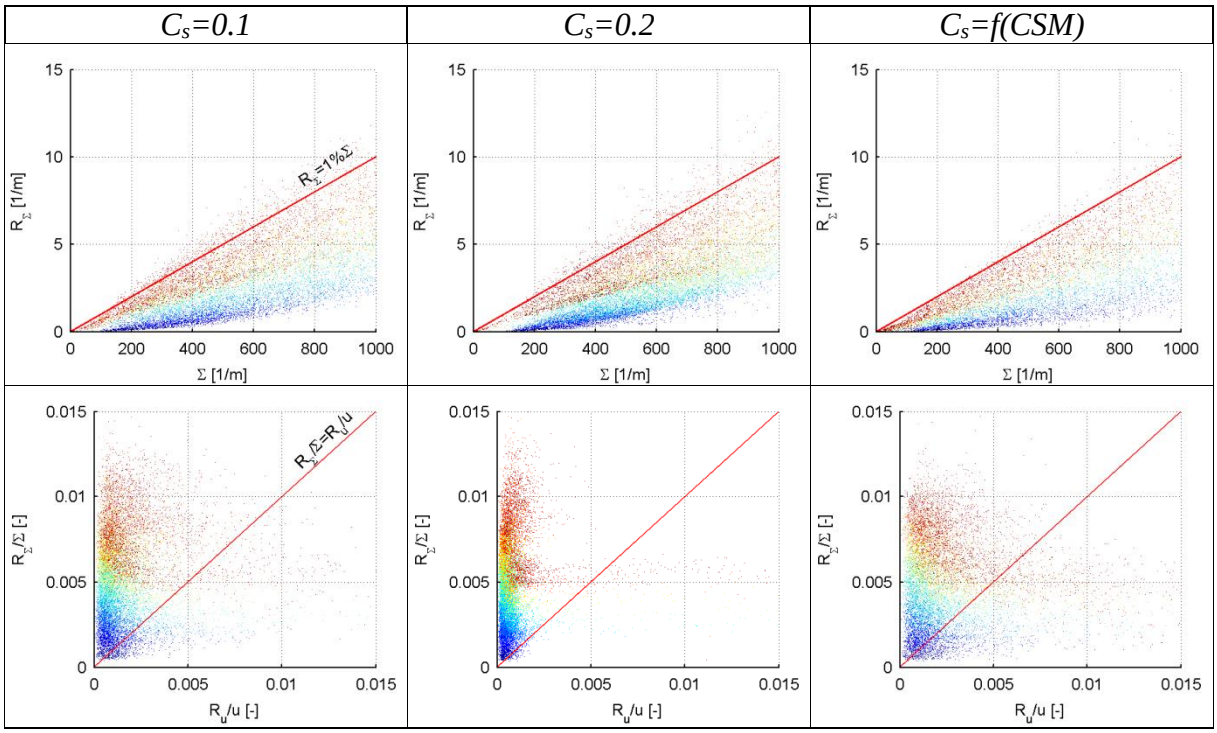

Figure 42 - Flame F2: scatter plots of cell values for FSD vs. momentum normalized residual errors, coloured by RPV, for $C_s=0.1$, $C_s=0.2$ & $C_s=f(CSM)$; lines in upper diagrams

represents error of 1% (1% slope), while in lower diagrams line represents equality between cell values of relative errors (slope =1)

Finally, the domain-integrated values were compared between the each SGS approach. It can be seen that the ratio between the resolved and total solution is higher for domain-integrated turbulent kinetic energy than it is for the FSD. With the mesh resolution used in this work, approximately 25% of the FSD solution has to be modelled by SGS relations for $C_s=0.1$ and $C_s=f(CSM)$. Approach with $C_s=0.2$ has the lowest values of resolved-to-total ratio, having SGS contribution of 20% for TKE and 35% for FSD.

Table 5 - Integral values of resolved-to-total ratio and cell residuals for turbulent kinetic energy and FSD (for cell residuals, only cells with RR>0 are taken into account)

	$C_s=0.1$	$C_s=0.2$	$C_s=f(CSM)$
$R_k^{\%,res}$, [%]	95	83	93
$R_\Sigma^{\%,res}$, [%]	75	66	72
$R_{k\|RR>0}$, [%]	0.3	0.1	0.6
$R_{\Sigma\|RR>0}$, [%]	0.5	0.5	0.5

Cell residuals have been integrated over the region of the flame, identified with criteria that RR has is larger than zero (RR>0). It shows very low values (below 1%) for both momentum and FSD. This indicates that that effect of numerical error is small inside the flame region. This result is important, since convergence criteria during the simulation integrated throughout the whole domain (not only where RR>0), in which flame region occupies negligible portion of cells.

6.3 Premixed methane-air swirl burner (flame PSF30)

This case represents swirling premixed unconfined methane/air flame. Reference experiment, as well as experimental data can be fund in paper from Schneider et al. [51]. Fresh mixture is lean. Lean premixed swirling flames are getting importance in technical systems (especially in low-NOx gas turbine combustors), since they feature reduced formation of pollutants due to lean combustion. Location in the combustion diagram is inside the thin reaction zone region. Comparison between experimental and simulated locations is provided in Figure 43. It can be seen that simulation matches well with the experiment. Inputs for regime diagram have been recorded at the location *x=10mm, r=25mm*.

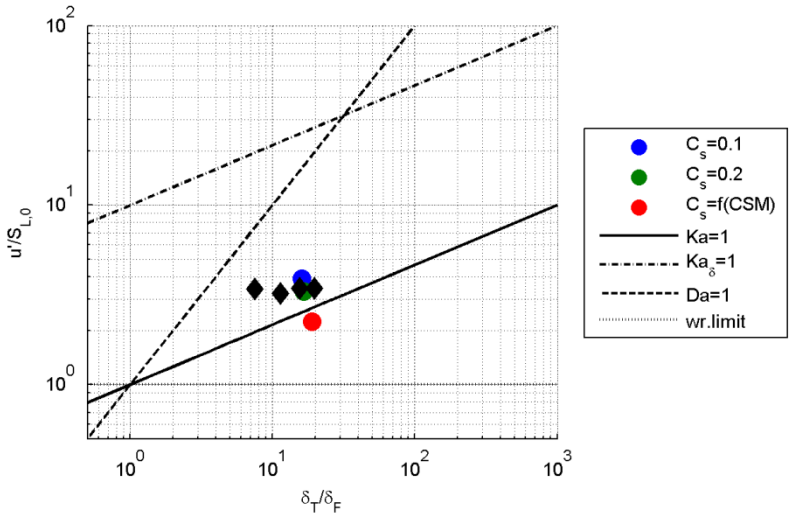

Figure 43 - Combustion regime diagram for flame PSF30 with plotted lines separating the regimes

The focus in investigating this flame was combustion stability limits due to lean combustion associated to flashback and flame blow-out. However, configurations presented in the reference paper were stable steady by the mean properties of the flames.

This test case was already used for validation of thickened flame approach [84] and F_TACLES combustion model with dynamic SGS approach [85]. Results of the simulation will be validated against the experimental data by radial profiles of mean velocity, RPV (defined via temperature) and main species (CH4 and CO2), as well as RMS profiles of velocity and RPV fluctuation, for five axial locations (10, 20, 30 and 60 mm).

6.3.1 Experimental configuration

The experiment was performed by Schneider, Dreizler and Janicka in 2005 [51]. Schematic view of experiment configuration is shown in Figure 44.

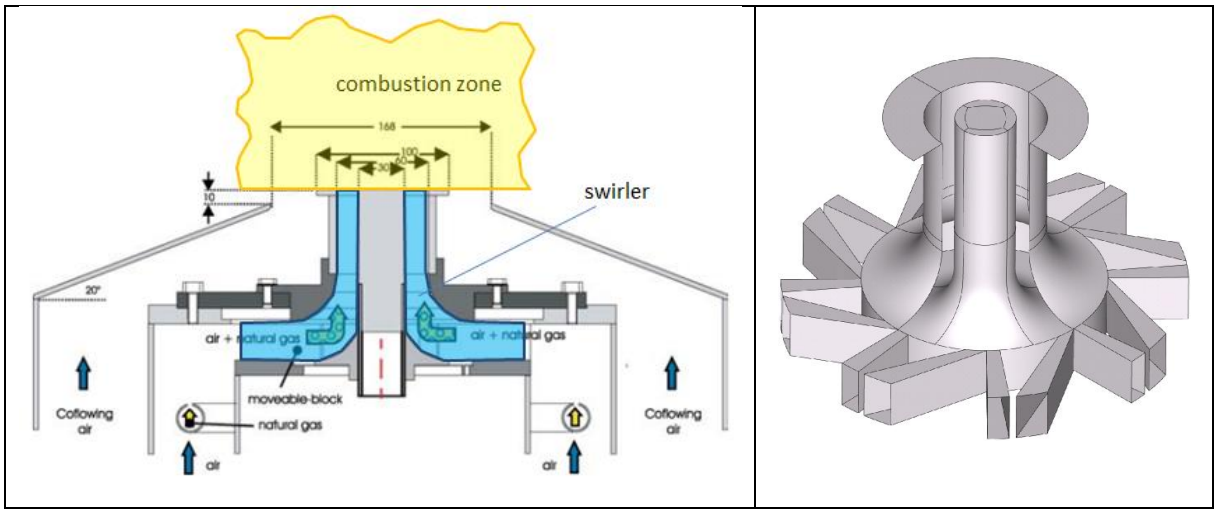

Figure 44 - Schematic view of the experimental configuration. (Source: Schneider, Dreizler and Janicka in 2005 [51])

Swirl is generated by a moveable block which can be adjusted in order to introduce proper ratio between tangential and radial mass flow. This results in a swirl which is then lifted towards the entrance into the combustion domain. Fresh mixture is a lean premixed methane-air mixture at equivalence ratio $\phi = 0.833$.

Different configurations for the PSF flames can be overviewed in Table 6.

Table 6 - Different premixed swirling flames (PSF) investigated on the unconfined swirl burner.

Variable	Flame configuration		
name	PSF-30	PSF-90	PSF-150
$S_{0,th}$	0.75	0.75	0.75
P	30	90	150
ϕ	0.833	0.833	1.0
$Q^N_{h,gas}$	3.02	9.06	15.1
$Q^N_{h,air}$	34.91	104.33	145.45
Re_{tot}	10000	29900	42300
$S_{L,0}$	0.36	0.36	0.42
l_F	$0.26 \cdot 10^{-6}$	$0.26 \cdot 10^{-6}$	$0.18 \cdot 10^{-6}$

In this work simulation of flame PSF30 is performed.

6.3.2 Simulation set-up

Computational domain describing the geometry of the swirler and combustion chamber (Figure 44), is discretized into computational mesh with hexahedron cells with typical sizes between 1.5-2.5 mm in the flame region. Total number of cells is approximately 1 million.

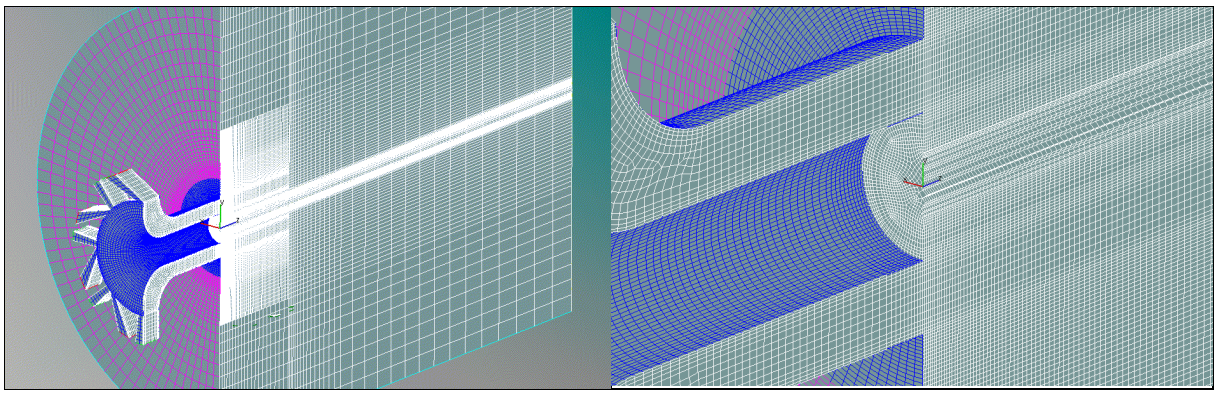

Figure 45 - Computational mesh for TECFLAM laboratory flame; swirler is included in the domain

The swirler is included in the computational domain, meaning that the flow field is fully reproduced according to the experiment prior to the entrance into the combustion chamber. Boundary conditions for the swirler part are two inlets, one fully radial and other having radial

and tangential component. They can be seen in Figure 47. Ratio between mass flows for two inlets has to be found, since small variations in this ratio has large influence on simulation results

In experiment, the swirl number is achieved by adjusting the the angle of moveable block in geometry, according to theoretical swirl number:

$$S_{0,th} = \frac{\pi}{n\xi_m} \frac{\sin(\alpha)\cos(\alpha)\left[1+\tan(\alpha)\tan\left(\frac{\xi}{2}\right)\right]\frac{\xi}{\xi_m}}{\left\{1-\left[1-\cos(\alpha)\left(\tan(\alpha)\tan\left(\frac{\xi}{2}\right)\right)\right]\frac{\xi}{\xi_m}\right\}^2} \frac{R_0}{B}\left[1-\left(\frac{2r_0}{2R_0}\right)^2\right] \tag{6-6}$$

Graphical representation of former equation is depicted in Figure 46.

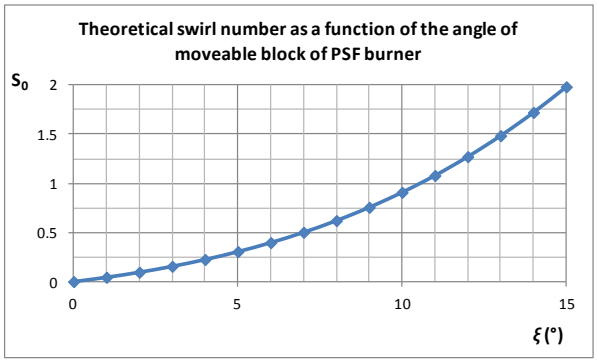

Figure 46 - Theoretical swirl number as a function of the angle of PSF' burner moveable block.

Target swirl number is $S_{0,th} = 0.75$. It can be seen that for this swirl number angle $\xi = 9°$ is used. Experimental geometry and computational domain was designed with that angle. However, actual swirl number reported in the experiment was 0.64, which is 15% less than the theoretical value.

Outlet boundary conditions defined in the same manner as for highly stretched flame, meaning that slipwall is defined on lateral boundary and NSCBC is defined on axial outlet.

Same as in the case for highly stretched flame, simulation of isothermal flow is performed first and results for three velocity components (both mean and RMS) are compared with the experimental data.

The time step was set to *5μs* and convergence criteria was *1e-4* for momentum, energy and all scalars.

6.3.3 Isothermal flow - validation of boundary conditions

Simulations of isothermal flow are used for validation of mean and RMS values of three components of velocity (axial, radial and azimuthal) w.r.t. the values measured in the experiment under isothermal conditions. The importance of this simulation test is to see if swirler can correctly reproduce velocity field inside the combustion region and if yes, under which ratio of mass flows for '*inlet_1'* and '*inlet_2'*, see Figure 48.

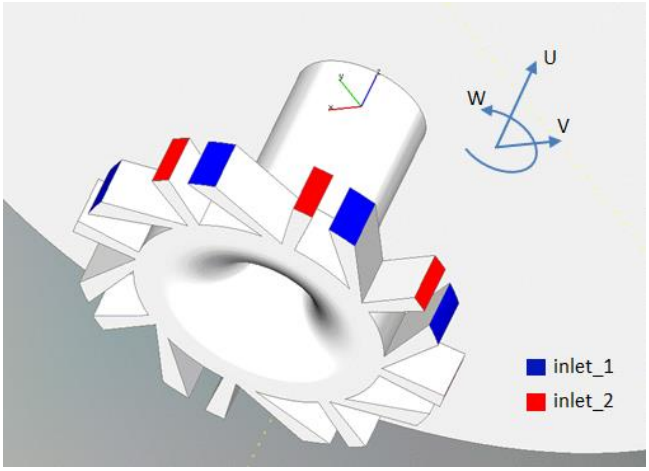

Figure 47 - 3D representation of the swirler with two inlets and axes of cylindrical coordinate system

Total mass flow entering the domain can easily be found from the normal volume flow reported in the experiment, but ratio between the two mass flows, entering '*inlet_1*' and '*inlet_2*', has to be determined since exact ratio is unknown. Some authors suggest that this ratio should be 54/46 in favour of mass flow entering '*inlet_1'*.

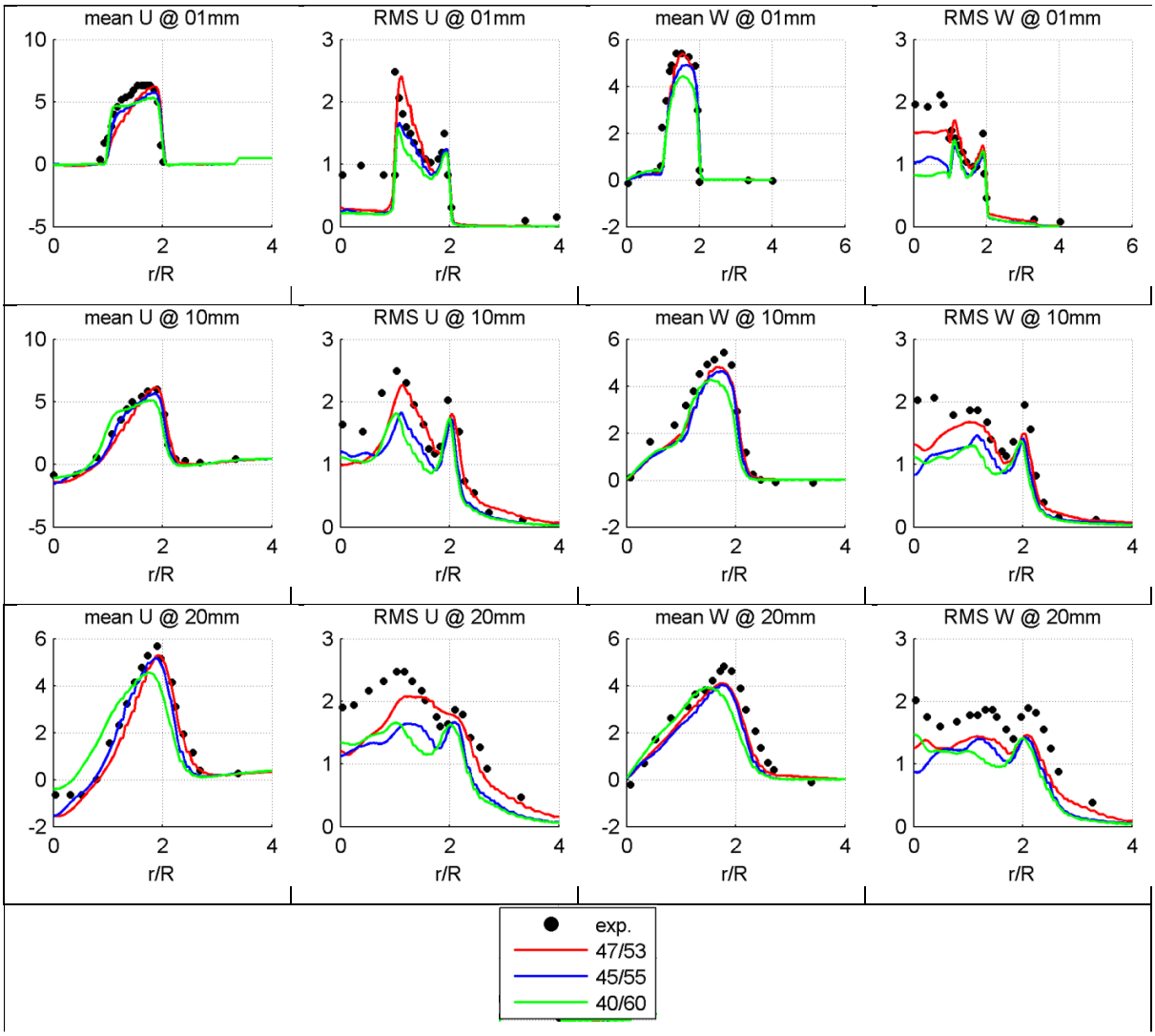

Figure 48 - TECFLAM isothermal flow: Mean and RMS values of axial (U) and tangential (W) velocity on three axial positions near the nozzle exit.

Results shows that the ratio of 47/53 provides best validation and this ratio is used for obtaining all results for reactive flow. Difference between simulation and experiment is more pronounced closer to the centreline, but generally stay below 5% for mean and 25% for RMS values.

Swirl is obtained from the resolved velocity field by using the common definition by Gupta et al. [86]:

$$S_0 = \frac{\int_{R_1}^{R_2} (wur)dr}{\int_{R_1}^{R_2} (uur)dr} \tag{6-7}$$

Swirl number equal to 0.62 is obtained from the simulation, which is close to the experimentally achieved value of 0.65.

6.3.4 Reactive flow

Figure 48 indicates that highest amount of wrinkling is present in CSM approach. It can also be observed that approaches C_s=f (CSM) and C_s=0.1 enables the fresh mixture to penetrate deeper into the flame when compared to the case C_s=0.2.

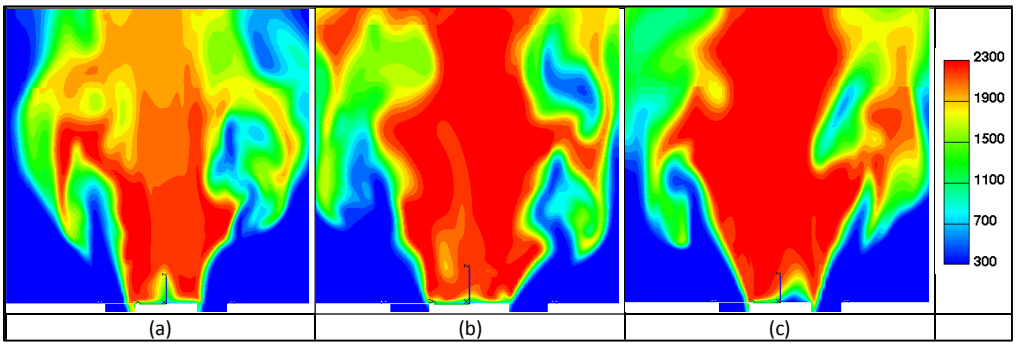

Figure 49 - Flame PSF30: qualitative difference in fields of temperature between C_s=f (CSM) (a), C_s=0.1 (b) and C_s=0.2 (c)

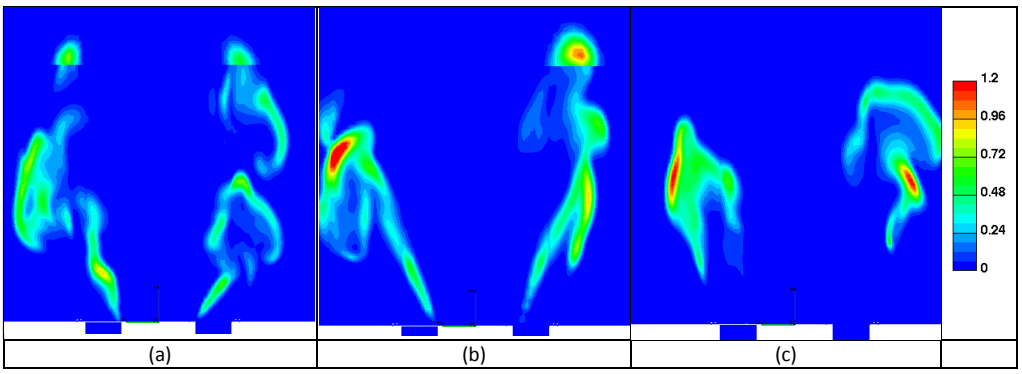

Figure 50 - Flame PSF30: qualitative difference in fields of reaction rate between C_s=f (CSM) (a), C_s=0.1 (b) and C_s=0.2 (c)

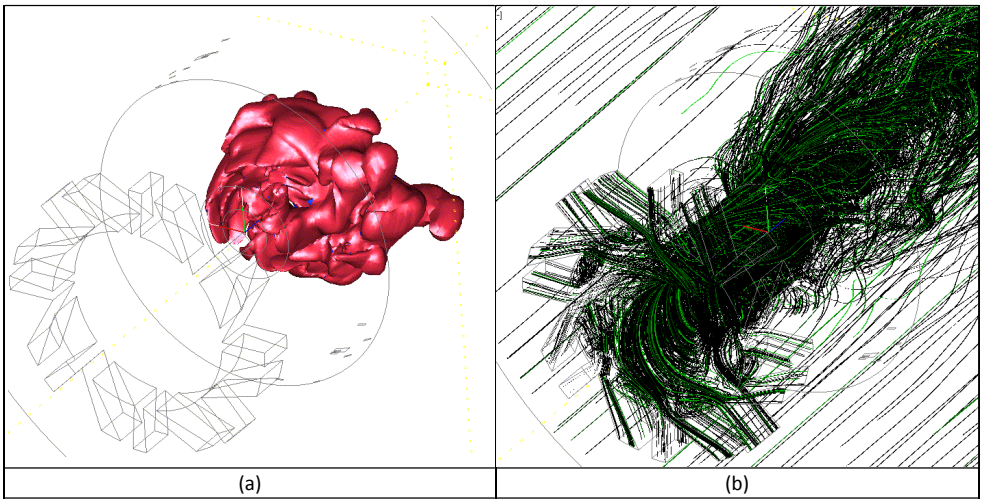

Figure 51 - Flame PSF30: Iso-surface of instantaneous reaction rate (left) and streamlines at nozzle entrance to the combustion chamber (right)

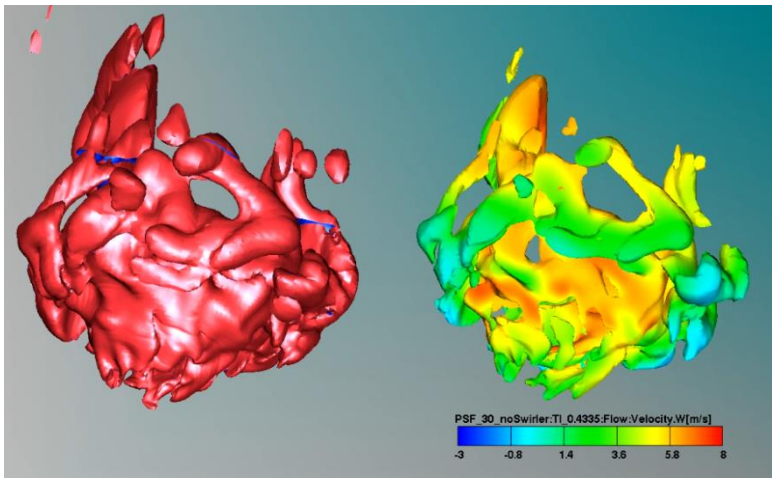

Figure 52 - Colourless instantaneous isosurface of reaction rate at value of 0.1 J/s (left) and isosurface of same reaction rate coloured by axial velocity for the case of CSM turbulent transport for the flame PSF-30 (right).

Results were averaged over the time period of 50 ms.

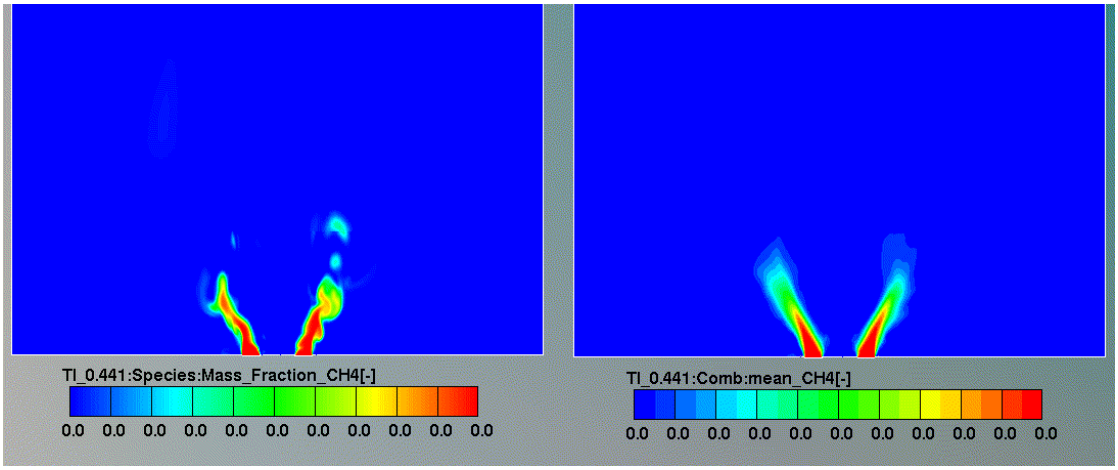

Figure 53 - Instantaneous and mean CH4 mass fraction

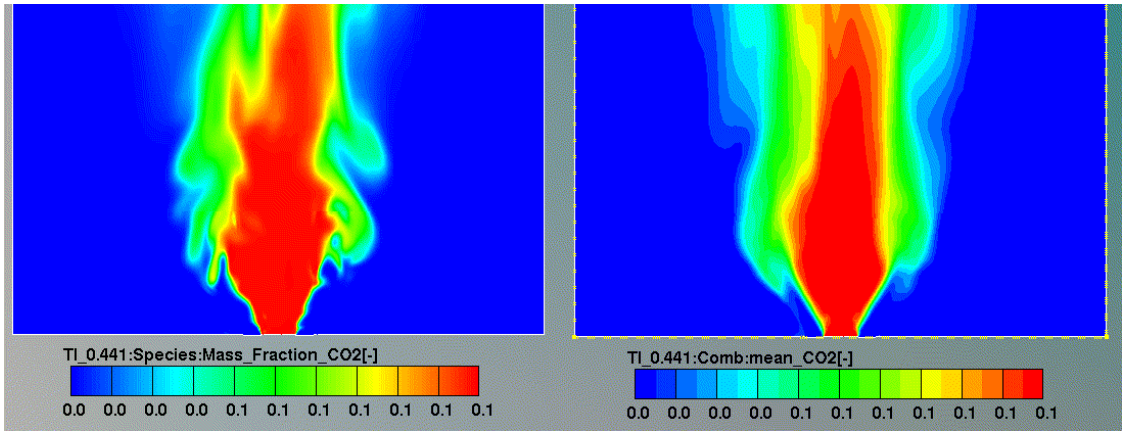

Figure 54 - Instantaneous and mean CO2 mass fraction

6.3.4.1 Validation of mean and RMS flame quantities vs. experimental data

Mean and RMS temperature profiles are presented in Figure 55. Radial profiles of temperature shows that all three approaches have a mismatch from the experiment and that CSM approach has better match when compared to other two. This may be a consequence of lowest reaction rate in CSM approach, as it was previously mentioned.

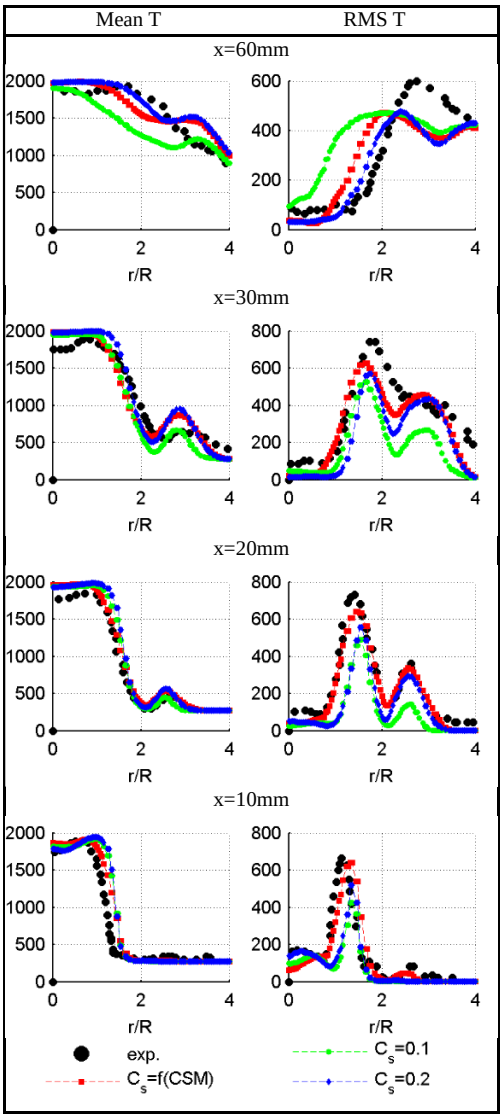

Figure 55 - Flame PSF30: mean and RMS of temperature at different axial distances from the inlet to combustion chamber

Radial profiles of mean values of CH4 and CO2 are showing the same trend and for the flame F2, meaning that even if the temperature is over predicted in lower axial positions, the CH4 is also over predicted. As mentioned before, probable cause for this is usage of a very simple chemistry modelling of the combustion process.

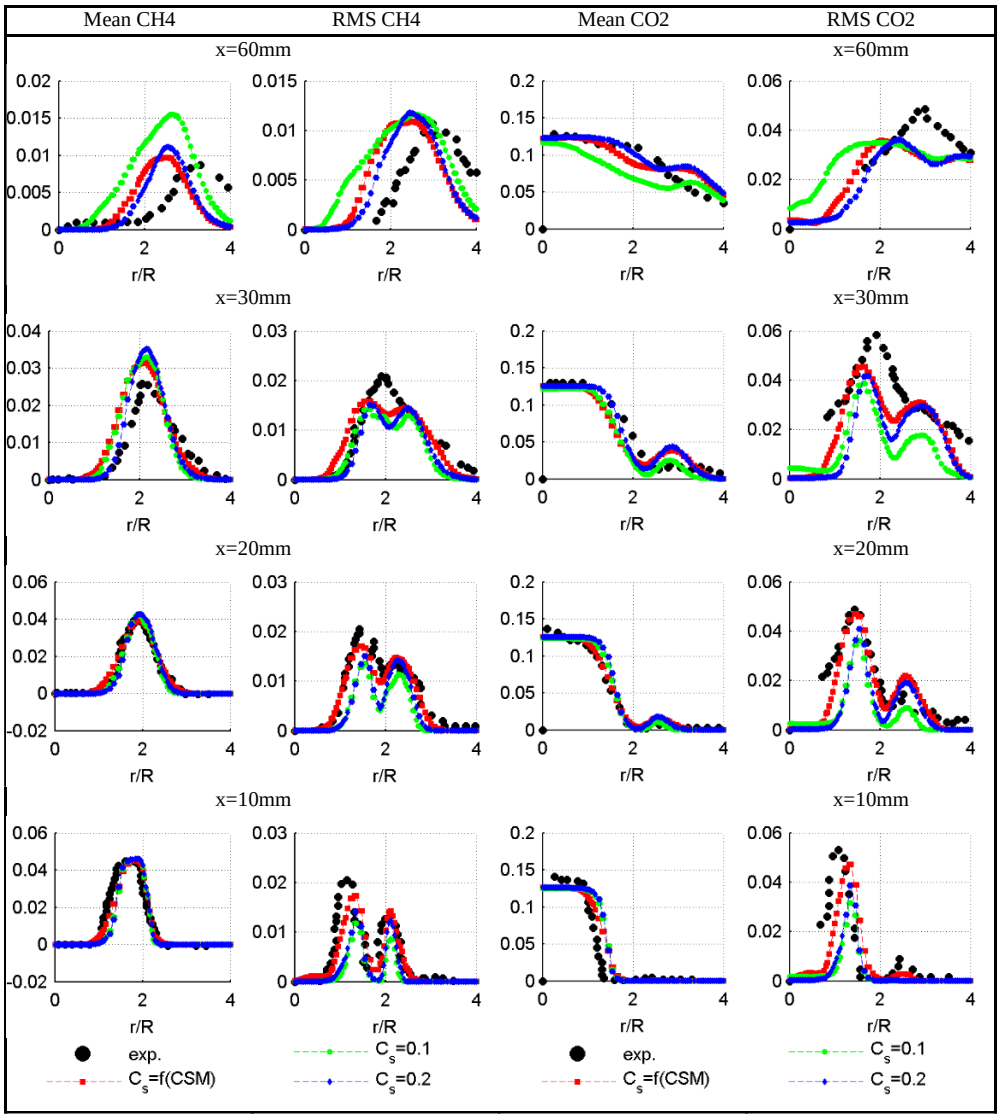

Figure 56 - Flame PSF30: mean and RMS of CH4 and CO2 at different axial distances from the inlet to combustion chamber.

Mean and RMS values of axial and tangential velocity of the flame are represented in Figure 57. RMS values were calculated in the standard way.

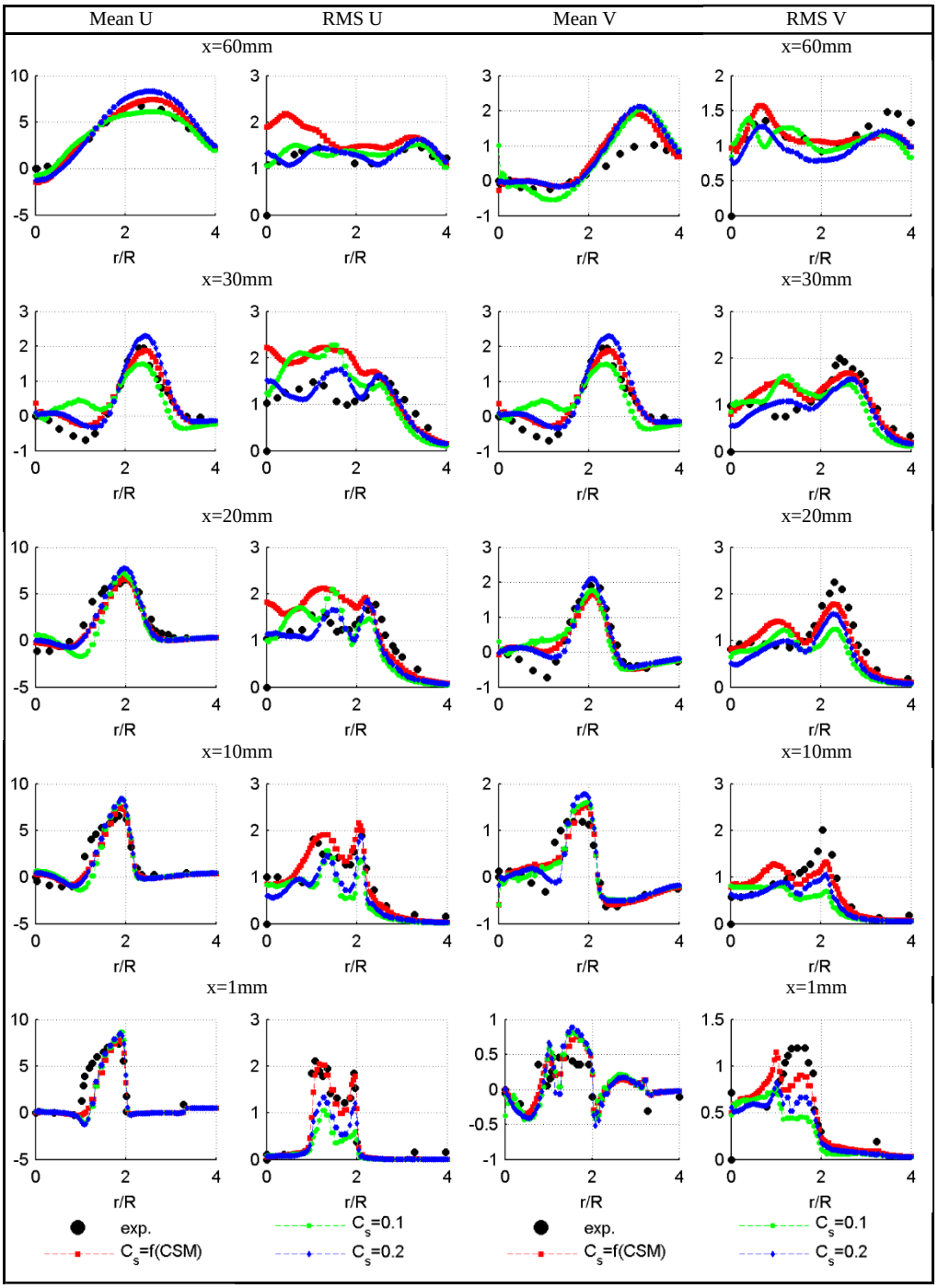

Figure 57 - Flame PSF 30: mean and RMS of axial and radial velocity at several axial positions

The results of the mean axial velocities for all three approaches were similar. There is a difference between simulated profiles and experiment at the zone where flame emerges from the inner radius of the inlet. This might be a consequence of a too excessive reaction rate, which prevents axial entrance of the fresh mixture on lower radius, thus shifting the mass flow towards the outer radius of the inlet. The reason for that may be a very simple chemistry model or

improper solution of the flow inside the swirler as a consequence of too coarse mesh. When comparing RMS values of axial fluctuations, CSM approach reproduces more fluctuations than other two approaches and even accomplishes very good agreement near the nozzle inlet from the swirler. Radial profiles of tangential velocity are indicating that the flame emerging from the inside radius of the inlet speeds up tangential part of the velocity field. This is least visible in case of CSM. Possible reason for that is the influence that C_s has on the combustion model, especially on the SGS contribution for FSD balance equation and turbulent viscosity. These results indicate that mesh resolution should be increased in order to reduce this effect. Root mean squared values of tangential fluctuations are reproduced well on all axial positions, with CSM approach having best match with the experiment.

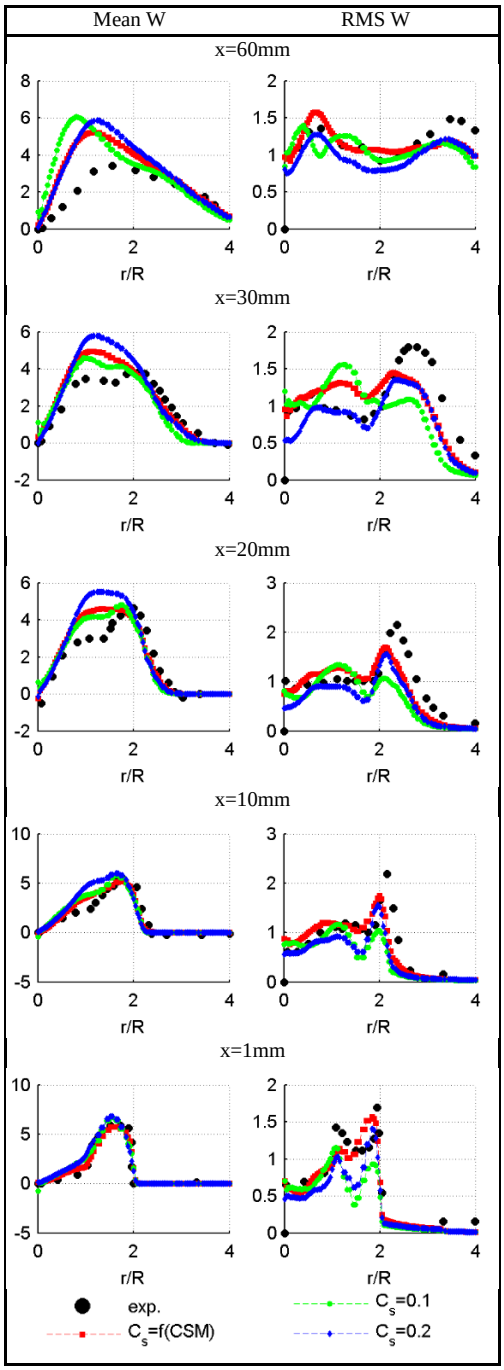

Figure 58 - Flame PSF 30: mean and RMS of tangential velocity at several axial positions.

6.3.4.2 Influence of different SGS models on flame properties

Ratio between SGS and resolved FSD source terms presented in Figure 59 shows that the distribution is more compact in the case with lower C_s, which is in contrast to analysis given for the flame F2. For low reaction rates the $C_s=0.1$ approach has more influence of resolved than SGS part, while for the $C_s=0.2$ approach resolved and SGS part get more equal significance. The CSM approach has lies between the former two approaches which means that

this approach does not scatter around the center point (0,0), as observed in the case for flame F2.

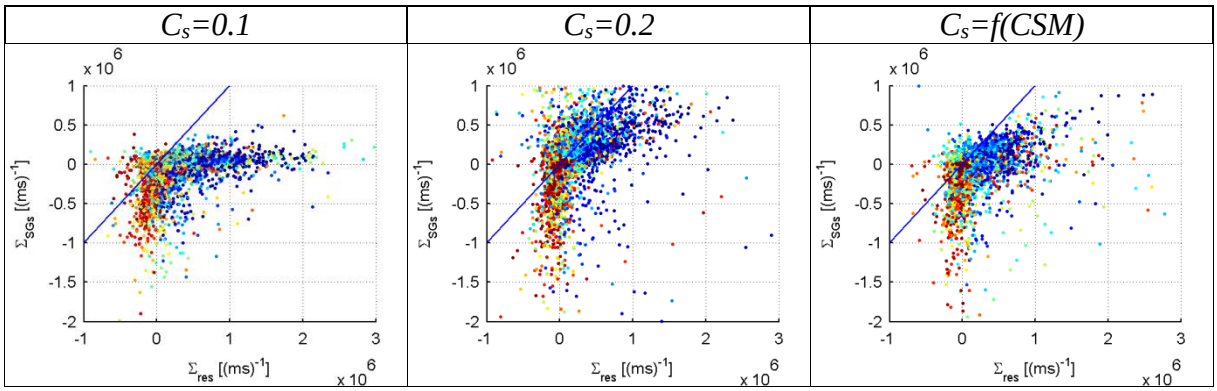

Figure 59 - Flame PSF30: scatter plots of cell values for resolved vs. SGS FSD source terms, coloured by RR for C_s=0.1, C_s=0.2 & C_s=f(CSM)

Distribution of reaction rate across the flame, presented in Figure 60, shows that for all three approaches, the largest reaction rate is in the middle of the flame. In contrast to the flame F2, here CSM approach also follows this trend without excessive scattering. Vorticity inside the flame is present but not in such levels as in the flame F2. It looks like its level is decreasing towards the end of the flame (identified by higher levels of RPV), indicating the flame-induced laminarization of the flow field.

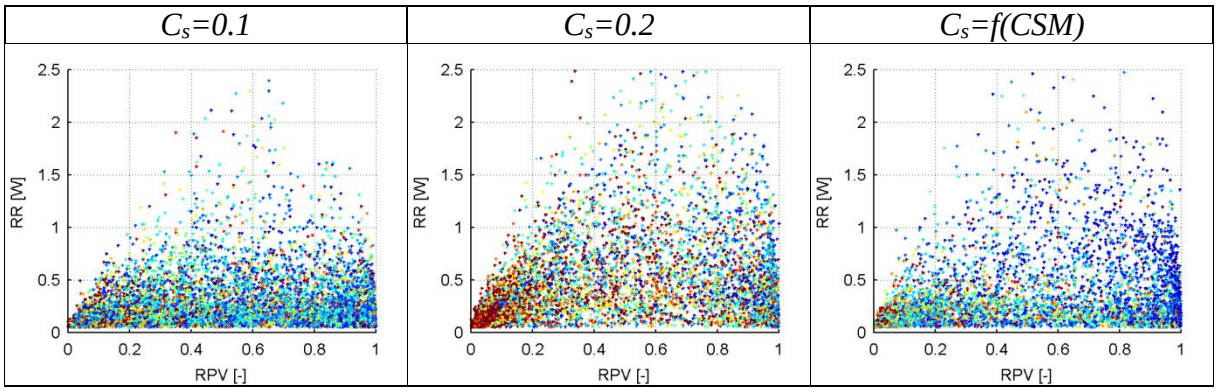

Figure 60 - Flame PSF30: scatter plots of cell values for RR vs. RPV, coloured by vorticity, for C_s=0.1, C_s=0.2 & C_s=f(CSM)

Values of controlling parameter F is not declining throughout the flame (Figure 61), as in the case for the flame F2.

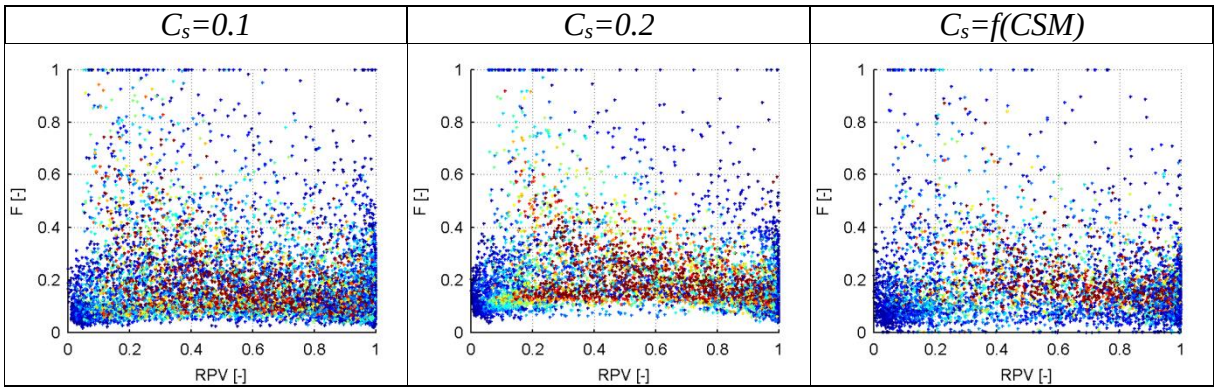

Figure 61 - Flame PSF30: scatter plots of cell values for controlling factor F vs. RPV, coloured by RR for $C_s=0.1$, $C_s=0.2$ & $C_s=f(CSM)$

F-diagram in Figure 38 depicts the difference between the three SGS approaches. Approach Cs=0.2 has highest values of SGS turbulent velocity and slightly higher values of controlling parameter F than the approach where $C_s=0.1$. Values of F were significantly lower than its values in flame F2 that brings out the conclusion that this flame is more controlled than the flame F2. Low values of controlling parameter increase the SGS strain source for FSD, as seen in Eq. (2-51).

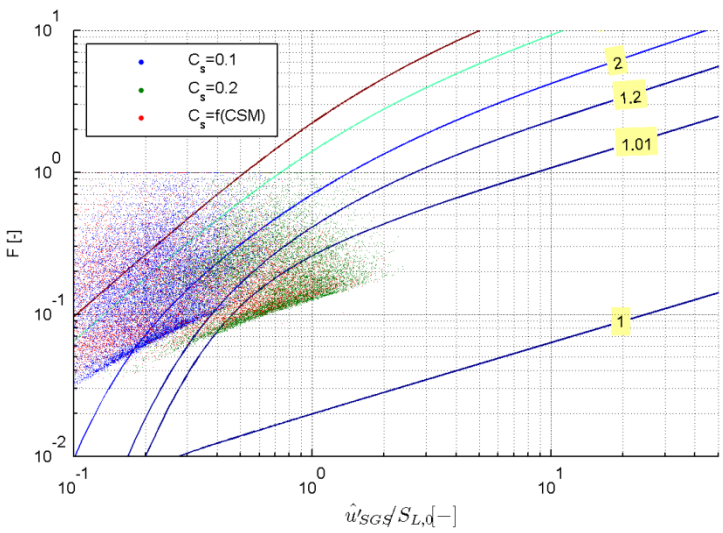

Figure 62 - Flame PSF30: cell values of controlling factor F for $C_s=0.1$, $C_s=0.2$ & $C_s=f(CSM)$; lines are different parameters of $\hat{\Delta}/\Delta_x$

6.3.4.3 Flame quenching

This flame is not characterized with high δ_q/δ_t ratio and this is clearly visible in Figure 63, where the cell values of δ_q/δ_t ratio remain mostly below 1%.

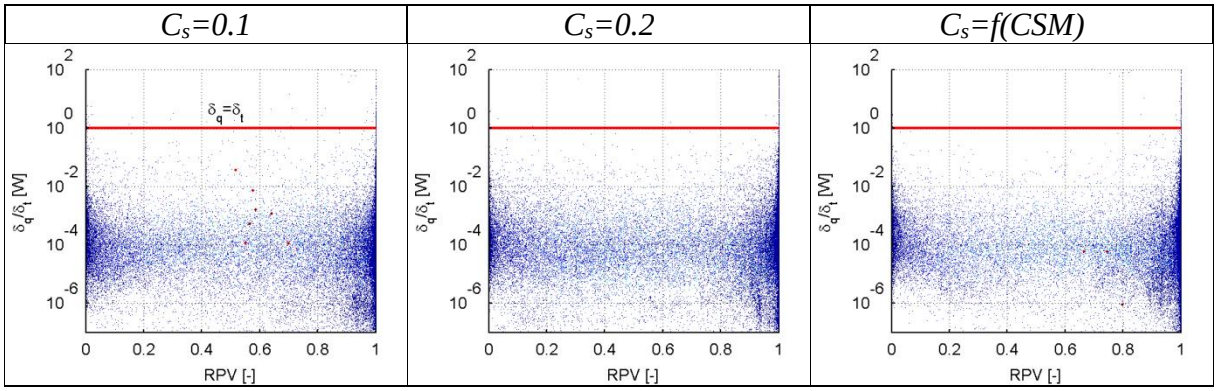

Figure 63 - Flame PSF30: scatter plots of cell values for δ_q/δ_t ratio vs. RPV, coloured by RR; horizontal line represents limit where $\delta_q/\delta_t = 1$ (above that limit flame quenching can be expected)

Difference in cell values of quench-to-turbulent scale ratio between flames F2 and PSF30 clearly show the difference in flame structure between them.

6.3.4.4 Parameter C_s

Similar as in the case for highly stretched flame, decreasing of C_s with the increasing vorticity can be observed. Larger cell values of RR are also scattered across the whole vorticity range, but still most of them are present at low vorticity.

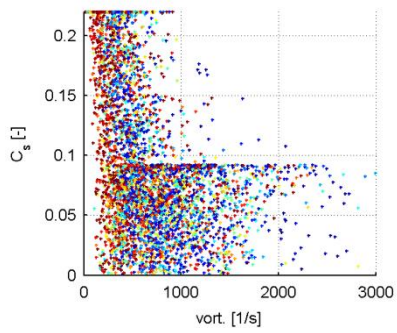

Figure 64 - Flame PSF30: scatter plot of cell values for Smagorinsky parameter C_S vs. vorticity for C_s=*f(CSM)*, coloured by RPV

6.3.4.5 Error analysis

Most of the cell values of TKE throughout the domain have more contribution from the resolved than the SGS side. This is most pronounced in case where $C_s=0.1$. Cell values for CSM approach are mostly scattered, covering both ranges of $C_s=0.1$ and $C_s=0.2$.

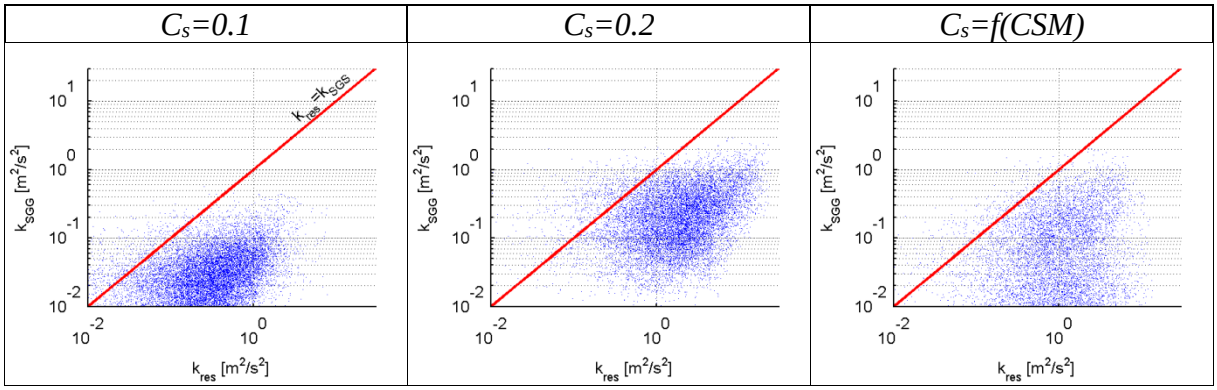

Figure 65 - Flame PSF30: scatter plots of cell values for resolved vs. SGS turbulent kinetic energy for $C_s=0.1$, $C_s=0.2$ & $C_s=f(CSM)$; line represents equality between resolved and SGS TKE

The ratio between cell values of residuals and the nominal solution, presented in Figure 66, peaks at approximately 8%, which is higher than in the case of highly stretched flame, where this peak value was around 1% (Figure 42).

Analysis of normalized residuals indicates that residuals of the FSD are 10 times higher than residuals for momentum, which was also the case for highly stretched flame. Also, this difference is more pronounced towards the end of the flame (higher values of RPV).

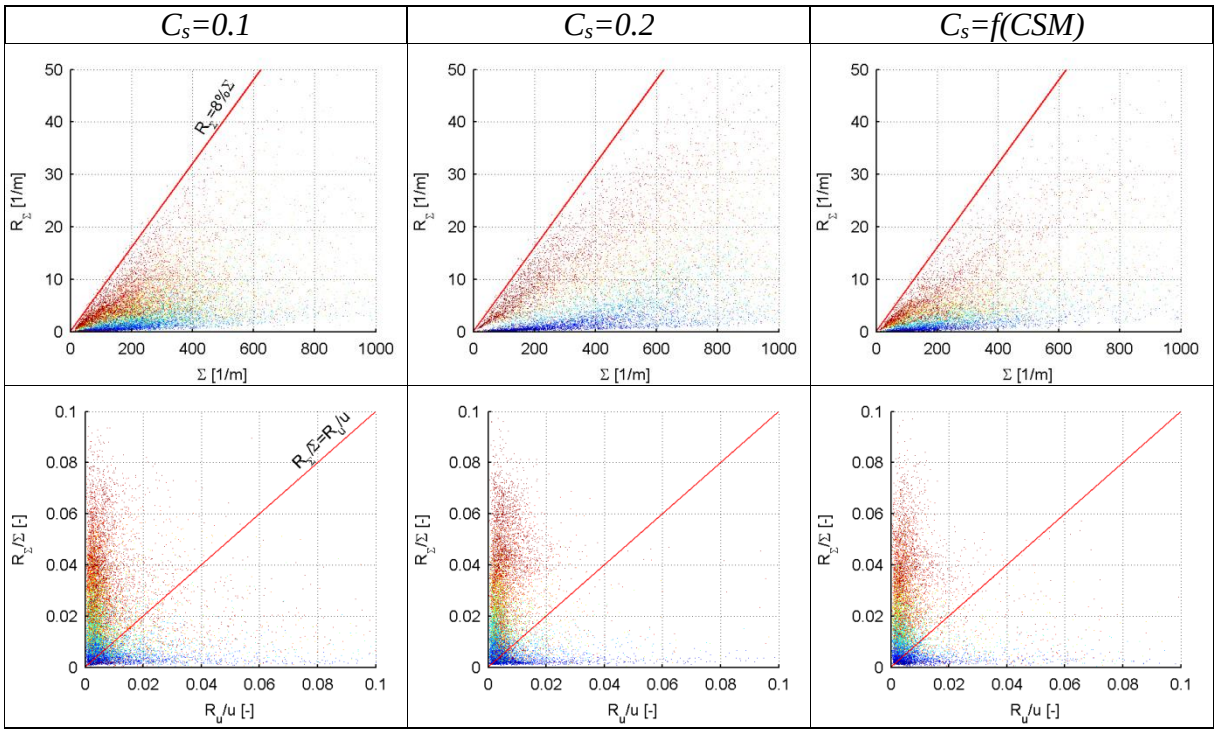

Figure 66 - Flame PSF30: scatter plots of cell values for FSD vs. momentum normalized residual errors, coloured by RPV, for $C_s=0.1$, $C_s=0.2$ & $C_s=f(CSM)$; lines in upper diagrams represents error of 1% (1% slope), while in lower diagrams line represents equality between cell values of relative errors (slope =1)

Comparison of domain-integrated values for the three SGS approaches reveals that the ratio between the resolved and total solution is higher for turbulent kinetic energy (above 80% for worst case $C_s=0.2$) than it is for the FSD (only 46% for the same case). Higher values of C_s lead to higher influence of SGS part in the overall solution. The CSM approach acts similar to $C_s=0.1$.

Table 7 - Integral values of resolved-to-total ratio and cell residuals for turbulent kinetic energy and FSD (for cell residuals, only cells with RR>0 are taken into account)

	$C_s=0.1$	$C_s=0.2$	$C_s=f(CSM)$
$R_k^{\%,res}$, [%]	95	80	92
$R_\Sigma^{\%,res}$, [%]	61	46	61
$R_{k\|RR>0}$, [%]	1.5	1.0	1.2
$R_{\Sigma\|RR>0}$, [%]	2.4	2.7	1.7

Domain-integrated values of cell residuals in flame region (identified with RR>0), shows that residuals do not exceed 1.5% for turbulent kinetic energy and 3% for FSD. These normalized values were much higher than for the highly stretched flame, where normalized residuals within the flame were less than 0.5% for both FSD and velocity magnitude.

6.4 Discussion of results with comparative analysis between flames F2 and PSF30

The quality of simulation for two flames F2 and PSF30 can be evaluated from direct validation against experimental data, as well as qualitative evaluation for specific flame features, e.g. ratio between the quench and turbulent length scale inside the flame. As mentioned before, under the assumption that experimental data is accurate, simulation errors may come from the modelling, numerical or discretization side. In addition, errors may appear due to wrong simulation setup, such as inappropriate definition of boundary conditions. The discrepancy between simulated and experimental data, as well as assessment on influence for each type of error is given in Table 8. Validation is performed by qualitative analysis of axial velocity and temperature matching the experimental data at the first and last axial point where radial profiles were recorded. Numbers were rounded to the value of five. Error assessment for BC were also a comparison of isothermal simulations against isothermal experiments. Mean and RMS values of axial velocities have been compared. Influence of SGS (modelled) contribution to the overall solution is simply derived from equations (6-1) and (6-2) and values presented in Table 5 and Table 7. Numerical errors are defined as an integral of the normalized cell residuals for the cells inside the flame region (identified by RR>0) and have been taken from the same tables. Assessment of discretization errors was performed by using the results from verification tests (Figure 17 and Figure 21), by taking the criteria that mesh resolution is between 1.2-1.5mm, which is larger than the value used in the verification.

Table 8 - Comparison between flame F2 and PSF30 by validation against experimental data and error assessment

flame	F2			PSF30		
C_s	*0.1*	*0.2*	*f(CSM)*	*0.1*	*0.2*	*f(CSM)*
difference to experiment						
v_{ax} @ x_{min} [%]	~20	~20	~20	~10	~10	~10
v_{ax} @ x_{max} [%]	<5	<5	<5	~10	~25	~10
T @ x_{min} [%]	>50	>50	>50	~15	~20	~25
T @ x_{max} [%]	<5	<5	<5	~10	~25	<5
error assesment						
mean BC [%]	~10			~5		
RMS BC [%]	~10			~25		
$100\% - R_k^{\%,res}$ [%]	15	17	7	5	10	8
$100\% - R_\Sigma^{\%,res}$ [%]	25	33	28	39	54	39
$R_{k\|RR>0}$, [%]	0.3	0.1	0.6	1.5	1.0	1.2
$R_{\Sigma\|RR>0}$, [%]	0.5	0.5	0.5	2.4	2.7	1.7
discretization, mesh[%]	>8-25	>1-10	>1-10	>8-25	>1-10	>1-10
discretization, time [%]	~0	~0	~0	~0	~0	~0

In this analysis it has to be noticed that error arising from the modelling of chemistry is not taken into account. Errors from the used SCRS may be significant since SCRS is not taking into account intermediate species which may occur during the flame quenching due to flame stretch, especially at the beginning of the flame F2 (this can be seen in Figure 29).

For both flames the discrepancy between the simulation results and the experimental data are by magnitude between 10-20%, based on the qualitative analysis of the simulation results. Based on Table 8, this difference is most probably a consequence of discretization, which can be avoided by using the more refined mesh. With increase in mesh resolution both the discretization and model errors would decrease. Gradients responsible for flame evolution would be captured more detailed and SGS terms would decrease since they implicitly or explicitly include cell size Δ_x.

Root-mean-squared values of velocity and temperature (as well as main chemical species for the flame PSF30) show higher deviation form the experiment than mean values. Reason for that is also mesh resolution. Nevertheless, from the comparison between three values of Cs used, it is clearly visible using the CSM approach results in higher level of fluctuations than using constant values of 0.1 and 0.2. This may be explained by examining Figure 40 and Figure 64. For higher values of vorticity, C_s can fall almost to zero which reduces the SGS viscosity and smoothening of the fluctuations inside the flow field.

Flame quenching analysis shows that flame F2 possesses high stretch rates, comparable to turbulent length scale. This is exactly what experiment was performed for - to investigate quenching due to flame stretch. Flame PSF30 has 100 times lower stretch rates and there was no record on experimentally determined stretch rates for this case. Since inlet velocity from the swirler is relatively low (just 10 m/s) no high stretch rates are expected.

7 Conclusions

Two significantly different flames, the highly stretched flame F2 and the swirling flame PSF30, were simulated, each with three different values of Smagorinsky parameter C_s. The first approach was the CSF approach which modifies C_s according to the local coherence in the flow and other two are approaches with constant C_s, namely $C_s=0.1$ and $C_s=0.2$.

For both flames the CSM approach showed the best results in terms of the mean and RMS values of velocity, temperature and main species. This is most probably due to the fact that CSM allows locally a decrease of C_s values in regions with high coherence in the velocity field. As a consequence, vortices from the side of the fresh mixture can be sustained without being dissipated for a sufficiently long time to penetrate into the flame front and change its curvature. Locally this can lead to higher reaction rates, but also to high quench rates due to flame stretch, as observed in the case for flame F2. On the other hand, decreased C_s reduces the influence of modelling terms that directly or indirectly take into account the value of C_s, for example the SGS turbulent transport in FSD equation or turbulent viscosity in the enthalpy and momentum equations, leading to the reduced diffusion of FSD, enthalpy or velocity field. This can be observed on both flames.

Flame quench analysis shows that the proposed method can be used for determining the local flame stretch rates and can be used to define local quench points within the flame.

Error analysis indicates that most of the errors come from the insufficient mesh resolution. By reducing the cell size two errors would be reduced - the discretization error and the modelling error (the SGS contribution). It is still an unknown what is the influence of using the very simple SCRS as a chemistry framework. Further work is needed in the direction of using the more sophisticated coupling between chemical reactions and flame tracking via FSD.

Appendix A- Vortex method inflow boundary condition

Vortices are characterized by their position $\vec{x}^{v}$, orientation $\vec{\varepsilon}^{v}$ and circulation Γ. Position vector is pointing to the origin of the orientation vector. Initial position of vortices, as well as their orientation, is obtained from random number generator.

Characteristic half-size of the turbulent structures is provided by the well-known relation for turbulence length scale. This value is dependent on the local turbulent kinetic energy and length scale.

$$\sigma = f\left(k,\varepsilon,\vec{x}^{v}\right) = \frac{C_{\mu}^{3/4} k\left(\vec{x}^{v}\right)^{3/2}}{2\varepsilon\left(\vec{x}^{v}\right)} \tag{A-1}$$

Number of turbulent structures imposed is given by the simple relation:

$$N = f\left(\sigma\right) = \frac{D_h}{\sigma^2 \pi} \tag{A-2}$$

Structures (2D vortices) are introduced directly on the boundary face. This velocity field is representing turbulent fluctuations.

$$\vec{u}'_{||BF}\left(\vec{x}\right) = \frac{1}{2\pi}\sum_{k=1}^{N}\left\{\underbrace{\left[\Gamma_k\left(\vec{x}\right)\frac{\vec{d}_{\perp\varepsilon}\times\vec{\varepsilon}}{\left|\vec{d}\right|^2}\left(1-\exp\left(-\frac{\left|\vec{d}_{\perp\varepsilon}\right|^2}{2\sigma^2}\right)\right)\exp\left(-\frac{\left|\vec{d}_{\perp\varepsilon}\right|^2}{2\sigma^2}\right)\right]}_{\text{2D vortex structure}}\right\} \tag{A-3}$$

Circulation, which represents magnitude of velocity fluctuations, is calculated w.r.t. local value of k [2]. Circulation has random sign.

$$\Gamma_k\left(\vec{x}\right) = \left(\pm 1\right) 4\sqrt{\frac{\pi k\left(\vec{x}\right)}{N 3\left(2\log\left(3\right)-3\log\left(2\right)\right)}N} \tag{A-4}$$

Geometrical quantities defining position and orientation of the vortex structure are:

$$\vec{d} = \left(\vec{x}_k^v - \vec{x}\right) \tag{A-5}$$

$$\vec{d}_{||\varepsilon} = \left(\vec{d} \cdot \vec{\varepsilon}\right)\vec{\varepsilon} \tag{A-6}$$

$$\vec{d}_{\perp\varepsilon} = \vec{d} - \vec{d}_{||\varepsilon} \tag{A-7}$$

Position of each vortex, defined by its position vector, is updated after each time step. Its movement is dependent on the 5% portion of 2D boundary surface velocity field.

$$\vec{x}^{v,new} = \vec{x}^{v,old} + 0.05\vec{u}_{||BF}^{old}\Delta t \tag{A-8}$$

Additionally, each vortex has its own life time of an existence on the boundary, which depends on the local integral turbulent values. After vortex life time has expired, vortex is removed and another one is introduced on a different random location.

$$\tau_v\left(\vec{x}^v\right) = \frac{k\left(\vec{x}^v\right)}{\varepsilon\left(\vec{x}^v\right)} \tag{A-9}$$

In order to represent impact on mean (streamwise) flow, linear kinetic model is introduced in order to account fluctuations in the streamwise direction [1, 2].

$$\vec{u}'_{\perp BF} = -\vec{u}'_{||BF} \cdot \frac{\nabla\vec{u}_m}{\left|\nabla\vec{u}_m\right|} \tag{A-10}$$

Finally, after all components of turbulent fluctuations have been determined, they should be added to the mean flow providing velocity boundary condition:

$$\vec{U} = (\vec{u}'_{\perp BF} + \vec{u}'_{||BF}) + \vec{u}_m \tag{A-11}$$

Appendix B- 3D NSCBC boundary conditions

According to Lodato et al. [17] for face boundaries.

Navier Stokes equations can be written in terms of wave amplitudes L_i.

$$L = \begin{pmatrix} \lambda_1 \left(\frac{\partial p}{\partial x_1} - \rho c \frac{\partial u_1}{\partial x_1} \right) \\ \lambda_2 \left(c^2 \frac{\partial \rho}{\partial x_1} - \frac{\partial p}{\partial x_1} \right) \\ \lambda_3 \frac{\partial u_2}{\partial x_1} \\ \lambda_4 \frac{\partial u_3}{\partial x_1} \\ \lambda_5 \left(\frac{\partial p}{\partial x_1} + \rho c \frac{\partial u_1}{\partial x_1} \right) \end{pmatrix}$$

For a boundary orthogonal to x_1 it reads:

$$\begin{cases} \frac{\partial \rho}{\partial t} + \frac{1}{c^2} \left[L_2 + \frac{1}{2} \left(L_5 + L_1 \right) \right] - T_1 = 0 \\ \frac{\partial u_1}{\partial t} + \frac{1}{2\rho c} \left(L_5 - L_1 \right) - T_2 = 0 \\ \frac{\partial u_2}{\partial t} + L_3 - T_3 = 0 \\ \frac{\partial u_2}{\partial t} + L_4 - T_4 = 0 \\ \frac{\partial p}{\partial t} + \frac{1}{2} \left(L_5 + L_1 \right) - T_5 = 0 \end{cases}$$

$$T = \begin{pmatrix} -\frac{\partial m_t}{\partial x_t} \\ -u_t \frac{\partial u_1}{\partial x_t} \\ -u_t \frac{\partial u_2}{\partial x_t} - \frac{1}{\rho} \frac{\partial p}{\partial x_2} \\ -u_t \frac{\partial u_3}{\partial x_t} - \frac{1}{\rho} \frac{\partial p}{\partial x_3} \\ -u_t \frac{\partial p}{\partial x_t} - \gamma p \frac{\partial u_t}{\partial x_t} \end{pmatrix}, t = 2,3$$

$$\lambda_1 = u_1 - c$$
$$\lambda_{2,3,4} = u_1$$
$$\lambda_5 = u_1 + c$$

Appendix C- derivation of the flame controlling parameter F

Controlling parameter can be derived from the natural flame brush thickness [3]:

$$\delta_{cn} = \frac{4S_L\left(\Xi_{eq}-1\right)\underbrace{\frac{\beta}{1+\tau}\left[\left(1+\tau\right)\left(\frac{1}{2}+\frac{\tau}{3}\right)-c^*\left(1+\tau+\frac{\tau^2}{3}\right)\right]}_{K_1}}{a_T} \tag{C-1}$$

where Ξ_{eq} is equilibrium wrinkling factor given by KPP analysis [87]:

$$\Xi_{eq} = \frac{S_{T,KPP}}{S_L} = 1+\frac{2}{S_L}\sqrt{\frac{\hat{\upsilon}_t a_t}{\underbrace{1-\frac{\beta c^*}{1+\tau}}_{K_2}}} \tag{C-2}$$

Controlling parameter is defined as $F = n_{res}\Delta_x/\delta_{cn}$ [3]. Inserting Eq. (C-1) into (C-2) using the formal definition, the controlling parameter can be written:

$$F = \frac{n_{res}\Delta_x a_T}{8K_1\sqrt{\frac{\left(D+\hat{D}_t\right)a_T}{\bar{\rho}(1-K_2)}}} \tag{C-3}$$

Appendix D- source terms for residual error analysis

In this appendix a derivation of the cheap method for determining numerical errors is derived for a set of equations used in this work. The general form of the equations is given first. This is followed by derivation of these equations for specific scalars.

Cell residual of momentum error is obtained by substituting scalar φ in eq. (3-3)-(3-6) with *k*-th component of the velocity field u_k. For each velocity component a set of three equations can be written:

$$R_P\left(\tilde{u}_k^o\right)=\sum_{f=1}^{N_f} S_f \cdot\left[\left(\rho\tilde{u}_i^o\right)_f \tilde{u}_k^o-\left(\rho D_\varphi\right)_f\left(\nabla\tilde{u}_k^o\right)_f\right]-\left(\nabla p\right)_k \tag{D-1}$$

$$R_P\left(\tilde{u}_k^n\right)=\sum_{f=1}^{N_f} S_f \cdot\left[\left(\rho\tilde{u}_i^n\right)_f \tilde{u}_k^n-\left(\rho D_\varphi\right)_f\left(\nabla\tilde{u}_k^n\right)_f\right]-\left(\nabla p\right)_k \tag{D-2}$$

$$R_F\left(\tilde{u}_k\right)=\frac{\left(\rho_P^n\tilde{u}_k^n\right)-\left(\rho_P^o\tilde{u}_k^o\right)}{\Delta t}V_P+\frac{1}{2}R_P\left(\tilde{u}_k^n\right)+\frac{1}{2}R_P\left(\tilde{u}_k^o\right) \tag{D-3}$$

The magnitude of the momentum error can be calculated from all three components:

$$R_F\left(\left|\tilde{u}_k\right|\right)=\left|R_F\left(\tilde{u}_k\right)\right| \tag{D-4}$$

Cell residual error for FSD is obtained if scalar φ is replaced with Σ. Then, Eq. (3-3)-(3-6) can be written in the following form:

$$R_P\left(\tilde{\Sigma}^n\right)=\sum_{f=1}^{N_f} S_f \cdot\left[\left(\rho\tilde{u}_i^n\right)_f \tilde{\Sigma}_f^n-\left(\rho D_\varphi\right)_f\left(\nabla\tilde{\Sigma}^n\right)_f\right]-S_\Sigma^n \tag{D-5}$$

$$R_P\left(\tilde{\Sigma}^0\right)=\sum_{f=1}^{N_f} S_f \cdot\left[\left(\rho\tilde{u}_i^o\right)_f \tilde{\Sigma}_f^o-\left(\rho D_\varphi\right)_f\left(\nabla\tilde{\Sigma}^o\right)_f\right]-S_\Sigma^o \tag{D-6}$$

$$R_F\left(\tilde{\Sigma}\right)=\frac{\left(\rho_P^n\tilde{\Sigma}_P^n\right)-\left(\rho_P^o\tilde{\Sigma}_P^o\right)}{\Delta t}V_P+\frac{1}{2}R_P\left(\tilde{\Sigma}^n\right)+\frac{1}{2}R_P\left(\tilde{\Sigma}^o\right) \tag{D-7}$$

Cell residual for a steady-state can be calculated:

$$R_P\left(\varphi\right)=\sum_{f=1}^{N_f} S_f \cdot\left[\left(\rho u_i\right)_f \varphi_f-\left(\rho D_\varphi\right)_f\left(\nabla\varphi\right)_f\right]-S_u V_P-S_P\varphi_P V_P$$

For transient cases total residual can be calculated as:

$$R_F(\varphi) = \frac{\left(\rho_P^n \varphi_P^n\right) - \left(\rho_P^o \varphi_P^o\right)}{\Delta t} V_P + \frac{1}{2} R_P\left(\varphi^n\right) + \frac{1}{2} R_P\left(\varphi^o\right)$$

Flame surface density

Equation for FSD (Eq. (2-51)) can be rewritten in the form of constant and linearized part of the source term:

$$\frac{\partial\left(\tilde{\Sigma}\right)}{\partial t} + \frac{\partial}{\partial x_j}\left(\tilde{u}_j \tilde{\Sigma}\right) = \frac{\partial}{\partial x_j}\left(\tilde{D}_\Sigma(\tilde{c}) \frac{\partial \tilde{\Sigma}}{\partial x_j}\right)$$
$$+ \underbrace{K_1 \tilde{\Sigma} + K_2 \tilde{\Sigma} - K_3 \tilde{\Sigma} - \sum_{i=1}^{3} S_d N_i \frac{\partial \tilde{\Sigma}}{\partial x_i}}_{resolved} + \underbrace{K_5 \tilde{\Sigma} + K'\left(\tilde{\Sigma} - K''\right)\tilde{\Sigma}}_{SGS}$$

Constants are:

$$K_1 = \left(\frac{\partial \tilde{u}_j}{\partial x_j} - N_i N_j : \frac{\partial \tilde{u}_i}{\partial x_j}\right)$$

$$K_2 = S_d \nabla \cdot \left(N_i\right)$$

$$K_3 = \nabla \cdot \left(S_d N_i\right)$$

$$K_5 = \Gamma\left(\frac{\hat{u}'_{SGS}}{S_{L,0}}, \frac{\hat{\Delta}}{\delta_L}\right) \frac{\hat{u}'_{SGS}}{\hat{\Delta}}$$

$$K' = \beta^* S_{L,0} \frac{c^* - \bar{c}}{\bar{c}(1 - \bar{c})}$$

$$K'' = \tilde{\Sigma}^{lam}$$

Last term on the r.h.s. can be transformed into:

$$K'\left(\tilde{\Sigma} - K''\right)\tilde{\Sigma} = K'\tilde{\Sigma}^2 - K'K''\tilde{\Sigma} = -K_6 \tilde{\Sigma} + K_7 \tilde{\Sigma}^2$$

Finally, source terms for FSD equation can be written:

$$S_\Sigma = C_1 \tilde{\Sigma} + C_2 \tilde{\Sigma}^2 - \sum_{i=1}^{3} S_d N_i \frac{\partial \tilde{\Sigma}}{\partial x_i}$$

$$C_1 = \left(K_1 + K_2 - K_3 + K_5 - K_6\right)$$

$$C_2 = K_7$$

Bibliography

[1] E. R. Hawkes and R. S. Cant, “A flame surfac e density approach to large-eddy simulation of premixed turbulent combustion,” *Proceedings of the Combustion Institute,* vol. 28, no. 1, pp. 51-58, 2000.

[2] E. R. Hawkes and R. S. Cant, “Implications of a Flame Surface Density Approach to Large Eddy Simulation of Premixed Turbulent Combustion,” *Combustion and Flame,* vol. 126, no. 3, pp. 1617-1629, 2001.

[3] S. Richard, O. Colin, O. Vermorel, A. Benkenida, C. Angelberger and D. Veynante, “Towards large eddy simulation of combustion in spark ignition engines,” *Proceedings of the Combustion Institute,* vol. 31, no. 1, pp. 3059-3066, 2007.

[4] O. Vermorel, S. Richard, O. Colin, C. Angelberger, A. Benkenida and D. Veynante, “Towards the understanding of cyclic variability in a spark ignited engine using multi-cycle LES,” *Combustion and Flame,* vol. 156, pp. 1525-1541, 2009.

[5] F. Charlette, C. Meneveau and D. Veynante, “A power-law flame wrinkling model for LES of premixed turbulent combustion PART I: non-dynamic formulation and initial tests,” *Combustion and Flame,* vol. 131, no. 1-2, pp. 159-180, 2002.

[6] J. F. Driscoll, “Turbulent premixed combustion: Flamelet structure and its effect on turbulent burrning velocities,” *Progress in Energy and Combustion Science,* vol. 34, no. 1, pp. 91-134, 2008.

[7] V. R. Savarianandam and C. J. Lawn, “Burning velocity of premixed turbulent flames in the weakly wrinkled regime,” *Combustion and Flame,* vol. 146, no. 1-2, pp. 1-18, 2006.

[8] Y.-C. Chen, N. Peters, G. A. Schneemann, N. Wruck, U. Renz and M. S. Mansour, “The detailed flame structure of highly stretched turbulent premixed methane-air flames,” *Combustion and Flame,* vol. 107, no. 3, pp. 223-244, 1996.

[9] R. O. S. Prasad and J. P. Gore, “An Evaluation of Flame Surface Density Models for Turbulent Premxed Jet Flames,” *Combustion and Flame,* vol. 116, no. 1, pp. 1-14, 1998.

[10] M. Herrmann, “Numerical simulation of turbulent Bunsen flames with a level set flamelet model,” *Combustion and Flame,* vol. 145, pp. 357-375, 2006.

[11] G. Wang, M. Boileau and D. Veynante, “Implementation of a dynamic thickened flame model for large eddy simulations Implementation of a dynamic thickened flame model for large eddy simulations,” *Combustion and Flame,* vol. 158, no. 1, pp. 2199-2213, 2010.

[12] F. E. Hernandez-Perez, F. T. C. Yuen, C. P. T. Groth and O. L. Gulder, “LES of a laboratory-scale turbulent premixed Bunsen flame using FSD, PCM-FPI and thickened flame models,” *Proceedings of the Combustion Institute,* vol. 33, no. 1, pp. 1365-1371, 2011.

[13] H. Kobayashi, “The subgrid-scale models based on coherent structures for rotating homogeneous turbulence and turbulent channel flow,” *Physics of Fluids* , vol. 17, pp. 1-12, 2005.

[14] H. Kobayashi, F. Ham and X. Wu, “Application of a local SGS model based on coherent structures to complex geometries,” *International Journal of Heat and Fluid Flow,* vol. 29, no. 3, pp. 640-653, 2008.

[15] L. Perković, P. Silva, M. Ban, N. Kranjčević and N. Duić, “Harvesting high altitude wind energy for power production: The concept based on Magnus’ effect,” *Applied Energy,* 2012.

[16] F. Mathey, D. Cokljat, J. P. Bertoglio and E. Sergent, “Assessment of the vortex method for Large Eddy Simulation inlet conditions,” *Progress in Computational Fluid Dynamics,* vol. 6, no. 1-3, pp. 58-67, 2006.

[17] G. Lodato, P. Domingo and L. Vervisch, “Three-dimensional boundary conditions for direct and large-eddy simulation of compressible viscous flows,” *Journal of Computational Physics,* vol. 227, no. 1, pp. 5105-5143, 2008.

[18] O. Vermorel, S. Richard, O. Colin, C. Angelberger, A. Benkenida and D. Veynante, “Towards the understanding of cyclic variability in a spark ignited engine using multi-cycle LES,” *Combustion and Flame,* vol. 156, no. 1, pp. 1525-1541, 2009.

[19] M. Breuer, D. Lakehal and W. Rodi, “Flow around a surface mounted cubical obstacle: comparison of LES and RANS results,” pp. 22-30, 1996.

[20] J. J. and S. A, “Large Eddy Simulation of Turbulent Combustion Systems,” *Proceedings of the Combustion Institute,* vol. 30, pp. 537-547, 2005.

[21] R. Panton, Incompressible Flow, Wiley-Interscience; 2nd edition , 1997.

[22] T. Arkady, An Informal Introduction to Turbulence, Dordrecht: Kluwer Academic Publishers, 2011.

[23] J. Froehlich and D. von Terzi, “Hybrid LES/RANSmethods for the simulation of turbulent flows,” *Progress in Aerospace Sciences,* vol. 44, no. 1, pp. 349-377, 2008.

[24] A. Leonard, “Energy Cascade in Large-Eddy Simulations of Turbulent Fluid Flows,” *Advances in Geophysics,* vol. 18, p. 237, 1974.

[25] P. Sagaut, Large Eddy Simulation for Incompressible Flows, Verlag Berlin Heidelberg: Springer, 2006.

[26] Z. Wang, Y. Lv, P. He, J. Zhou and K. Cen, “Fully explicit implementation of direct numerical simulation for a transient near-field methane/air diffusion jet flame,” *Computers & Fluids,* vol. 39, no. 8, pp. 1381-1389, 2010.

[27] E. Hawkes and J. Chen, “Direct numerical simulation of hydrogen-enriched lean premixed methane–air flames,” *Combustion and Flame,* vol. 138, no. 3, pp. 242-258, 2004.

[28] E. Hawkes and J. Chen, “Comparison of direct numerical simulation of lean premixed methane–air flames with strained laminar flame calculations,” *Combustion and Flame,* vol. 144, no. 1-2, pp. 112-125, 2006.

[29] S. B. Pope, Turbulent Flows, Cambridge: Cambridge University Press, 2000.

[30] J. O. Hinze, Turbulence, New York: McGraw-Hill, 1975.

[31] D. Veynante and L. Vervisch, “Turbulent combustion modelling,” 30.11.2013 2004. [Online]. [Accessed 2013].

[32] A. Favre, “Statistical equations of turbulent gases,” in *Problems of hydrodynamics and continuum mechanics*, Philadelphia, SIAM, 1969, pp. 231-266.

[33] S. Ghosal and P. Moin, “The basic equations for large eddy simulation of turbulent flows in complex geometry,” *J.Comp.Phys.*, vol. 118, pp. 24-37, 1995.

[34] J. Ferziger and M. Perić, Computational Methods for Fluid Dynamics, Springer Verlag, 1999.

[35] I. Alfirević, Uvod u tenzore i mehaniku kontinuuma, Zagreb: Golden Marketing, 2003.

[36] C. Hirsch, Numerical Computation of Internal and External Flows, Volume 1: Fundamentals of Numerical Discretization, John Wiley & Sons, 1988.

[37] K. K. Kuo, Principles of Combustion, John Wiley & Sons, Inc., 1986.

[38] C. Lubbers, B. G. and J. Boersma, “Simulation of the mixing of a passive scalar in a round turbulent jet,” *Fluid Dynamics Research,* vol. 28, p. 189–208, 2001.

[39] S. Bai and L. Fuchs, “Sensitivity study of turbulent reacting flow modeling in gas turbine combustors,” *AIAA Journal,* vol. 33, p. 1857–1864, 1995.

[40] H. Pitsch, “Unsteady Flamelet Modeling of Differential Diffusion in Turbulent Jet Diffusion Flames,” *Combustion and Flame,* vol. 123, pp. 358-374, 2000.

[41] H. Kobayashi, F. Ham and X. Wu, “Application of a local SGS model based on coherent structures to complex geometries,” *International Journal of Heat and Fluid Flow,* vol. 29, no. 3, pp. 640-653, 2008.

[42] H. Kobayashi, “Large eddy simulation of magnetohydrodynamic turbulent channel flows with local subgrid-scale model based on coherent structures,” *Phys. Fluids,* vol. 18, 2006.

[43] H. Kobayashi, “Large eddy simulation of magnetohydrodynamic turbulent duct flows,” *Phys. Fluids,* vol. 20, 2008.

[44] H. Fasel, J. Seidel and S. Wernz, “A methodology for simulation of complex turbulent flows,” *J Fluids Eng,* vol. 124, p. 933–42., 2002.

[45] H. Zhang, C. Bachman and H. Fasel, “Application of a new methodology for complex turbulent flows,” *AIAA paper,* Vols. 2000-2535, 2000.

[46] K. Hanjalić, M. Popovac and M. Hadžiabdić, “A robust near-wall elliptic-relaxation eddy-viscosity turbulence model for CFD,” *International Journal of Heat and Fluid Flow,* vol. 25, no. 6, pp. 1047-1051, 2004.

[47] G. Delibra, D. Borello, K. Hanjalić and F. Rispolia, “URANS of flow and endwall heat transfer in a pinned passage relevant to gas-turbine blade cooling,” *International Journal of Heat and Fluid Flow,* vol. 30, no. 3, p. 549–560, 2009.

[48] G. Delibra, K. Hanjalić, D. Borello and F. Rispolia, “Vortex structures and heat transfer in a wall-bounded pin matrix: LES with a RANS wall-treatment,” *International Journal of Heat and Fluid Flow,* vol. 31, no. 5, pp. 740-753, 2010.

[49] “CFD Solver (AVL FIRE manual),” 2010.

[50] N. Peters, Turbulent combustion, Cambridge: Cambridge University Press, 2000.

[51] C. Schneider, A. Dreizler and J. Janicka, “Fluid dynamical analysis of atmospheric reacting and isothermal swirling flows,” *Flow, turbulence and combustion,* vol. 74, pp. 103-127, 2005.

[52] N. Peters, “Turbulent reactive flows,” *Lecture notes in physics,* vol. 241, pp. 242-256, 1985.

[53] C. Meneveau and T. Poinsot, “Stretching and quenching of flamelets in premixed turbulent combustion,” *Combustion and Flame,* vol. 86, pp. 311-332, 1991.

[54] R. Colin, F. Ducros, D. Veynante and T. Poinsot, “A thickened flame model for large eddy simulations of turbulent premixed combustion,” *Phys. Fluids,* vol. 12, no. 7, p. 1843–1863, 2000.

[55] C. T. Chong and S. Hochgreb, “Measurements of laminar flame speeds of acetone/methane/air mixtures,” *Combustion and Flame,* vol. 158, no. 3, pp. 490-500, 2011.

[56] H. Miao and Y. Liu, “Measuring the laminar burning velocity and Markstein length of premixed methane/nitrogen/air mixtures with the consideration of nonlinear stretch effects,” *Fuel,* vol. 121, no. 1, pp. 208-215, 2014.

[57] Z. Chen, P. Dai and S. Chen, “A model for the laminar flame speed of binary fuel blends and its application to methane/hydrogen mixtures,” *International Journal of Hydrogen Energy,* vol. 37, no. 13, p. 10390–10396, 2012.

[58] M. Metgalchi and J. Keck, “Burning velocities of mixtures of air with methanol, iso-octane, and idolene at high pressure and temperature,” *Combustion and Flame,* vol. 48, pp. 191-210, 1982.

[59] *PREMIX: A Program for Modeling Steady, Laminar, One-dimensional Premixed Flames,* Reaction Design, PRE-036-1 2000..

[60] M. Ban, Numerical modelling of auto-ignition chemistry kinetics in computational fluid dynamics (PhD thesis), Zagreb, 2010.

[61] S. Bougrine, S. Richard, A. Nicolle and V. D., “Numerical study of laminar flame properties of diluted methane-hydrogen-air flames at high pressure and temperature using detailed chemistry,” *International Journal of Hydrogen Energy,* vol. 36, no. 18, pp. 12035-12047, 2011.

[62] M. Baburić, “Numerically efficient modelling of turbulent non-premixed flames (PhD Thesis),” Zagreb, 2005.

[63] G. P. e. a. Smith, “GRI 3.0,” [Online]. Available: http://www.me.berkeley.edu/gri_mech.

[64] O. Colin and K. Truffin, “A spark ignition model for large eddy simulation based on a FSD transport equation (ISSIM-LES),” *Proceedings of the Combustion Institute,* vol. 33, pp. 3097-3140, 2011.

[65] L. Petzold, “DASSL,” [Online]. Available: http://www.dm.uniba.it/~testset/solvers/dassl.php. [Accessed 27 01 2014].

[66] A. C. Hindmarsh, “Serial Fortran Solvers for ODE Initial Value Problems,” Lawrence Livermore National Laboratory, [Online]. Available: http://computation.llnl.gov/casc/odepack/odepack_home.html. [Accessed 27 01 2014].

[67] C. Madhav Rao Vendra, W. J. X. and T. V.H.Y, “Numerical simulation of turbulent flameewall quenching using a coherent flame model,” *Journal of Loss Prevention in the Process Industries,* vol. 26, pp. 363-368, 2013.

[68] T. Poinsot and V. D., Theoretical and numerical combustion, Philadelphia: R. T. Edwards Inc., 2005.

[69] H. Jasak, Error Analysis and Estimation for the Finite Volume Method with Applications to FLuid Flows (PhD thesis), London, 1996.

[70] N. Chakraborty and R. S. Cant, “Effects of Lewis number on turbulent scalar transport and its modelling in turbulent premixed flames,” *Combustion and Flame,* vol. 156, pp. 1427-1444, 2009.

[71] V. Katta, L. Goss and W. M. Roquemore, “Effect of non-unity Lewis number and finite-rate chemistry on the dynamics of a hydrogen–air jet diffusion flame,” *Combust. Flame,* vol. 96, pp. 60-74, 1996.

[72] J. B. Bell, R. K. Cheng, M. S. D. and S. I. G., “Numerical simulation of Lewis number effects on lean premixed turbulent flames,” *Proceedings of the Combustin Institute,* vol. 31, pp. 1309-1317, 2007.

[73] N. Chakraborty, K. M. and S. N., “Effects of Lewis number on the reactive scalar gradient alignment with local strain rate,” *Proceedings of the Combustion Institute,* vol. 32, pp. 1409-1417, 2009.

[74] N. Chakraborty and R. S. Cant, “Effects of Lewis number on flame surface density transport in turbulent premixed combustion,” *Combustion and Flame,* vol. 158, no. 9, pp. 1768-1787, 2011.

[75] T. Shamim, “Effect of unequal fuel and oxidizer Lewis numbers on flame dynamics,” *International Journal of Thermal Sciences,* vol. 46, no. 1213–1223, 2006.

[76] L.-Y. Jiang and C. I, “Prandtl/Schmidt number effect on temperature distribution in a generic combustor,” *International Journal of Thermal Sciences,* vol. 48, p. 322–330, 2009.

[77] M. J., G. B. J. and S. P., “A computational error-assessment of central finite-volume discretizations in large-eddy simulation using a Smagorinsky model,” *Journal of Computational Physics,* vol. 227, pp. 156-173, 2007.

[78] J. Meyers, B. J. Geurts and P. Sagaut, “A computational error-assessment of central finite-volume discretizations in large-eddy simulation using a Smagorinsky model,” *Journal of Computational Physics,* vol. 227, no. 1, pp. 156-173, 2007.

[79] S. V. Patankar, Numerical Heat Transfer and Fluid Flow, Washington: Hemisphere Publishing Corporation, 1980.

[80] A. Katz and V. Sankaran, “Mesh quality effects on the accuracy of CFD solutions on unstructured meshes,” *Journal of Computational Physics* , vol. 230, no. 20, pp. 7670-7686, 2011.

[81] M. Mossi and P. Sagaut, "Numerical investigation of fully developed channel flow using shock-capturing schemes," *Comput. Fluids,* vol. 31, p. 695., 2002.

[82] M. Meinke, W. Schroder, E. Krause and T. Rister, “A comparison of second- and sixth-order methods for large-eddy simulations,” *Comput. Fluids,* vol. 31, p. 695., 2002.

[83] B. P. Leonard, “Simple high-accuracy resolution program for convective modelling of discontinuities,” *Int. Journal for Numerical Methods in Fluids,* vol. 8, pp. 1291-1318, 1988.

[84] G. Kuenne, A. Ketelheun and J. Janicka, “LES modelling of premixed combustion using a thickened flame approach coupled with FGM tabulated chemistry,” *Combustion and Flame,* vol. 158, no. 1, pp. 1750-1767, 2011.

[85] T. Schmitt, A. Sadiki, B. Fiorina and D. Veynante, “Impact of dynamic wrinkling model on the prediction accuracy using the F-TACLES combustion model in swirling premixed turbulent flames,” *Proceedings of the Combustion Institute,* vol. 34, no. ¸1, pp. 1261-1268, 2013.

[86] A. K. Gupta, D. G. Lilley and N. Syred, Swirl Flows, Turnbridge Wells: Abacus Press, 1984.

[87] J. M. Duclos, D. Veynante and T. Poinsot, “A comparison of flamelet models for premixed turbulent combustion,” *Combustion and FLame,* vol. 95, no. 1-2, pp. 101-117, 1993.

[88] B. Lansdorp and W. J. Ockels, *Comparison of concepts for high-altitude wind energy,* The 2nd China International Renewable Energy Equipment & Technology Exhibition ed., 2005.

[89] D. B. Spalding, Combustion and Mass Transfer: A Textbook with Multiple-Choice Exercises for Engineering Students, New York: Pergamont Press, 1979.

[90] “FLOW and COMBUSTION (Phoenics),” [Online].

Curriculum vitae in English

Personal data

Name:	Luka
Surname:	Perković
Date of birth:	23. 11. 1982.
Place of birth:	Zagreb
email:	luka.perković@fsb.hr
URL:	http://powerlab.fsb.hr/lperkovic

Education

1989 - 1997	Elementary school in Zagreb
1997 - 2001	Secondary school in Zagreb (electro-technician)
2001 - 2007	Faculty of Mechanical Engineering and Naval Architecture (FMENA), Zagreb
2008 - 2013	Doctoral study at FMENA, Zagreb

Professional

since 2008	Research assistant at the Department of Energy, Power Engineering and Environment; teaching assistance in under-graduate courses "Fluid Mechanics I", "Modelling of Combustion and Radiative Heat Transfer", "Introduction to Energy Management" and "Energy planning" at FMENA
since 2008	Member of the International Centre for Sustainable Development of Energy, Water and Environmental Systems (SDEWES)
since 2013	Member of the Adria Section of The Combustion Institute

Foreign languages

English - very good (written and spoken)

German - communication level

Curriculum vitae in Croatian

Osobni podaci

Ime:	Luka
Prezime:	Perković
Datum rođenja:	23. 11. 1982.
Mjesto rođenja:	Zagreb
email:	luka.perković@fsb.hr
URL:	http://powerlab.fsb.hr/lperkovic

Obrazovanje

1989 - 1997	Osnovna škola u Zagrebu
1997 - 2001	Srednja škola u Zagrebu (zvanje elektrotehničar)
2001 - 2007	Fakultet strojarstva i brodogradnje Sveučilišta u Zagrebu (FSB), Zagreb
2008 - 2013	Doktorski studij na FSB, Zagreb

Profesionalne aktivnosti

since 2008	Znanstveni novak na Zavodu za energetska postrojenja, energetiku i ekologiju; asistiranje u nastavi iz kolegija "Mehanika fluida I", "Modeliranje izgaranja i zračenja", "Osnove energetike" and "Energetsko planiranje" na FSB-u.
since 2008	Član Međunarodnog centra za održivi razvoj energetike, voda i okoliša (SDEWES)
since 2013	Član Jadranske sekcije Instituta za izgaranje

Strani jezici

Engleski - vrlo dobro (pisanje i govor)

Njemački - komunikacijski nivo